Studies of Spin-Exchange Optical Pumping

by

Bien Chann

A dissertation submitted in partial fulfillment

of the requirements for the degree of

Doctor of Philosophy

(Physics)

at the

UNIVERSITY OF WISCONSIN-MADISON

2003

Contents

List of Figures

List of Tables

Chapter 1

Introduction

1.1 Motivation

Nuclear spin-polarized ^{3}He and ^{129}Xe [Walker97][Appelt98] are becoming increasingly important in many areas of fundamental physics and applied physics. Applications of these "hyperpolarized" noble gases include magnetic resonance imaging of the lungs and other organs [Albert94][Middleton95][MacFall96], precision measurements [Bear00] [Newbury91] [Romalis01], spin-polarized targets for nuclear physics [Xu00] [Jones00], quantum computation [Verhulst01], and surface physics [Nagasaka01][Raftery91][Wu90]. Since its discovery in 1960 by Carver and coworkers [Bouchiat60] the technology has progressed to such an extent that liters of highly polarized ^{3}He and ^{129}Xe are routinely produced by laboratories around the world. Nevertheless, the basic fundamental limits to the efficiency of the spin-exchange process rates are not fully understood. For example, the fundamental spin-exchange rate in Rb-^{3}He reported in the literature differs by as much as a factor of 2 [Coulter90][Larson91][Baranga98].

In spin exchange optical pumping, resonance circularly polarized pump light is absorbed by the alkali-metal vapor contained in a glass cell. Also contained in the

glass cell is a much larger quantity of noble gas. Collisions between the alkali-metal atoms and noble gas atoms transfer some of the electron-spin polarization to the nuclei of the noble gas. The polarization of the noble gas in steady-state is [Walker97]

$$\begin{aligned} P &= P_{Rb}\frac{\kappa[Rb]}{(\kappa[Rb]+\Gamma_w)} \\ &= \frac{R_p}{(R_p+\Gamma_{Rb})}\frac{\kappa[Rb]}{(\kappa[Rb]+\Gamma_w)}, \end{aligned} \tag{1.1}$$

where P_{Rb} is the Rb polarization, R_p is the optical pumping rate, Γ_{Rb} is the Rb spin-relaxation rate, $[Rb]$ is the Rb density, Γ_w is the noble gas wall-relaxation rate, and κ is the Rb-noble gas spin-exchange rate coefficient. With the current understanding of the spin-exchange process and the available technology of high power diode-array bars, it should be possible to have $R_p \gg \Gamma_{Rb}, \kappa[Rb] \gg \Gamma_w$ so that equation 1.1 predicts a very high noble gas polarization. In ^{3}He, the polarization should be close to unity with an easily-made room-temperature cell lifetime of a few hundred hours [Rich02][Hsu00]. However, the highest ^{3}He polarization reported in the literature for diode pumping is about 55% [Rich02]. In ^{129}Xe the typical observed polarization is about 10 to 15% [Driehuys96]. Thus, for example, the resolution of the magnetic resonance of the lungs using ^{129}Xe is still very much limited by this low ^{129}Xe polarization. Experiments which rely on high ^{3}He polarization could also greatly benefit from higher than 55% ^{3}He polarization. For example, an upcoming experiment at the Los Alamos spallation neutron source plans to measure the weak nucleon-nucleon coupling constant, H_π, by measuring the gamma ray emission directional parity-violating asymmetry (A_γ) in the $\overline{n} + p \rightarrow d + \gamma$ reaction. Here polarized ^{3}He is used as a neutron polarizer. The goal of the experiment is to measure A_γ with an uncertainty of $< 5 \times 10^{-9}$. Assuming the current value of 55% ^{3}He polarization, this makes the run time of the nuclear reactor to 500 days. With ^{3}He polarization of 74% as demonstrated in this thesis, that reduces the run time to 290 days.

In order to understand the low-observed noble gas polarization, all of the parameters in equation 1.1 must be carefully studied. In this thesis I describe a comprehensive study that was undertaken in the last four years in trying to understand the fundamental processes in spin-exchange optical pumping.

1.2 Overview of Spin-Exchange Optical Pumping

In spin-exchange optical pumping [Happer72] [Walker97] [Appelt98], resonance circularly polarized pump light is absorbed by the alkali-metal atoms, usually Rb, contained in a sealed glass cell. The transition of interest is the $5^2S_{1/2} \rightarrow 5^2P_{1/2}$. Also contained in the sealed glass cell is a a high density of ^{3}He or ^{129}Xe. In most conditions, the hyperfine levels of the Rb atom are not resolved due to the pressure broadening of the noble gas (20 Ghz/Amagat)[Romalis97]. Normally, the pressure of the noble gas ranges from 1 to 10 amagats [amg], so that the pressure broadening is many tens of GHz, and much greater than the hyperfine splitting of the Rb atoms. Even at one amagat of noble gas pressure, the laser linewidth is typically much greater than the hyperfine levels. Thus, all the Rb hyperfine levels are pumped equally.

Also in the sealed glass cell is a fraction of an amagat of buffer gas, almost always N_2. After the Rb atoms absorb a resonance photon they collide with the noble gas or N_2 before they decay optically . The collisions redistribute the Rb atoms in the excited state with equal probability. Once in the excited state the Rb atoms have an equal probability of de-exciting to the ground state. The excitation energy is absorbed by the N_2. On average, therefore, half a unit of the photon angular momentum is transferred to the Rb atom per one unit of photon angular momentum absorbed. Figure 1.1 shows a simplified optical pumping of the D1 line with only two Zeeman sublevels.

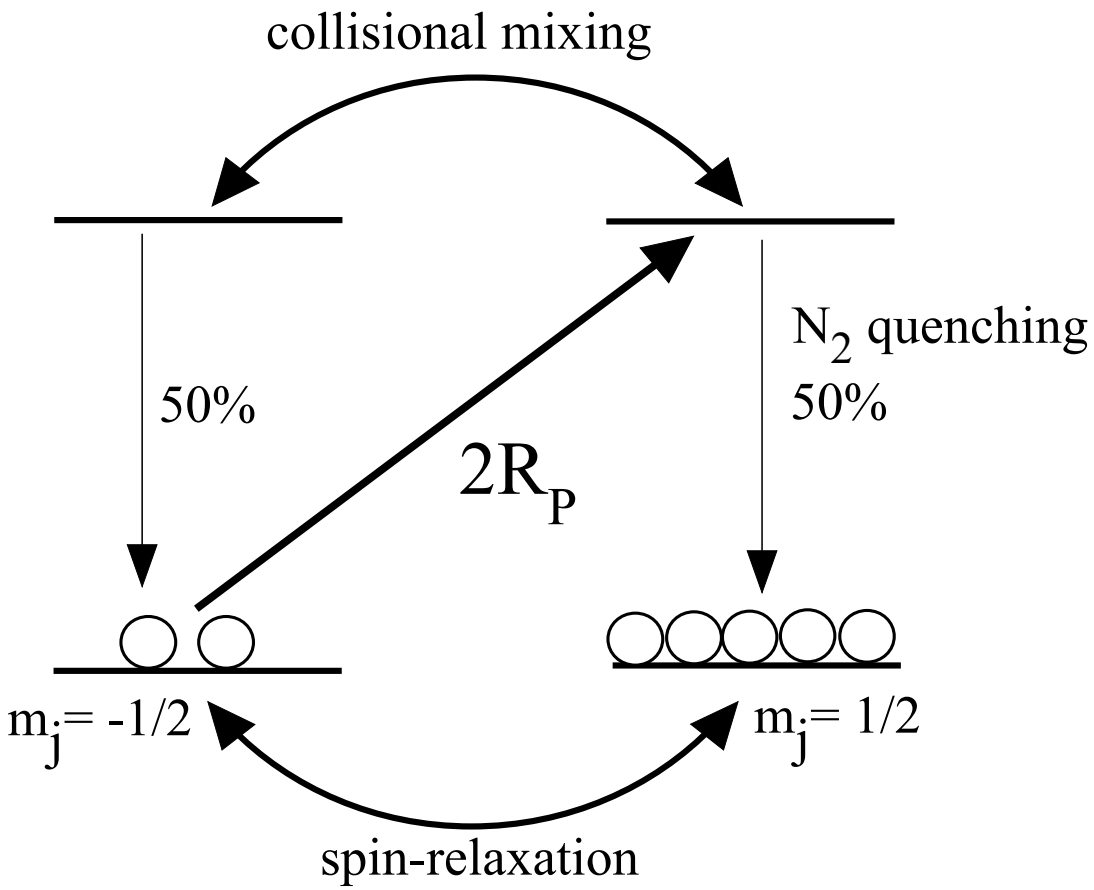

Figure 1.1: A simplified picture of optical pumping of the D1 line.

The average photon absorption rate is [Walker97] [Appelt98]

$$\langle \delta\Gamma \rangle = (1 - 2\langle S_z \rangle) R_p, \tag{1.2}$$

where R_p is the pumping rate for the unpolarized Rb atoms, and $2\langle S_z \rangle$ is the average polarization of the Rb atoms. The pumping rate is given as [Happer72] [Walker97] [Appelt98]

$$R_p = \int_0^\infty I(\nu)\sigma(\nu)d\nu, \tag{1.3}$$

where $I(\nu)$ is the intensity of the pumping laser per unit frequency and $\sigma(\nu)$ is the Rb absorption cross section.

The rate equation which governs the average spin of the Rb atoms, $\langle F_z \rangle$, is

$$\frac{d\langle F_z \rangle}{dt} = \frac{1}{2}(1 - 2\langle S_z \rangle) R_p - \Gamma_{Rb}\langle S_z \rangle, \tag{1.4}$$

where $(1-2\langle S_z \rangle)R_p$ is the rate at which the photons are absorbed, and each absorption deposits 1/2 unit of angular momentum. Γ_{Rb} is the total Rb atoms spin-relaxation rates. Hence, in steady state, the Rb polarization, $P_{Rb} = 2\langle S_z \rangle$, is

$$P_{Rb} = \frac{R_p}{(R_p + \Gamma_{Rb})} \tag{1.5}$$

Once the Rb atoms are spin-polarized, some fraction of the electron spin is transferred to the nuclear spin of the noble gas through spin-exchange collisions [Happer72] [Walker97] [Appelt98]. The Hamiltonian of the Rb-noble gas system is [Walter98]

$$H = A_a \mathbf{I}_a \cdot \mathbf{S} + g_S \mu_B \mathbf{S} \cdot \mathbf{B} + \mu_a \mathbf{I}_a \cdot \mathbf{B} + \mu_b \mathbf{K} \cdot \mathbf{B} + \gamma \mathbf{N} \cdot \mathbf{S} + A_b \mathbf{K} \cdot \mathbf{S} + B_b \mathbf{K} \cdot (3\hat{\mathbf{R}}\hat{\mathbf{R}} - 1) \cdot \mathbf{S}, \tag{1.6}$$

where $\mathbf{I}_a$, $\mathbf{K}$, and $\mathbf{S}$ are the spins of the Rb nucleus, noble gas nucleus and the alkali-metal electron, respectively. $\mathbf{B}$ is the external magnetic field and $\mathbf{N}$ is the rotational angular momentum of the colliding pair. $\hat{\mathbf{R}}$ is the vector displacement between the pair. The first term of the Hamiltonian is the hyperfine coupling between the electron

and nucleus of the alkali-metal atoms and is usually the strongest. The second, third and fourth terms are the coupling of the spins to the external magnetic field. The term $\gamma\mathbf{N}\cdot\mathbf{S}$ causes spin-relaxation due to the coupling between the spin of the electron and the rotational angular momentum of the colliding pair. The term $A_b\mathbf{K}\cdot\mathbf{S}$ is responsible for the spin-exchange between the electron spin of the alkali-metal and the nucleus of the noble gas. This is the well-understood isotropic hyperfine "Fermi contact" interaction that aligns the noble-gas nuclear spin with the electron spin of the alkali-metal atom. The last term is the anisotropic coupling of the electron spin with the noble gas nucleus due to the long-range classical dipole-dipole interaction [Walter98] which is usually ignored. A substantial value of B_b is a potential explanation for the low observed noble gas polarization and will be discused in chapter 6.

1.3 Summary of Thesis

1.3.1 Introduction

The thesis is comprised of four parts. The first part deals with alkali-alkali metal spin-relaxation, an important contribution to Γ_{Rb}, which is described in detail in chapter 2. The second part describes the ^{129}Xe-Xe molecular spin-relaxation in van der Waals molecules and is described in chapter 3. This process is a fundamental limit in Γ_w for ^{129}Xe. The third part of the thesis addresses the invention of an external cavity diode array bar [Chann00] for spin-exchange optical pumping and is described in chapter 4. This device allows for a greater R_p and higher P_{Rb}. The last part of the thesis deals with the measurements of the Rb-^{3}He spin-exchange rate coefficients, κ, and is described in chapters 5 and 6. The thesis is summarized in chapter 7.

The following subsections give summaries of findings.

1.3.2 Cesium-Cesium spin-relaxation

From equation 1.5 the alkali-metal atom polarization is limited by the alkali-metal spin destruction rate Γ_{Rb}. Alkali-alkali spin-relaxation accounts for the majority of the spin-relaxation. Originally, the alkali-alkali spin-relaxation mechanism was thought to arise mainly from binary collisions. This was proven to be incorrect when Kadlecek, Walker, and Anderson [Kadlecek98] showed that the relaxation rate could be decoupled in a magnetic field of few thousand gauss. The mechanism responsible, however, was not understood.

Although, we still do not understand the alkali-alkali metal spin-relaxation in buffer gases at pressures of an amagat or more, the low pressure Cs experiment in this thesis proves that the main alkali-alkali relaxation comes from the spin-axis interaction

$$\frac{2\lambda}{3}\mathbf{S}\cdot(3\hat{\xi}\hat{\xi}-\mathbf{1})\cdot\mathbf{S}, \tag{1.7}$$

where $\mathbf{S}=\mathbf{S_1}+\mathbf{S_2}$ is the total electron spin of the colliding pair, $\hat{\xi}$ is a unit vector along the direction of the internuclear axis. $\lambda=\lambda(R)$ is the interaction energy thought to arise from the electrons' magnetic moments and spin-orbit interaction in second order [Mies96].

Results from fitting the Cs experimental data with the theory as predicted by spin-axis interaction are summarized in table 1.1. The first two columns assume each collision breaks up the molecules and the last two columns allow for collisional reorientation without breakup. The theoretical chemical equilibrium coefficient, ${}^3\kappa_{chem}$, calculated using the *ab intio* potential calculated by Krauss and Stevens [Krauss90] gives 613 A^3. Thus, λ is most likely accurate to a factor of about 2.

We also measure the spin-destruction cross section between ^{4}He, N_2 buffer gas with

Positive λ	Negative λ	Positive λ	Negative λ
$\lambda = 3.4$ GHz	$\lambda = -2.9$ GHz	$\lambda = 2.71$ GHz	$\lambda = -2.13$ GHz
$\kappa = 307$ A^3	$\kappa = 350$ A^3	$\kappa = 431$ A^3	$\kappa = 584$ A^3
$\sigma = 82$ A^2	$\sigma = 98$ A^2	$\sigma = 55$ A^2	$\sigma = 42$ A^2

Table 1.1: Cesium-cesium spin-relaxation fitted parameters. The first two columns assume each collision breaks up the molecules, the last two columns allow for collisional reorientation without breakup. λ is the spin-axis interaction strength, ${}^3\kappa_{chem}$ is the chemical equilibrium coefficient, and σ is the breakup cross section. The theoretical ${}^3\kappa_{chem}$ calculated using the *ab intio* potential calculated by Krauss and Stevens [Krauss90] gives 613 A^3. Thus, λ is most likely accurate to a factor of about 2.

Cs atoms

$$\sigma_{N_2-Cs} = 38.6 \times 10^{-22} \text{ cm}^2 \tag{1.8}$$

$$\sigma_{^4He-Cs} = 6.3 \times 10^{-22} \text{ cm}^2. \tag{1.9}$$

The $\sigma_{^4He-Cs}$ cross section is about a factor of ten bigger than the calculated value by Walker of $(0.6 \times 10^{-22}\text{cm}^{-2})$[Walker89].

1.3.3 ^{129}Xe-Xe molecular spin-relaxation

One of the big applications of spin-polarized noble gases is in magnetic resonance imaging of human organs. One of the challenges is to be able to store the polarized noble gas as long as possible before administering it to patients. In the ^{3}He the dipole-dipole interactions place the fundamental limit in bulk ^{3}He relaxation at $(807/P)$ hours, where P is the partial pressure of ^{3}He in units of bars at room temperature [Newbury93]. Previously for ^{129}Xe, it has been generally accepted that the fundamental limit is 56 hours which is due to the ^{129}Xe spin-relaxation due to ^{129}Xe-Xe binary collisions

[Hunt63] [Moudrakovski01].

We identified a new gas-phase ^{129}Xe-Xe spin-relaxation that is due to the formation of van der Waals molecules. The interaction responsible for the relaxation is the spin-rotation coupling between the nuclear spin, **K**, and the rotational angular momentum, **N**, of the molecules

$$V_{sr} = c_K(R)\mathbf{K} \cdot \mathbf{N}. \tag{1.10}$$

For a fixed gas composition this mechanism is independent of gas density and thus difficult to isolate from the wall relaxation. To measure the relaxation due to van der Waals molecules we measure the total relaxation as a function of gas composition. The measured van der Waals molecules spin-relaxation contributes

$$\Gamma_{vdW} = 6.72 \pm 0.1 \times 10^{-5}\ \mathrm{s}^{-1} \tag{1.11}$$

to the total observed relaxation rate. This is more than an order of magnitude larger than the well-known spin-relaxation due to the ^{129}Xe-Xe binary collisions at one 1 atmosphere of pressure. Thus, this makes spin-relaxation due to van der Waals molecules the primary fundamental process at gas densities less than 14 amagats. The measured rate is consistent with the theoretical estimates deduced from previously measured NMR chemical shifts. From Γ_{vdW} we calculate the breakup cross section to be

$$\sigma = 44\mathring{A}^2 \tag{1.12}$$

1.3.4 External Cavity Diode Array Bar

One of the crucial steps in achieving high noble gas polarization is to have a high alkali-metal atoms pumping rate. In the last ten years or so, traditionally, the laser of choice is the diode array bar with a power from 15W to hundred of watts. It is easy to use and relatively inexpensive compared to the dye laser or Ti:Sapphire laser.

However, one of the major disadvantages of the diode array bar is its large spectral width, about 1000 GHz. Traditionally, high pressures cells are used to match the absorption linewidth of the alkali-metal atoms (20 GHz/amagat) to the laser linewidth [Romalis97]. The highest ^{3}He polarization using such a diode array bar reported in the literature is about 55%. In ^{129}Xe the typical observed polarization is about 10 to 15%. Thus, the question arises of whether the observed low noble gas polarization is due to the inefficient pumping rate of the diode array bar. In order to answer that question, we invented an external cavity diode array bar [Chann00]. We have obtained a laser linewidth as low as 47 GHz with about 33% loss in power. The external cavity diode array bar is instrumental in achieving high polarization, especially in low pressure cells. It is detailed in chapter 4.

1.3.5 Rb-^{3}He spin-exchange rate coefficients

In the course of investigating the low observed noble gas polarizations we have measured the Rb-^{3}He spin-exchange rate coefficients. Until the work of Baranga *et al.* [Baranga98], only two measurements of the Rb-^{3}He spin-exchange rate coefficient had been reported. Coulter *et al.* [Coulter90] measured the spin-exchange rate coefficient to be $12 \pm 2 \times 10^{-20}$ cm^3/s. Larson *et al.* [Larson91] using the same method measured the spin-exchange rate coefficient to be $6.2 \pm 0.2 \times 10^{-20}$ cm^3/s. Both these measurements relied on the relaxation rate of ^{3}He as a function of temperature. In both cases the wall-relaxation is assumed to be temperature-independent. Also both experiments deduce the Rb vapor pressure using published saturated vapor curves, a procedure that can be in error by a factor of 2 or more [Jau02] [Borel02].

Recently, Baranga *et al.* [Baranga98] remeasured the Rb-^{3}He spin-exchange rate coefficient. They deduced the spin-exchange rate coefficient to be 6.7×10^{-20} cm^3/s.

Baranga used a different method which does not rely on Rb density measurement. Furthermore, his method made no assumption about the wall-relaxation of the cell. Therefore, it should be quite reliable.

To better understand the discrepancies between these three measurements, and also to further test our basic understanding of the spin-exchange optical pumping process we have measured the spin-exchange rate coefficients in Rb-^{3}He. We measured it three different ways. The first method we use is the same one used by Coulter [Coulter90] and Larson [Larson91] , which we call the "relaxation method". The second one is the method used by Baranga [Baranga98], which we call the "repolarization method". The third method is a new "rate balance method" which is based on the equilibrium ^{3}He polarization attained in a cell of known Rb density and ^{3}He polarization. Here, we make no assumption about the magnitude of the anisotropic spin-exchange rate.

We obtained $(6.73 \pm 0.12 \times 10^{-20})$ cm^3/s for the "repolarization method". Thus, it agrees very well with Baranga [Baranga98]. For the "rate balance method" we deduce the spin-exchange rate coefficient to be $(6.61 \pm 0.12 \times 10^{-20})$ cm^3/s. These two methods agree very well with each other. For the "relaxation method" we deduce the value to be $(8.82 \pm 0.16 \times 10^{-20})$ cm^3/s. This is about 30% higher than the other two methods, which implies a temperature-dependence wall-relaxation or a large value of anisotropic spin-exchange interaction for Rb-^{3}He. At this time, we believe the most likely cause is the temperature-dependence wall relaxation. Thus, this excess ^{3}He relaxation explains the low observed ^{3}He polarization.

References	Method	Spin-Exchange Rate Coeff. (10^{-20} cm^3/s)
This work	Relaxation Method	8.82 ± 0.16
[Coulter90]	Relaxation Method	12± 2
[Larson91]	Relaxation Method	6.2 ±0.2
This work	Repolarization	6.73 ±0.12
[Baranga98]	Repolarization	6.7 ± 0.6
This work	Rate Balance	6.61 ± 0.12

Table 1.2: Rb-^{3}He spin-exchange rate coefficients using various methods. The relaxation's method spin-exchange rate coefficient is most likely contaminated by wall effects, while the other two methods make no assumption about the wall.

Chapter 2

Cesium Spin-Relaxation

2.1 Introduction

Under the typical operating conditions of the Rb-^{3}He spin-exchange polarizers, the majority of the Rb spin depolarization is due to Rb-Rb collisions [Kadlecek98]. In 1980 Bhaskar *et al.* proposed that the alkali-alkali spin-relaxation is due to binary collisions [Bhaskar80], where the average duration collision time is about $\tau \approx 1$ psec [Happer72][Kadlecek98]. In 1998 Kadlecek, Anderson, and Walker [Kadlecek98] showed that the alkali-alkali spin-relaxation rate could be decoupled in a few kG of magnetic field. They reported the relaxation rate can be reduced up to a factor of 3 with a few kG of applied magnetic field. Hence, if the alkali-alkali spin-relaxation is due to binary collisions with a duration of ~ 1 psec, for an applied field of 1 kG, the precession around the applied magnetic field is

$$\Omega\tau = \frac{\mu_B B\tau}{\hbar} \ll 1, \tag{2.1}$$

where Ω is the Larmor precession frequency. Thus, the applied magnetic field of a few kG should not affect the alkali-alkali spin-relaxation rate. This rules out that the

alkali-alkali spin-relaxation comes from binary collisions. Kadlecek *et al.* measured the decoupling magnetic field width in Rb-Rb to be about 1.15 kG or a correlation time of about 50 ps. This implies that the alkali-alkali spin-relaxation occurs in molecules. The mechanism that is responsible was not understood.

Bhaskar *et al.* [Bhaskar80] also pointed out that there should be a spin-rotation interaction in triplet dimers of the form, $V_{sr} = \gamma \mathbf{S} \cdot \mathbf{N}$, where $\mathbf{S} = \mathbf{S_1} + \mathbf{S_2}$ is the total electronic spin of the dimer, and $\mathbf{N}$ is the rotational angular momentum of the pair. They ruled this out because the coupling coefficient γ was too small to account for the relaxation. Instead, they suggested a possible mechanism is the spin-axis interaction in triplet dimers of the form

$$V_{sa} = \frac{2\lambda}{3} \mathbf{S} \cdot (3\hat{\xi}\hat{\xi} - \mathbf{1}) \cdot \mathbf{S}, \tag{2.2}$$

where $\hat{\xi}$ is the unit vector between the two atoms.

The Cs-Cs experiment described here, along with the Rb-Rb experiment at Princeton University showed [Erickson00] that at pressures less than one amagat of buffer gas, half of the alkali-alkali-metal spin-relaxation comes from the spin-axis interaction in triplet dimer molecules. The key observation is the magnetic-resonances in spin-relaxation as predicted by the spin-axis interaction. The fit of the experimental data for Cs gives $\lambda = -2.13$ GHz with the chemical equilibrium coefficient of ${}^3\kappa_{chem} = 584$ A^3. This compares favorably to the theoretical estimate of 613 A^3 for the chemical equilibrium coefficient.

Section 2.2 is a brief overview of the experiment. Section 2.3 describes the apparatus (light sources, cell, detector) and techniques (rate measurement, Cs density) used to measure the Cs spin-relaxation. Section 2.4 details the theory of the spin-relaxation rate of triplet molecules due to the spin-axis interaction. Section 2.5 discusses the experimental data. Finally, section 2.6 presents the spin-relaxation cross section mea-

surement between Cs and buffer gas.

2.2 Brief Description of Experiment

The experimental setup is a typical spin-exchange optical pumping experiment. The setup is shown in figure 2.1 [Kadlecek98] [Kadlecek00][Kadlecek01]. We have a cell containing Cs vapor within a volume of about 100 cm^3. The cell is placed in an oven and heated to the desired temperature. Attached to the cell is a valve that is used to let in buffer gas or a mixture of buffer gases. The oven is placed in a uniform magnetic field. We then polarize the Cs vapor to a few percent polarization with a circularly polarized pump beam. After about 100-200 ms of pumping, the pump beam is blocked and we measure the time-dependent decay of the Cs polarization with a weak probe beam [Franzen59]. The exponential decay rate of the Cs polarization is the total relaxation rate of the Cs atoms. We make measurements as a function of magnetic field strength, buffer gas pressure, and Cesium density.

2.3 Experimental Apparatus

2.3.1 Light Sources

We use a standing-wave Ti:Sapphire laser (Spectra Physics model 3900) which is pumped by a 5W of an Ar^+ laser (Spectra Physics model 171) to pump the Cs vapor. The output of the Ti:Sapphire laser is about 50-150mW at 852 nm. The Ti:Sapphire laser wavelength is typically detuned about 0.5 nm to 2 nm from resonance to keep the polarization of the Cs vapor to less than 5%. This ensures that the spin-relaxation rate of the Cs atoms is only a single exponential [Happer72][Appelt98].

To detect the spin-relaxation rate of the Cs vapor we use an external cavity diode

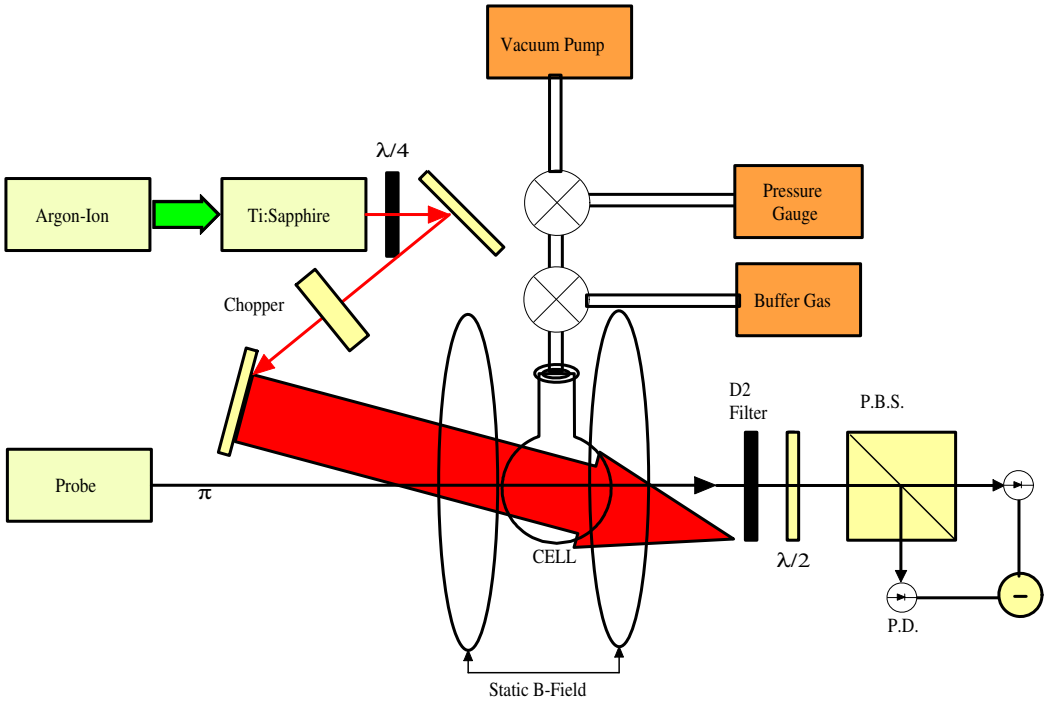

Figure 2.1: Cesium spin-relaxation experimental setup.

laser (5 mW at 850 nm, Intelite- part MLD850-5S5N) as a probe in the Littman-Metcalf configuration [Littman78]. We keep the power of the probe laser to less than 1 mW to ensure that there is no optical pumping of the Cs vapor by the probe laser.

2.3.2 Cell

The cell is a cylindrical stainless-steel chamber, shown in figures 2.2 and 2.3. The dimensions of the chamber are $1\frac{3}{8}''$ in diameter and $2.5''$ in length. The cell is first cleaned thoroughly and baked at about 300C for about 3 to 4 days to remove any impurities. After the cell is cooled down, high purity Cs is then introduced. The windows are then attached in the manner described in [Noble94] [Kadlecek00] with home-made knife-edge copper gaskets. We use plain pyrex circular discs as our windows ($2''$ diameter and $3/8''$ thick) and 30-40 sheets of aluminum foil as a pad between the

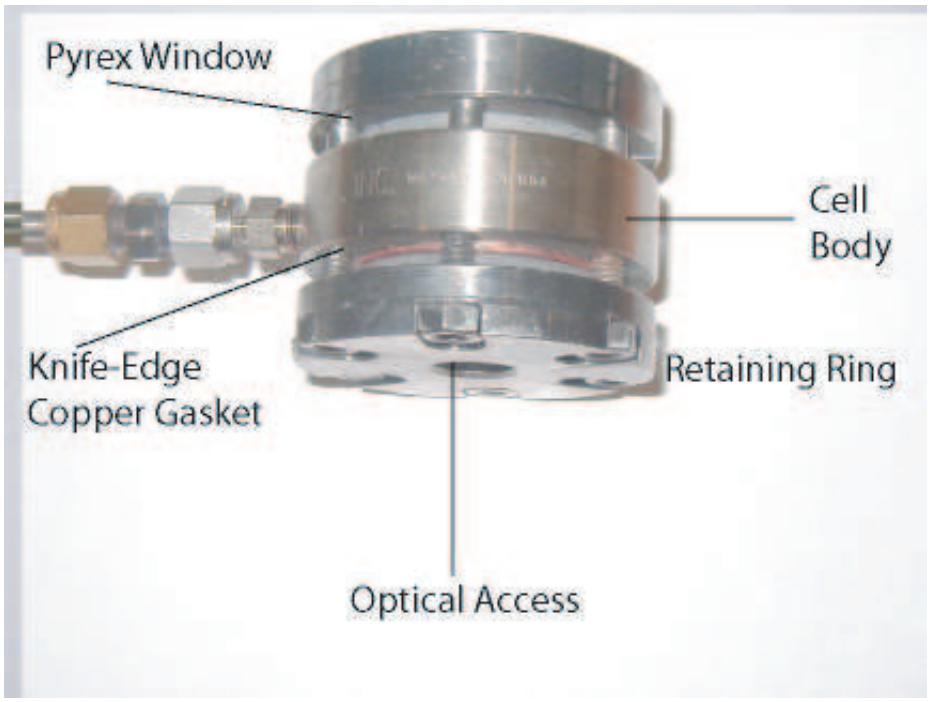

Figure 2.2: Stainless Steel Cesium Cell-From Top View

window and the stainless-steel retaining ring.

2.3.3 Polarization Detector

For our spin polarization detection, we use a polarization-Faraday rotation detector [Kadlecek98][Kadlecek00]. The optical setup is shown in figure 2.4. The detection is based on the birefringence of the alkali-atoms when it is spin-polarized. When linearly polarized light enters the cell, the polarization of the light gets rotated. The rotation is proportional to the polarization and density of Cs vapor. The detector is composed of a half-wave plate followed by a polarizing beam splitter and two photodiode detectors. The two photodiodes are wired to opposite polarity.

The signal detected is proportional to $\sin(P)$, where P is the Cs vapor polarization. Since the polarization is kept small, $\sin(P) \cong P$. At large detuning compared to

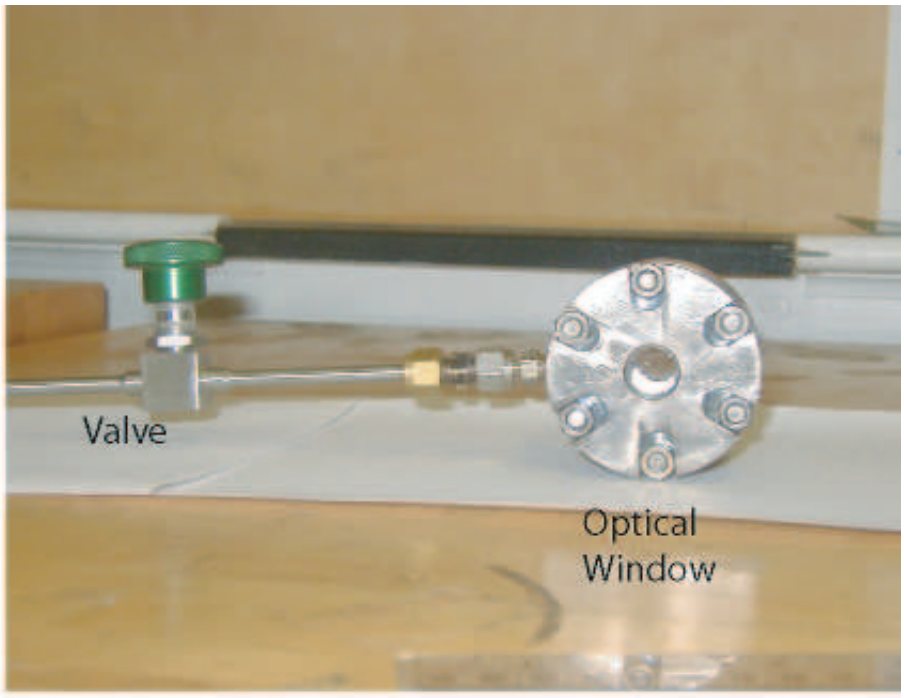

Figure 2.3: Stainless Steel Cesium Cell-From Side View

atomic linewidth and hyperfine structure, the Faraday rotation angle as a function of polarization is given as [Kadlecek00] [Vliegen01] (Appendix D)

$$\theta_P = \frac{[Cs]Le^2}{6mc}\left(\frac{1}{\Delta_{3/2}} - \frac{1}{\Delta_{1/2}}\right)P, \tag{2.3}$$

where L is the probe path length through the vapor and $\Delta_{3/2}$ $\Delta_{1/2}$ are the detunings from $P_{3/2}$ and $P_{1/2}$ resonances. [Cs] is the cesium density, m is the atomic mass, e is the electronic charge and c is the speed of light and P is the polarization. The absolute calibration is then obtained by measuring the rotation angle on the half-wave plate.

2.3.4 Relaxation Rate Measurements

The spin-relaxation signal [Franzen59] is usually averaged many times before being recorded. Typically, the number of averages ranges from 50 to 5000 times. The signal is then fitted to a single exponential. Care must be taken to make sure the Cs polarization

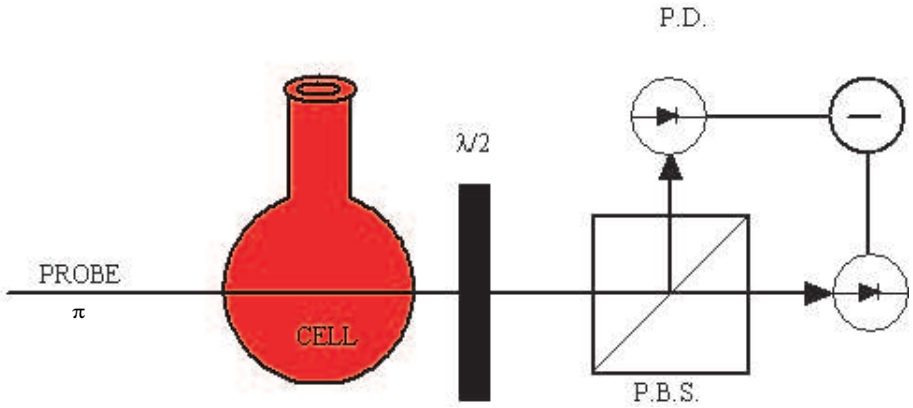

Figure 2.4: Our standard Faraday rotation detector used in most measurements in this thesis. The diagram for the cell is not an open flash as indicated in the diagram but valved as shown in figure 2.1.

is low. If the polarization is high, the signal is a linear combination of many exponentials from many different relaxation observables [Happer72]. A sample spin-relaxation signal and its residual fit is shown in figure 2.5.

2.3.5 Vapor Pressure Measurement

We use magnetic field-Faraday rotation to measure the Cs vapor density. In the large magnetic field (1 Tesla) that is used in our experiment, the rotation is typically on the order of many tens of degrees. This technique has been proven reliable up to 20 atmospheres of buffer gas [Vliegen01]. Also, our group has calibrated this technique to a much more laborious but very reliable technique using absorption spectroscopy of the second resonance [Kadlecek00].

The rotation angle, for the probe's detuning much greater than the atomic linewidth and hyperfine structure, as a function of Cs density and magnetic field is [Kadlecek00]

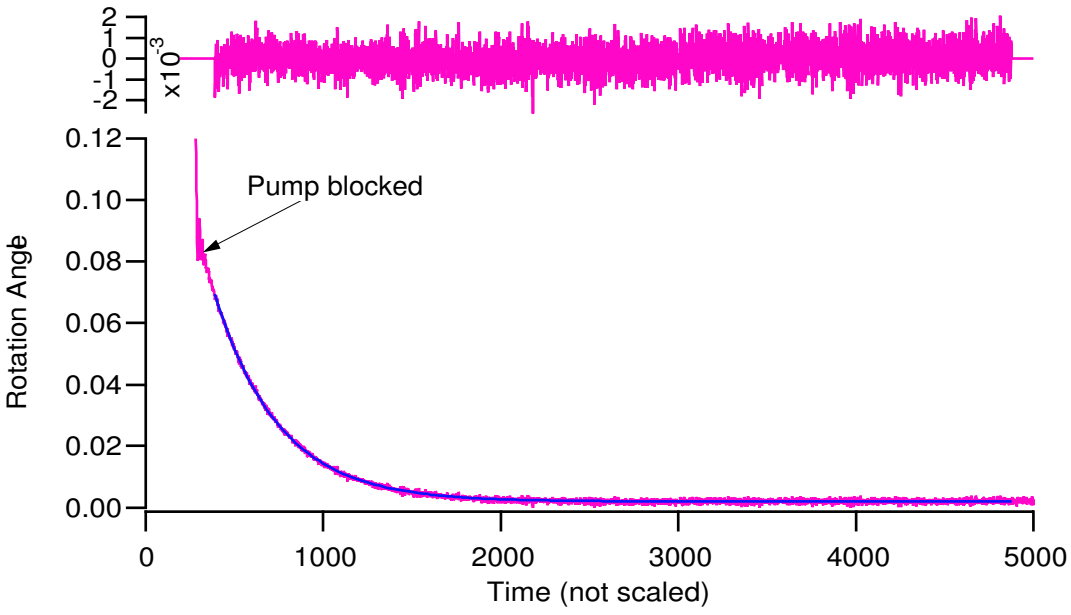

Figure 2.5: A sample exponential transient with an exponential fit with residual.

[Vliegen01] (Appendix D)

$$\theta_B = [Cs]\frac{Le^2\mu_B B}{18mhc}\left(\frac{4}{\Delta_{1/2}^2}+\frac{7}{\Delta_{3/2}^2}-\frac{2}{\Delta_{3/2}\Delta_{1/2}}\right), \tag{2.4}$$

where, for example, $\Delta_{3/2} = \nu - \nu_{3/2}$ is the detuning of the probe from the $nS_{1/2} \rightarrow nP_{3/2}$ transition. Here e is the electronic charge, μ_B is the Bohr magneton, m is the electron mass, h is Planck's constant, L is the path length of the probe through the cell, c is the speed of light, B is the external applied magnetic field, and $[Cs]$ is the Cs density. Thus, to measure the Cs density we measure the rotation angle as we change the magnetic field. We then plot the rotation angle as a function of the magnetic field and do a least square fit of a straight line. The slope of the line is proportional to the Cs density. A sample of the field-Faraday rotation is shown in figure 2.6.

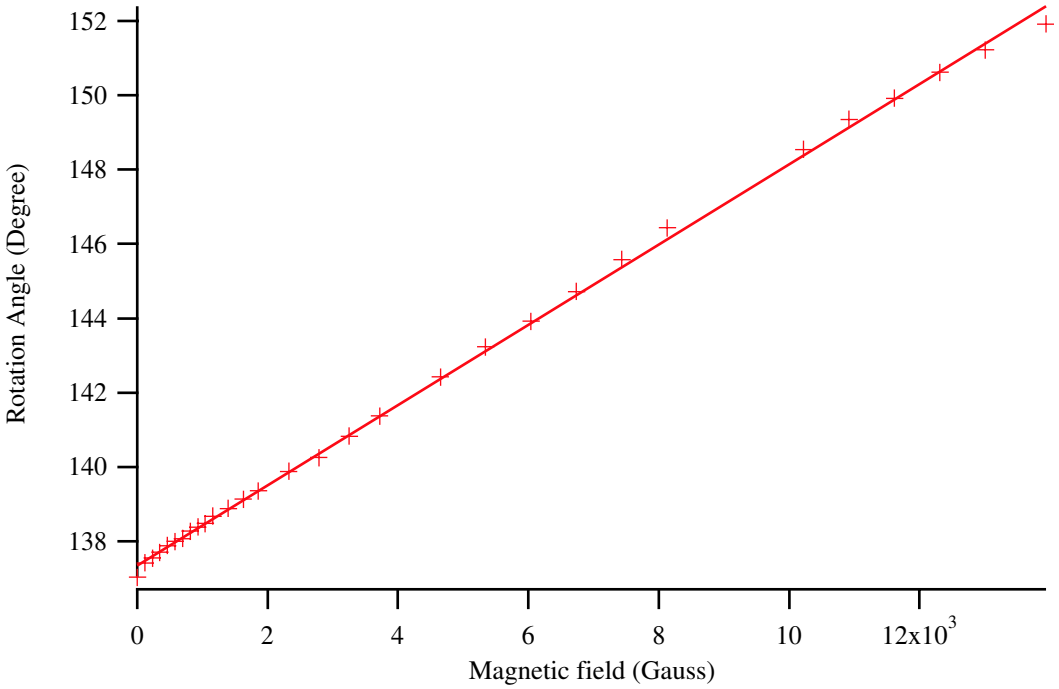

Figure 2.6: Rotation angle plotted as a function of applied magnetic field- the slope is proportional to Cs density. Also shown is the linear fit.

2.4 Spin-Relaxation in Triplet Dimers

2.4.1 Triplet Dimer Density

In a typical spin exchange optical pumping condition, about 0.01% of the Cs atoms are in triplet molecules. Unlike singlet dimers, the total electronic spin is not zero. Thus, fast spin-relaxation is possible through the magnetic coupling between the two electrons [Appelt98][Kadlecek00]. Other relaxation mechanisms like spin-rotation interaction and electric-quadrupole interaction [Kadlecek01] are much smaller.

To make any reasonable relaxation rate calculations due to triplet dimers, we need to know the triplet dimer density in the vapor. Unfortunately, it is extremely difficult to measure the triplet dimer density directly. So we are forced to deduce the triplet dimer from the atom density and the chemical equilibrium coefficient. We calculate the

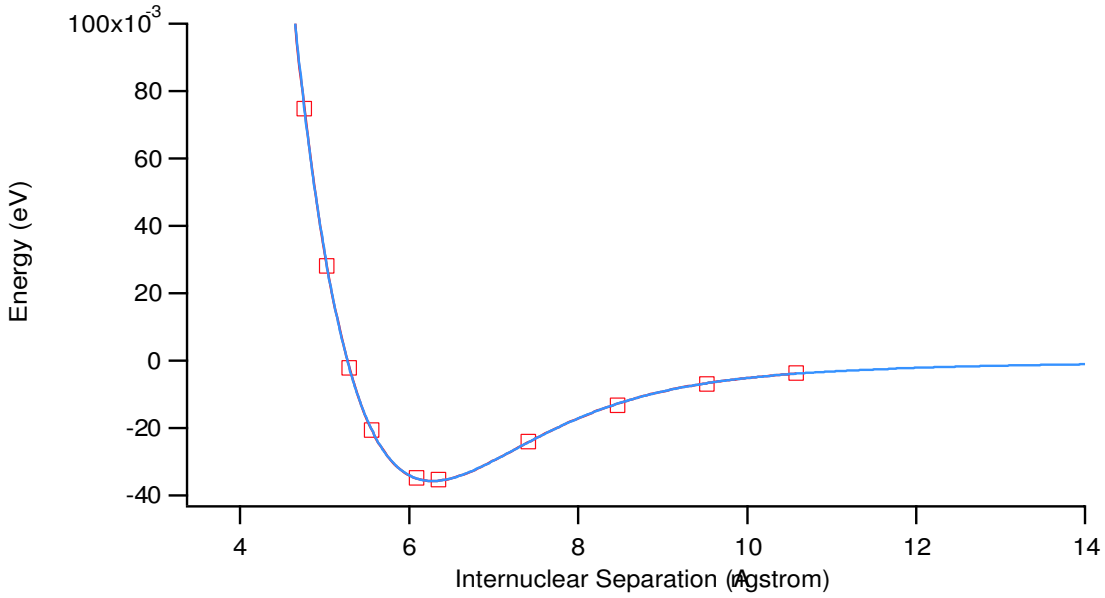

Figure 2.7: Cesium Triplet Potential- points are *ab initio* calculations of Krauss and Stevens [Krauss90], curve is a convenient fit to the potential.

chemical equilibrium using the *ab initio* potential calculated by Krauss and Stevens [Krauss90] which is shown in figure 2.7.

The relative motion of the pair of Cs atoms is reduced to the motion of the relative particle of mass [Bouchiat69]

$$\mu = \frac{m_1 m_2}{(m_1 + m_2)} \tag{2.5}$$

in the effective potential

$$U_{eff} = U(r) + \frac{N(N+1)\hbar^2}{2\mu r^2}, \tag{2.6}$$

where $\hbar N$ is the rotational angular momentum of the pair and r is the internuclear separation. $U(r)$ is the dominant term which describes the electrostatic exchange forces between the two atoms. The second term is the rotational energy of the pair.

The density of the triplet dimers can be deduced from the chemical equilibrium coefficient. From the law of mass action [Reif65], the chemical equilibrium coefficient,

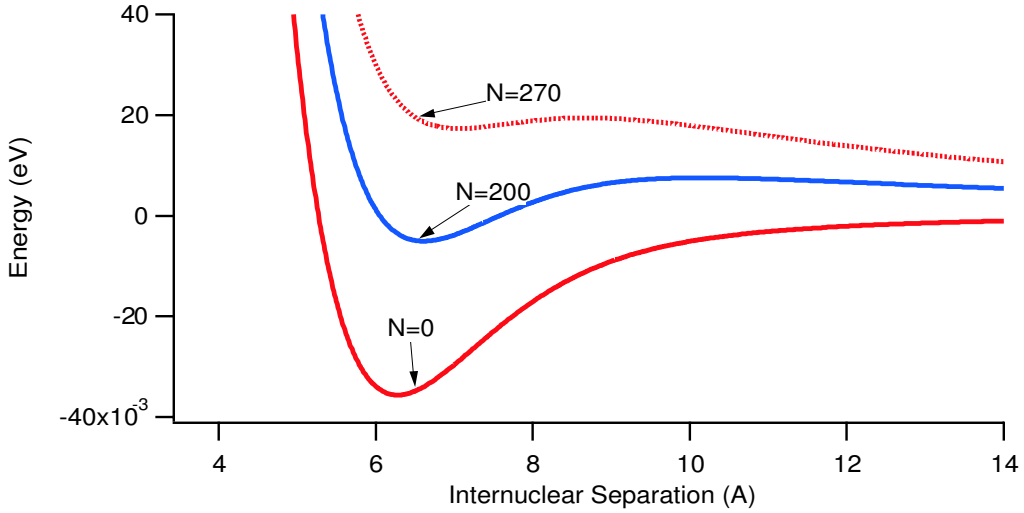

Figure 2.8: Cesium Triplet Potential...Here N is the rotational angular momentum of the molecule. Note at N=200, there is a region of bound states and quasi bound states, where energy is greater than zero.

${}^3\kappa_{chem}$, of the triplet molecules is given as:

$$ {}^3\kappa_{chem} = [{}^3Cs_2]/[Cs]^2, \tag{2.7} $$

where $[{}^3Cs_2]$ is the triplet dimer density.

First, from the *ab intio* potential of Krauss and Stevens [Krauss90] we numerically calculate all the bound eigenstates and eigenenergies using the Fourier Grid Hamiltonian method (Appendix A) [Marston89] [Balint-Kurti92] [Borisov01]. Figure 2.9 shows all the bound eigen-energies plotted as a function of the rotational angular momentum. From the eigen-energies we sum over all the states and weight it by the Boltzmann factor to determine the chemical equilibrium coefficient defined as [Kadlecek00][Kadlecek01]:

$$ {}^3\kappa_{chem} = \frac{3}{8}\left[\frac{h^2}{\pi mkT}\right]^{3/2} \sum_i e^{-E_i/kT}(2N_i+1), \tag{2.8} $$

The accuracy of ${}^3\kappa_{chem}$ depends critically on the accuracy of the *ab intio* potential. Since there is no experimental binding energy to scale the *ab intio* potential of Krauss

and Stevens [Krauss90] to, we are forced to estimate the error in ${}^3\kappa_{chem}$ from the chemical equilibrium coefficient in singlet molecules, ${}^1\kappa_{chem}$. The calculated ${}^1\kappa_{chem}$ of singlet molecules using *ab initio* potential and the calculated ${}^1\kappa_{chem}$ using *ab initio* potential scaled to the known binding energy differs by about 15% [Kadlecek01]. Thus, our calculated value of ${}^3\kappa_{chem,}$ in triplet molecules has an error of at least about 15% and probably more.

Note the chemical equilibrium coefficients calculated here are a bit off compared to Kadlecek's [Kadlecek00][Kadlecek01] calculation using conventional numerical iterations to find the eigenstates and energies. For example, at 500K Kadlecek calculated the chemical equilibrium coefficient for Cs to be 574 A^3, as compared to 515 A^3 in this thesis. The source of this discrepancy has not been found.

From the chemical equilibrium, we can deduce the triplet dimers density. Figure 2.11 shows the fraction of Cs atoms in triplet dimers.

2.4.2 Spin-Axis Interaction

The Hamiltonian for a homonuclear triplet dimers is [Appelt98] [Erickson00]

$$H = \frac{A}{2}\mathbf{S}\cdot\mathbf{I} - g_s\mu_B B S_z + \frac{2\lambda}{3}\mathbf{S}\cdot(3\hat{\xi}\hat{\xi} - \mathbf{1})\cdot\mathbf{S} + \gamma\mathbf{N}\cdot\mathbf{S} \tag{2.9}$$

Here A is the atomic magnetic-dipole hyperfine coupling coefficient, $\mathbf{I} = \mathbf{I}_1 + \mathbf{I}_2$ is the sum of the nuclear spin for the two atoms, $\mathbf{S} = \mathbf{S}_1 + \mathbf{S}_2$ is the total electron spin of the colliding pair, and $\hat{\xi}$ is the unit vector between the two atoms. $\mathbf{N}$ is the molecular angular momentum of the dimer. The first term in the Hamiltonian is the magnetic dipole hyperfine interaction between the nuclear and the electron. The second term is the interaction between the electron spin and the external magnetic field. The third term is the spin-axis interaction [Mies96]. The last term is the spin-rotation coupling between the electron spin and the molecular angular momentum N.

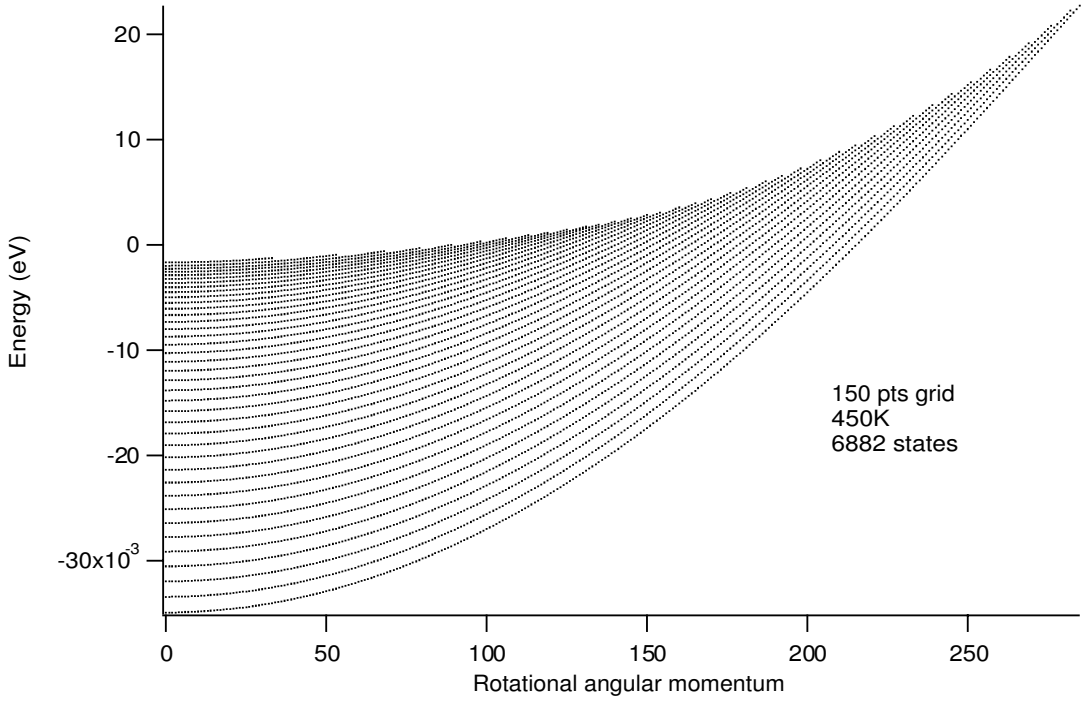

Figure 2.9: All bound triplet dimers eigen-energies plotted as a function rotational angular momentum at a temperature of 450K using a 150 points grid

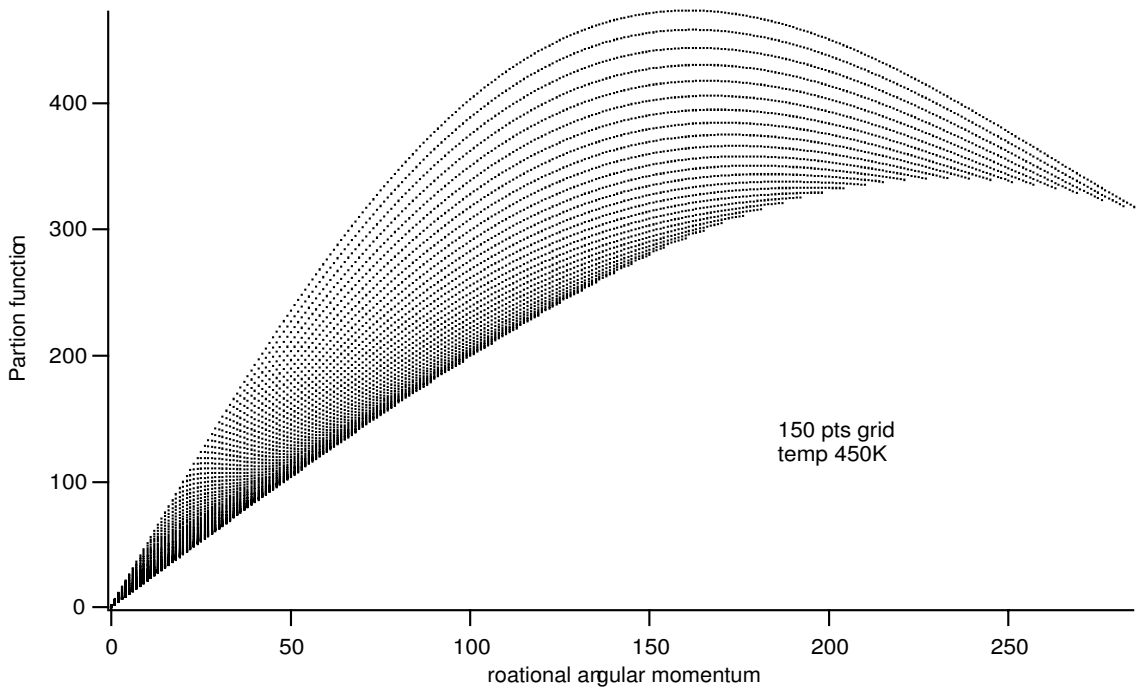

Figure 2.10: Plot showing partition function $Z = (2N_i+1)e^{-E_i/kT}$ plotted as a function rotational angular momentum, N, at a temperature of 450K

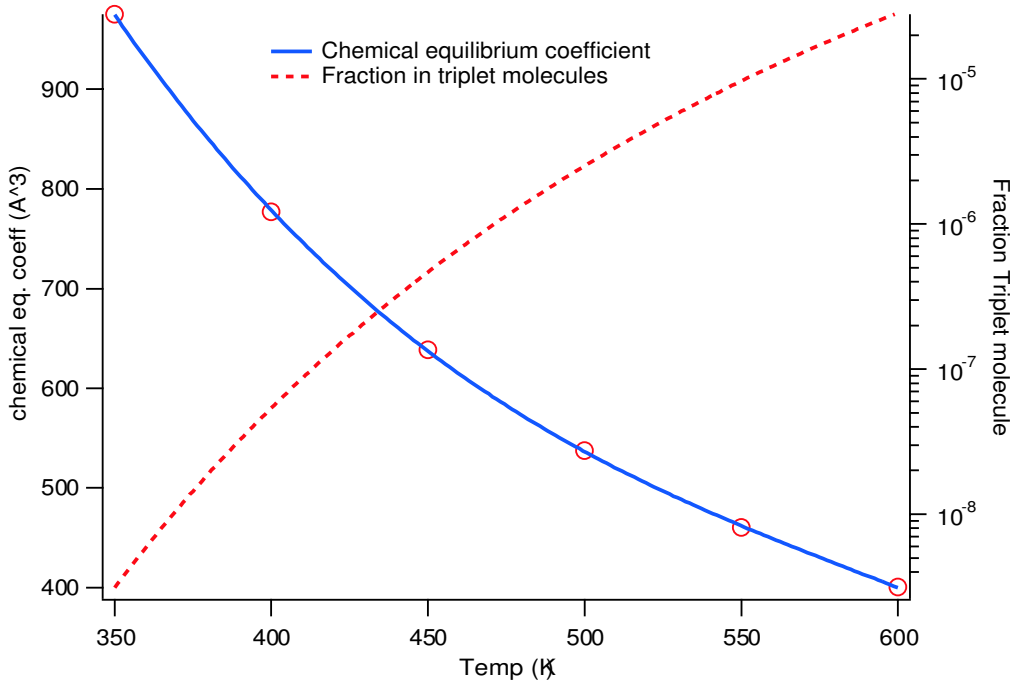

Figure 2.11: The graph shows the fraction of Cs atoms in triplet dimers as a function of temperature. Also shown is the chemical equilibrium coefficients of Cs triplet molecules as a function of temperature. Circles are numerical calculation using Fourier Grid Hamiltonian. Also shown is a polynomial fit of the form $\sum_{n=0}^{3} a_n x^n$with coefficients: 4972.7,-20.848,0.033194,-1.8665e-5

The spin-axis interaction term in the above Hamiltonian looks pretty obscure. To show it more clearly we need to write it in terms of the interaction between the total spin, **S**, and the molecular rotation, **N**. First we write the unit vector $\hat{\xi}$ in terms of its rectangular coordinate,

$$\hat{\xi} = \cos\theta\cos\omega t\hat{x} + \sin\omega t\hat{y} - \sin\theta\cos\omega t\hat{z}, \tag{2.10}$$

where θ is the angle between the rotational angular momentum and the quantization axis $\hat{z}$, and ω is the angular velocity of the molecule. The spin-axis term from equation 2.9 can be written as

$$\frac{2\lambda}{3}(3(\mathbf{S}\cdot\hat{\xi})^2 - \mathbf{S}^2). \tag{2.11}$$

Since the second term does not couple to anything, we do not need to worry about it. Expanding the first term as

$$(\mathbf{S}\cdot\hat{\xi})^2 = S_x^2\hat{\xi}_x^2 + 2\hat{\xi}_x\hat{\xi}_y S_x S_y + 2\hat{\xi}_z\hat{\xi}_x S_z S_x + 2\hat{\xi}_z\hat{\xi}_y S_z S_y + \hat{\xi}_z^2 + \hat{\xi}_y^2 \tag{2.12}$$

Substituting the unit vector from equation 2.10 and averaging over time the result equation is

$$(\mathbf{S}\cdot\xi)^2 = \frac{1}{2}\cos^2\theta S_x^2 + \frac{1}{2}S_y^2 + \frac{1}{2}\sin^2\theta S_z^2 - \frac{1}{4}\sin^2\theta(S_xS_y + S_yS_x). \tag{2.13}$$

From this last equation, it can be shown easily that

$$\frac{S^2}{2} - \frac{1}{2}(\mathbf{S}\cdot\hat{n})^2 = (\mathbf{S}\cdot\hat{\xi})^2, \tag{2.14}$$

where $\hat{n}$ is the unit vector pointing along the rotational angular momentum of the pairs. Thus, the full Hamiltonian becomes

$$H = \frac{A}{2}\mathbf{S}\cdot\mathbf{I} - g_s\mu_B B S_z - \frac{\lambda}{3}\mathbf{S}\cdot\Big(3\hat{n}\hat{n} - 1\Big)\cdot\mathbf{S} + \gamma\mathbf{N}\cdot\mathbf{S} \tag{2.15}$$

2.4.3 Spin-Relaxation Due to Spin-Axis Interaction

The relaxation rate caused by the spin-axis interaction can be derived from a density matrix model [Happer72][Erickson00]. Let us define the triplet dimer total spin angular momentum as

$$G_z = S_z + I_{1z} + I_{2z}, \tag{2.16}$$

where $I_{1,2z}$ are the projections of the nuclear spin of the two alkali atoms along the quantization axis, and $S_z = S_{1z} + S_{2z}$ is the total electron spin projection. Assuming that the Cs atoms are in spin-temperature equilibrium, the initial density matrix of the triplet dimers is a Boltzmann distribution and will be very nearly [Anderson59][Happer72]

$$\rho(t=0) = \frac{e^{\beta G_z}}{Z(\beta, G)} = \frac{\mathrm{e}^{\beta \mathrm{G_z}}}{\mathrm{Z}(\beta, \mathrm{I_1})\mathrm{Z}(\beta, \mathrm{I_2})\mathrm{Z}(\beta, \mathrm{S})}, \tag{2.17}$$

where β is the spin-temperature parameter, and related to the polarization, P, as [Happer72]

$$\beta = 2 \tanh^{-1} P. \tag{2.18}$$

Z is a partition function and for an arbitrary spin K it is equal to [Happer72]

$$Z(\beta, K) = \frac{\sinh\Big[\beta(\mathrm{K} + 1/2)\Big]}{\sinh(\beta/2)}. \tag{2.19}$$

When the polarization is low, or $\beta \ll 1$, the partition function is roughly

$$Z(\beta, K) \simeq (2K + 1). \tag{2.20}$$

Thus, in the low polarization limit, which is the case for our experiment, the initial density matrix of equation 2.17 becomes

$$\rho(t=0) \equiv \rho_0 \simeq \frac{(1 + \beta \mathrm{G_z})}{3(2\mathrm{I_m} + 1)^2}, \tag{2.21}$$

where $S = 1$ is assumed, and I_m is the monomer alkali nuclear spin .

The total average spin stored in the triplet dimer at the instant of formation can be defined as

$$\langle G_{z0}\rangle = \langle I_{1z}\rangle + \langle I_{2z}\rangle + \langle S_z\rangle, \tag{2.22}$$

where [Happer72]

$$\langle I_z\rangle = (I_m + 1/2)\coth\Big[\beta(I_m + 1/2)\Big] - 1/2\coth(\beta/2) \tag{2.23}$$

$$\langle S_z\rangle = 1/2\tanh(\beta/2) \tag{2.24}$$

In the low polarization limit the above equations reduce to

$$\langle I_z\rangle \simeq \beta I_m(I_m + 1)/3 \tag{2.25}$$

$$\langle S_z\rangle \simeq \beta S(S + 1)/3 \tag{2.26}$$

Substituting the last two equations into ($\langle G_{z0}\rangle$) of equation 2.22 we get the average total spin at the instant of formation to be

$$\langle G_{z0}\rangle = 2(I_m^2 + I_m + 1)\beta/3 \tag{2.27}$$

We are interested in calculating the relaxation rate coefficient, thus we need to calculate the mean change, $\langle \Delta G_z\rangle$, in the total triplet dimer spin due the Hamiltonian in equation 2.9. According to the density matrix theory this is just

$$\langle \Delta G_z\rangle = Tr\Big[G_z \Delta\rho\Big], \tag{2.28}$$

where $\Delta\rho$ is the mean change in the density matrix after it evolves by the Hamiltonian and given as

$$\Delta\rho = \rho_t - \rho_0 = U\rho_0 U^{-1} - \rho_0. \tag{2.29}$$

U is the time evolution operator and equal to

$$U = e^{iHt/\hbar} = \sum_i |i\rangle\langle i| e^{-iE_i t/\hbar}, \tag{2.30}$$

where $|i\rangle$ are the eigen-states that diagonalize the Hamiltonian H

$$H|i\rangle = E_i|i\rangle \tag{2.31}$$

The coherent evolution of the triplet dimers is, of course, interrupted by collisions. If we assume that each collision dissociates the molecule, which is most likely true since the well depth is on the order of kT, then the triplet dimers' lifetime is the same as the period between collisions. The coherent evolution is expected to be Poisson distributed as

$$P(t) = \frac{\mathrm{e}^{-\mathrm{t}/\tau}}{\tau}. \tag{2.32}$$

Thus, we also need to average equation 2.29 over the collisional lifetime of the molecules. Therefore, the change in total spin is

$$\langle \Delta G_z \rangle = \int_0^\infty \frac{\mathrm{dt}}{\tau} e^{-t/\tau} Tr\Big[G_z\Big[U\rho_0 U^{-1} - \rho_0\Big]\Big]. \tag{2.33}$$

Substituting for ρ_0 and U in the above equation we get

$$\begin{aligned} \langle G_z \rangle &= \int_0^\infty \frac{\mathrm{dt}}{\tau 3(2\mathrm{I_m}+1)^2} e^{-t/\tau} Tr\left[G_z([\sum_{ij}(|i\rangle\langle i|e^{i\omega_{ij}t}(1+\beta G_z)|j\rangle\langle j|)] - (1+\beta G_z))\right] \\ &= \sum_{ij} \frac{-\beta\omega_{\mathrm{ij}}^2\tau^2\langle \mathrm{j}|\mathrm{G_z}|\mathrm{i}\rangle\langle \mathrm{i}|\mathrm{G_z}|\mathrm{j}\rangle}{(1+\omega_{\mathrm{ij}}^2\tau^2)3(2\mathrm{I_m}+1)^2} \end{aligned} \tag{2.34}$$

Here $\omega_{ij} = (E_i - E_j)/\hbar$ are the Bohr frequencies.

The spin destruction probability is then [Erickson00]

$$\begin{aligned} W &= -\frac{\langle \Delta \mathrm{G_z}\rangle}{\langle \mathrm{G_{z0}}\rangle} \\ &= 2\sum_{ij} \frac{\omega_{\mathrm{ij}}^2\tau^2\langle \mathrm{j}|\mathrm{G_z}|\mathrm{i}\rangle\langle \mathrm{i}|\mathrm{G_z}|\mathrm{j}\rangle}{(1+\omega_{\mathrm{ij}}^2\tau^2)(2\mathrm{I_m}+1)^2[(2\mathrm{I_m}+1)^2+3]} \\ &= 2\sum_{ij} \frac{\omega_{\mathrm{ij}}^2\tau^2|\langle \mathrm{i}|\mathrm{G_z}|\mathrm{j}\rangle|^2}{(1+\omega_{\mathrm{ij}}^2\tau^2)(2\mathrm{I_m}+1)^2[(2\mathrm{I_m}+1)^2+3]} \end{aligned} \tag{2.35}$$

The spin destruction probability has to be averaged all over directions of $\hat{n}$

$$\begin{aligned} W_T &= \frac{1}{4\pi}\int_0^\pi \sin\theta d\theta \int_0^{2\pi} d\phi W \\ &= \frac{1}{2}\int_0^\pi \sin\theta d\theta W \end{aligned} \tag{2.36}$$

In the typical pumping cell, almost all the spin is carried by the Cs monomer. Using equations 2.25 and 2.26, the monomer spin density per unit volume can be shown to be [Erickson00]

$$\frac{[Cs]\beta(4I_m^2+4_m+3)}{12}. \tag{2.37}$$

The spin loss rate per unit volume from triplet dimers is [Erickson00]

$$\frac{[^3Cs_2]\langle\Delta G_z\rangle}{\tau}, \tag{2.38}$$

from which we can get the relaxation rate due to triplet dimers as

$$\begin{aligned}\Gamma_3 &= 2\left[\frac{(2I_m+1)^2+3}{(2I_m+1)^2+2}\right]\frac{W(^3\kappa_{chem})}{\tau} \\ &= \eta\frac{W}{T_F},\end{aligned} \tag{2.39}$$

where $T_F = 2(^3\kappa_{chem})/\tau$ is the formation rate, η is equal to 1.015 for Cs.

2.4.4 Average Spin-destruction During a Triplet Dimer Lifetime

So far we have assumed that each collision breaks up the molecule. In the case that collisional reorientation does not lead to breakup of the molecule, the average spin-destruction probability will change and can be derived as follows [Kadlecek00] [Kadlecek01].

If an atom undergoes N coherence before exiting the molecule, then the fractional polarization remaining is

$$\Big[1-(1-W)^N\Big]. \tag{2.40}$$

Thus, if P(N) is the probability of getting N coherences, then the average fractional polarization loss is

$$\bar{W} = \sum_{N=1}^{\infty} P(N)\Big[1-(1-W)^N\Big] = 1-\sum_{N=1}^{\infty} P(N)(1-W)^N. \tag{2.41}$$

It can be shown that [Kadlecek00] [Kadlecek01]

$$P(N) = \frac{\tau_b^{N-1}\tau_J}{(\tau_b + \tau_J)^N}, \tag{2.42}$$

where τ_b is the molecular breakup lifetime and τ_j is the time at which a triplet dimer is subject to decoherence from collisions with a buffer gas without breakup. Therefore,

$$\bar{W} = 1 - \frac{\tau_J}{\tau_b}\sum_{N=1}^{\infty}\left[\frac{\tau_b(1-W)^N}{\tau_b + \tau_J}\right]^N = \frac{(1+\langle N\rangle)W}{1+\langle N\rangle W}, \tag{2.43}$$

$\langle N\rangle = \tau_b/\tau_J$ is the average number of reorientation before dissociation and $\tau_b = \frac{1}{\langle\sigma_b v\rangle[N2]}$, $\tau_j = \frac{1}{\langle\sigma_j v\rangle[N2]}$ [Kadlecek00][Kadlecek01].

2.5 Data and Discussion

The experimental Cs spin-relaxation magnetic decoupling curves are fitted to the form

$$\Gamma \;=\; \Gamma_b + \Gamma_3 = \Gamma_b + \eta\frac{W(\lambda/A, A\tau_b/\hbar, \hbar\Omega/A)}{T_F},$$

where Γ_b is the background spin-relaxation. Here Γ_b is independent of the magnetic field. They are known to come from Cs-N_2 collisions, Cs-Cs binary collisions, diffusion and possibly singlet molecules. Γ_3 is the triplet spin-relaxation rate and is given in equation 2.39. $\hbar\Omega = 2\mu_B B$ is the Zeeman interaction.

Therefore, the fit parameters are Γ_b, $1/T_F$, λ/A, and, in the case of collisional reorientations without breakup, N. Our 84torr data is first fitted by allowing all the free parameters to vary. In subsequent fits to the rest of the data, λ and N are held fixed. Also, since the coherence time τ_c should be inversely proportional to the gas pressure, all the coherence times as a function of pressure are scaled to the 84 torr fit τ_c. Thus, in all subsequent fits only Γ_b and $1/T_F$ are allowed to vary.

Graph 2.12 shows the data and the fit at N_2 buffer gas of 84 torr. There should be seven resonances spin-relaxation due to anti-crossing of the Hamiltonian as predicted

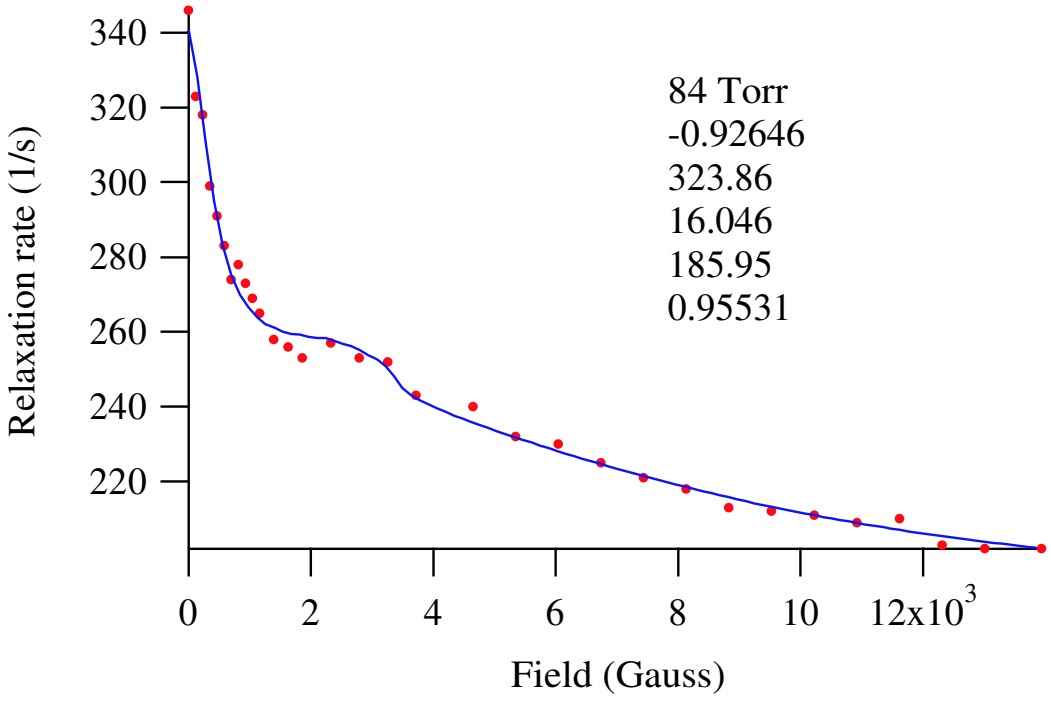

Figure 2.12: Graph showing relaxation (1/s) as a function of magnetic field (gauss) at N2 buffer gas pressure of 84 torr. The fit parameters are listed top to bottom, λ/A, the formation rate $(1/T_F)$ in unit of $(1/s)$, $A\tau/\hbar$, and the background rate Γ_b in unit of $(1/s)$, and the average number of reorientations before breakup N. Notice the "bump" around 2000 gauss, where the 7 resonances are supposed to be.

by the spin-axis interaction at the magnetic fields [Erickson00]

$$\begin{aligned} B_I &= \frac{A(2I+1)}{4g_s\mu_B} \\ &= (616, 1026, 1436, 1847, 2257, 2668, 3078) \text{ Gauss.} \end{aligned} \tag{2.44}$$

Notice the "bump" around 2000 gauss, where the 7 resonances predicted by the spin-axis interaction are supposed to be. Graphs 2.13 through 2.16 show the data and the fit up to N_2 buffer gas of 690 torr. The data fits very nicely up to 390 torr. At 690 torr it does not fit that well anymore.

Here is the summary of the fit parameters. Using the negative value of λ and allowing for collisional reorientation without breakup, the fit parameter gives $A\tau_c/\hbar = 16.046$ in the 84 torr of N_2 data. Hence, the deduced coherence time can be parametrized to the 84 torr of N_2 as

$$\tau_c = (\frac{84 \text{ torr}}{P})11.20 \times 10^{-10} \text{ s}, \tag{2.45}$$

where $A/\hbar = 2.28$ GHz and P is the buffer gas pressure in the unit of torr. The density of 84 torr of N_2 buffer gas at the cell temperature of 450K is 1.8×10^{18} cm^{-3}. The relative velocity between the N_2 and Cs atom is 6.14×10^4cm/s at this temperature. This gives the cross section

$$\sigma_c = \frac{1}{\langle v\tau_c \rangle [N_2]} = 80.8 \text{ A}^2. \tag{2.46}$$

Since $\frac{1}{\tau_c} = \frac{1}{\tau_b} + \frac{1}{\tau_j}$ and $\sigma_c = \sigma_b + \sigma_j$, using the fit parameter for $N = 0.995531$ gives

$$\sigma_b = 40.5 \text{ A}^3 \tag{2.47}$$

$$\sigma_j = 40.3 \text{ A}^3 \tag{2.48}$$

The deduced formation rate in 84 torr is 4.1723/(sec torr). Also from the fit, the value for λ is

$$\lambda = -2.13 \text{ GHz}. \tag{2.49}$$

Using these values we can find the chemical coefficient (${}^3\kappa_{chem}$)

$$\begin{aligned} {}^3\kappa_{chem} &= \frac{\tau_c(1+N)}{2T_F[Cs]} \\ &= 584 \text{ A}^3, \end{aligned} \tag{2.50}$$

where $[Cs] = 6 \times 10^{14}$ cm^{-3}.

These fit parameters are reasonable. The fit value of $N \approx 1$ implies that the breakup cross section is about same as the reorientation cross section. Even though the well depth is about KT, this does not seem to be outrageous. Also the calculated ${}^3\kappa_{chem}$ from Krauss and Stevens *ab initio* potential curve, which are believed to be very reliable, at 450K using Fourier Grid is 613 A^3 or about 5% different from the fit parameter. This is very favorable since at best our calculated chemical coefficient error is at least 15%.

Using the opposite sign of λ the fit parameters are

$$\lambda = 2.71 \text{ GHz}, \tag{2.51}$$

$$\sigma_c = 93 \text{ A}^3, \tag{2.52}$$

$$\sigma = 55 \text{ A}^3, \tag{2.53}$$

$${}^3\kappa_{chem} = 431 \text{ A}^3. \tag{2.54}$$

Using the negative value λ allowing no collisional reorientation, the data are well fitted by

$$\lambda = -2.9 \text{ GHz}, \tag{2.55}$$

$$\sigma = 98 \text{ A}^3, \tag{2.56}$$

$${}^3\kappa_{chem} = 350 \text{ A}^3. \tag{2.57}$$

Assuming the opposite sign o f λ we get

$$\lambda = 3.4 \text{ GHz}, \tag{2.58}$$

$$\sigma = 82 \text{ A}^3, \tag{2.59}$$

$$^3\kappa_{chem} = 307 \text{ A}^3. \tag{2.60}$$

At buffer gas pressures of an amagat or more, spin-relaxation rate decoupling curves are independent of the buffer gas pressures. As expected, the fit gets worse as a function of increasing buffer gas pressure. It is a mystery at this time. If all the alkali-alkali spin-relaxation comes from triplet molecules or molecules in general, the spin-relaxation rate contribution from the molecules should vanish as the buffer gas pressure is increased since the formation of the molecules has $T_F \propto 1/[B]$ dependent.

Unlike the Princeton data in Rb, our Cs data, unfortunately, do not show the distinct seven resonances spin-relaxation due to anti-crossing of the Hamiltonian as predicted by the spin-axis interaction. This is most likely due to the closeness of the seven peaks to each other. We wanted to emphasize that single values of λ and σ_c accurately describe all the magnetic decoupling spin-relaxation curves from 10 torr to 690 torr of N_2 buffer gas.

2.6 Cesium Spin-Relaxation with Buffer Gas

At buffer gas pressure of an amagat or more, a small fraction of Cs spin-relaxation comes from collisions with buffer gas. Although the interaction time is very short, there is a small probability that the Cs atoms loose some of their spin during collisions with the buffer gas. The relaxation rate depends only on the buffer gas density. The relaxation rate can be written as

$$\Gamma_B = [B]\langle\sigma v\rangle, \tag{2.61}$$

where $[B]$ is the buffer gas density and $\langle\sigma v\rangle$ is the velocity average spin-destruction cross section between the alkali-atom and the buffer gas. The microscopic mechanism

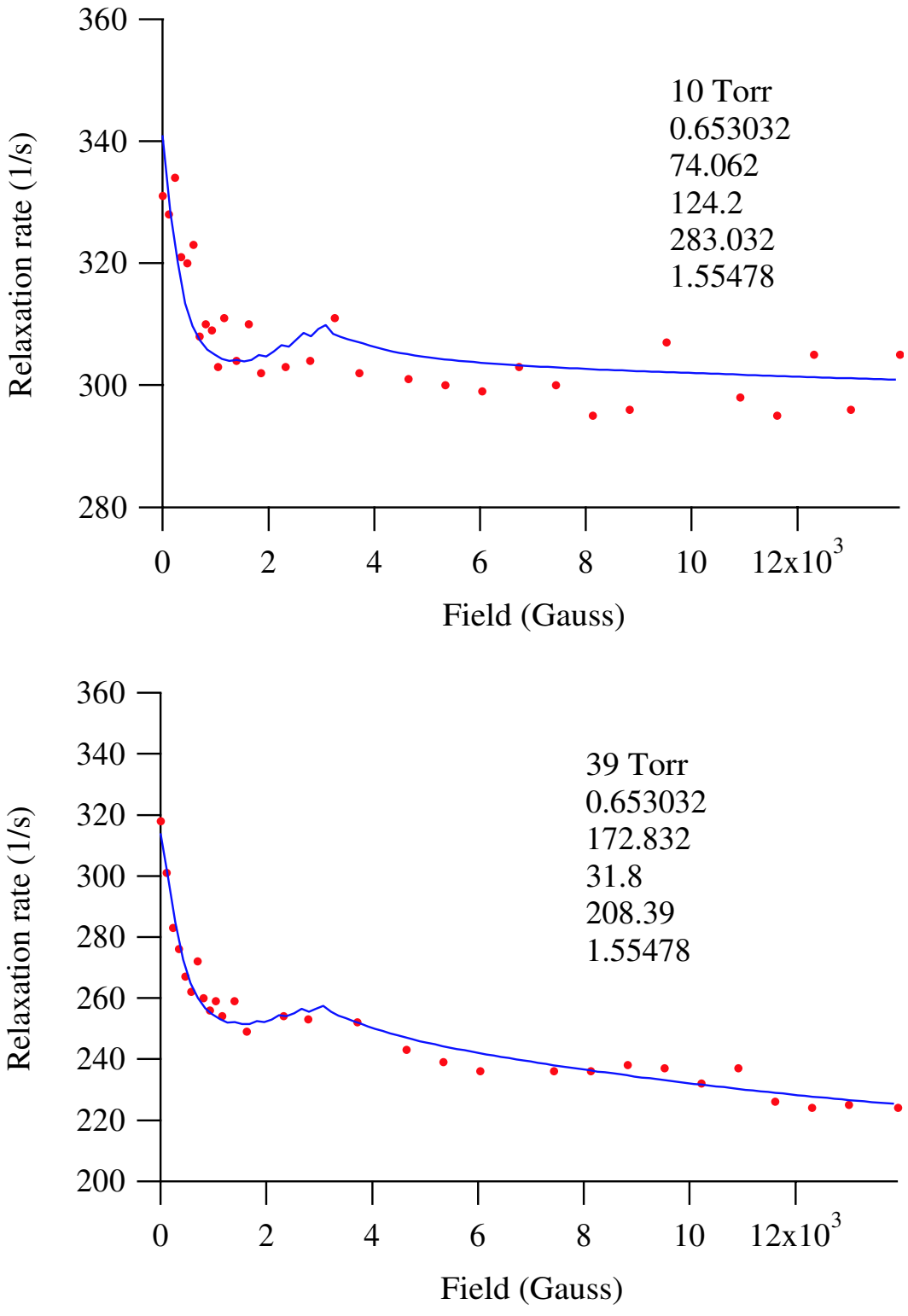

Figure 2.13: Graphs showing relaxation (1/s) as a function of magnetic field (gauss) at N2 buffer gas pressures 10 torr and 39 torr.

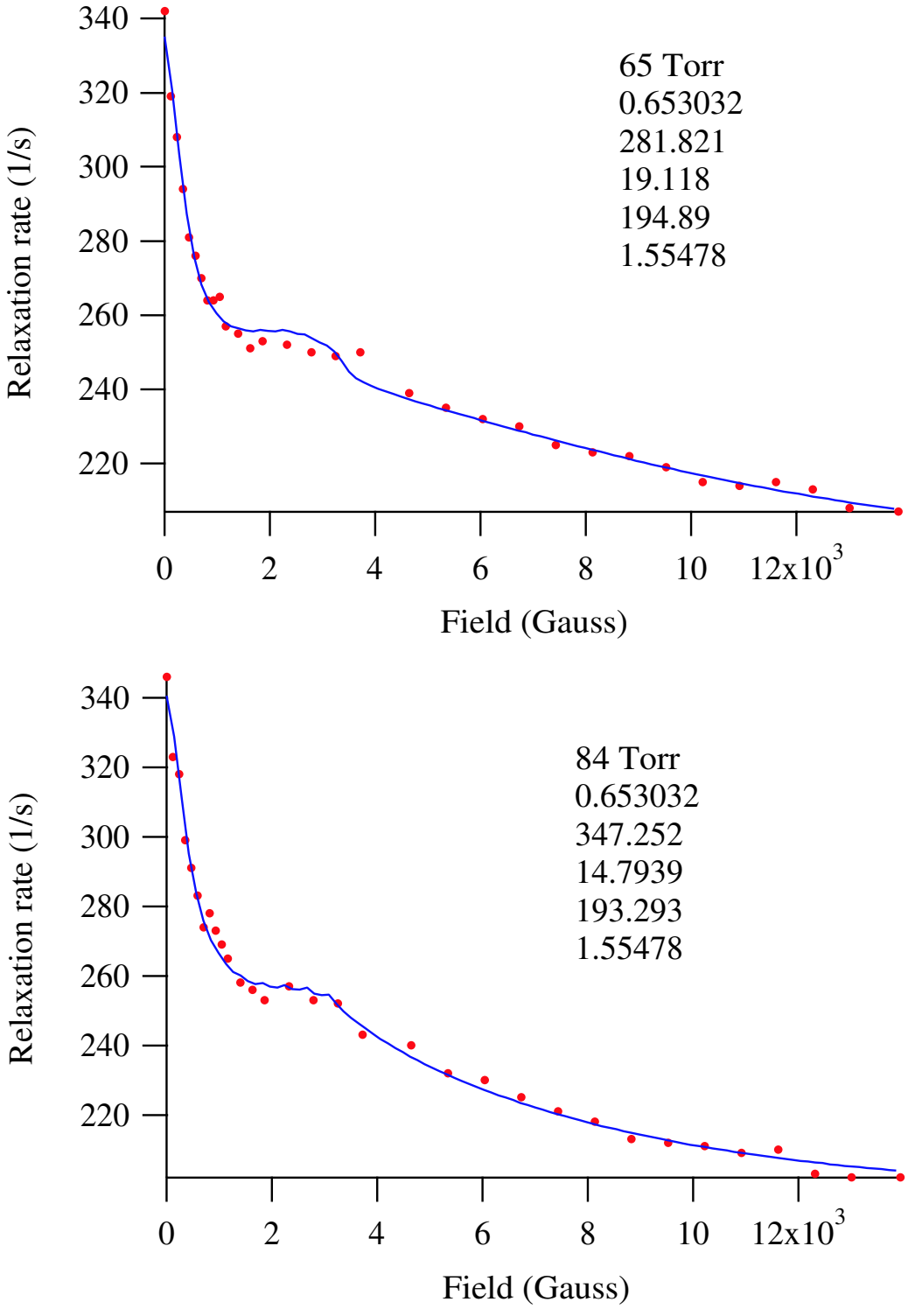

Figure 2.14: Graphs showing relaxation (1/s) as a function of magnetic field (gauss) at N2 buffer gas pressures 65 torr and 84 torr.

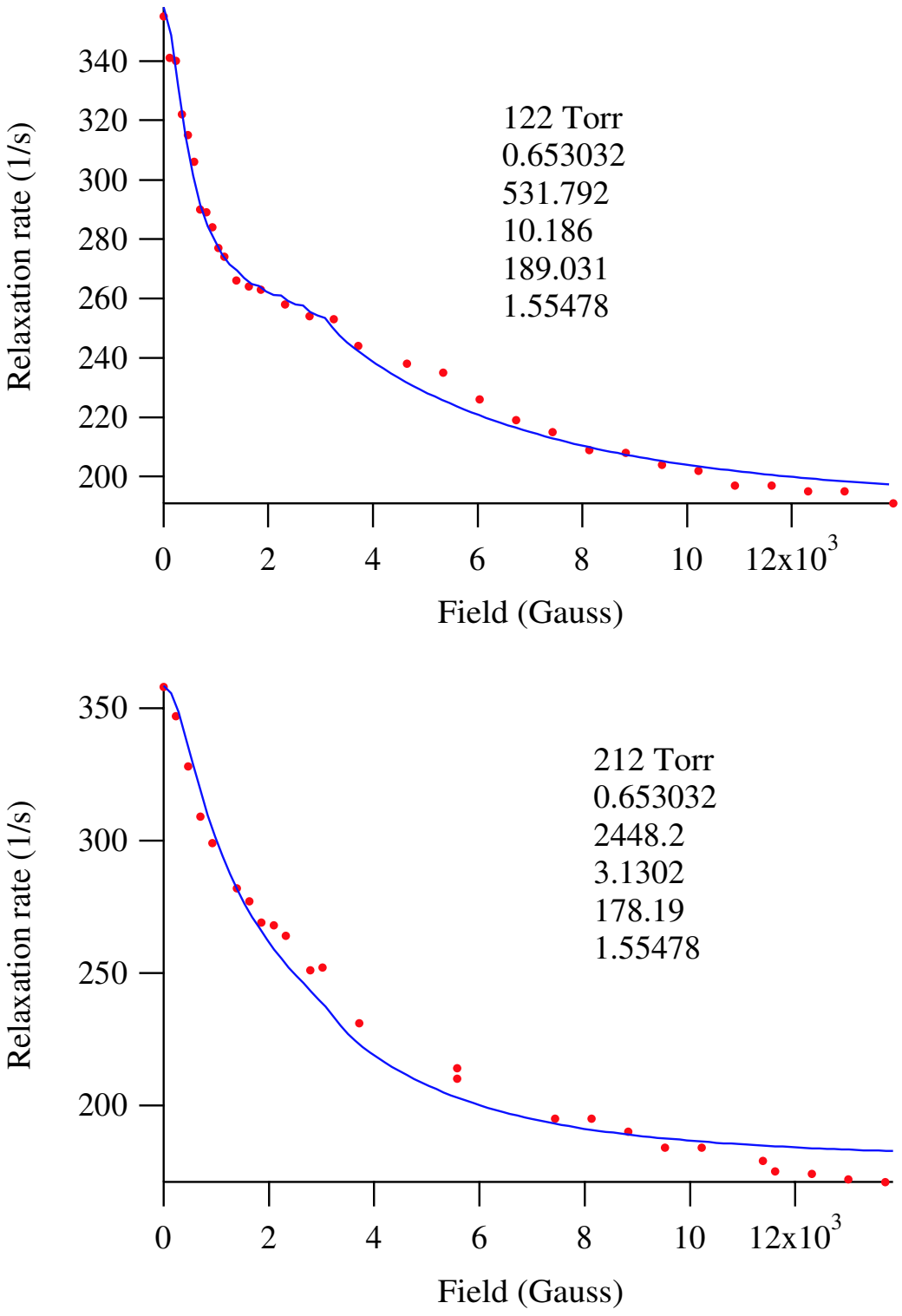

Figure 2.15: Graphs showing relaxation (1/s) as a function of magnetic field (gauss) at N2 buffer gas pressures 122 torr and 212 torr.

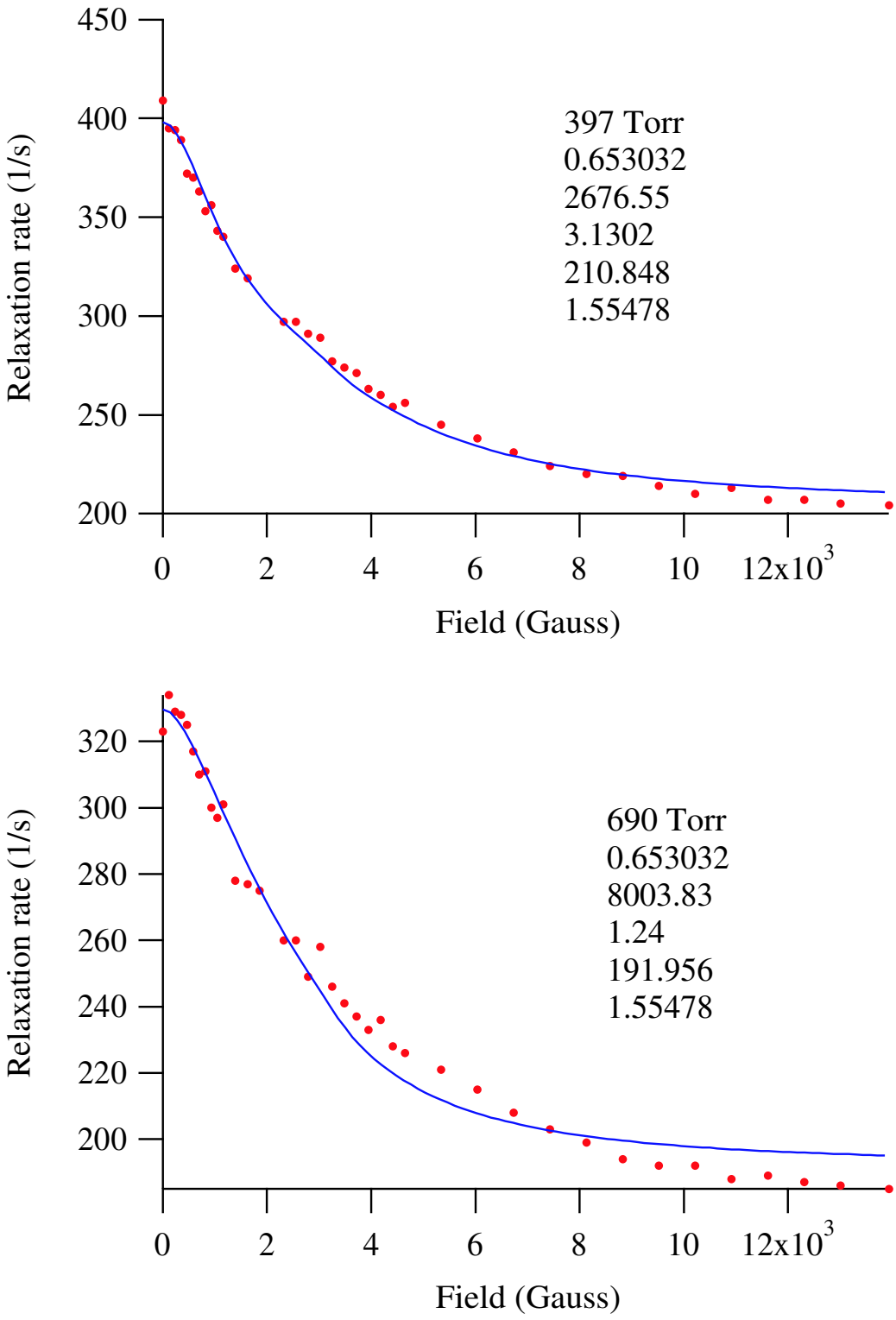

Figure 2.16: Graphs showing relaxation (1/s) as a function of magnetic field (gauss) at N2 buffer gas pressures 397 torr and 690 torr.

behind this spin-relaxation most likely arises from the spin-rotation interaction in the alkali-metal-buffer gas pairs [Walker89].

From figure 2.17 the fitted-spin-relaxation due to Nitrogen buffer gas is

$$0.058 \pm 0.0026/(\text{torr s}), \tag{2.62}$$

where the Cs density is ($5.6e14$ cm$^-3$) or the temperature of about 444K. The relative velocity of the of the nitrogen buffer gas and cesium atom at this temperature is about ($1.1e5$cm/s). Thus, the collisonal cross section is

$$\begin{aligned} \sigma_{N_2-Cs} &= \frac{0.058 \times 760 \times 22}{(1.1 \times 10^5)(2.69 \times 10^{19})(273/444)}\ \text{cm}^2 \\ &= 38.6 \times 10^{-22}\ \text{cm}^2, \end{aligned} \tag{2.63}$$

where the number 22 in the first equation is the slowing down factor of Cesium atoms [Happer72] [Appelt98]. Also from the figure, the spin-relaxation due to the Helium buffer gas is

$$0.0146 \pm 0.0011/(\text{torr s}) \tag{2.64}$$

At this temperature the relative velocity of the Helium atom is about ($2.7e5$ cm/s). Thus, the spin-destruction cross section between Helium and Cesium atoms is about

$$\sigma_{He-Cs} = 6.3 \times 10^{-22}\text{cm}^2. \tag{2.65}$$

This cross section is about a factor of ten bigger compared to the calculated value of (0.6×10^{-22}cm^{-3}) [Walker89]. This is expected since the measured spin-relaxation cross section for other alkali-^{4}He buffer gas is also about a factor of ten bigger than the calculated value. This is most likely due to the uncertainty in potentials used in the calculations.

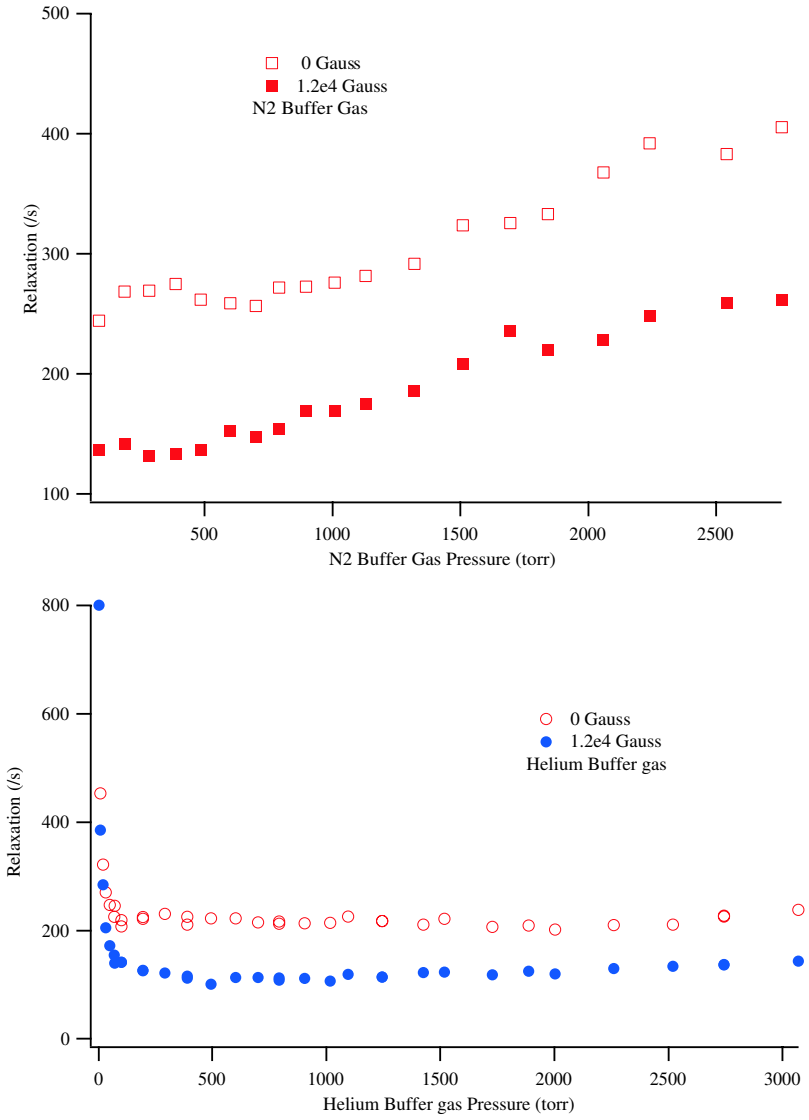

Figure 2.17: Graphs showing relaxation (1/s) as a function of buffer gas pressures in 0 and 1.2e4 Gauss of magnetic field

2.7 Summary

The Cs-Cs experiment described here, along with the Rb-Rb experiment at Princeton University show [Erickson00] that at pressures less than one amagat of buffer gas, the main spin-relaxation in alkali-alkali-metal comes from the spin-axis interaction in triplet dimer molecules. The key observation is the magnetic-resonances in spin-relaxation as predicted by the spin-axis interaction. We wanted to emphasize that single values of λ and σ_c accurately describe all the magnetic decoupling spin-relaxation curves from 10 torr to 690 torr of N_2 buffer gas. At buffer gas pressures of an amagat or more we still do not understand alkali-alkali spin-relaxation. The relaxation rate up to about 20 amagat of buffer gas still shows the same decoupling curve with the same magnetic field decoupling width.

Chapter 3

^{129}Xe-Xe Molecular Spin-Relaxation

3.1 Introduction

It is generally agreed that the interaction that produces spin-relaxation in both gaseous and liquid ^{129}Xe is the nuclear spin-rotation interaction [Happer84] [Hunt63] [Fitzgerald99] [Torrey63]

$$V_{sr} = c_K(R)\mathbf{K} \cdot \mathbf{N}, \tag{3.1}$$

where $\mathbf{K}$ is the nuclear spin of the ^{129}Xe atom and $\mathbf{N}$ is the rotational angular momentum of the ^{129}Xe-Xe pair. The interaction is due to the coupling between the atom's nuclear magnetic moment and the magnetic field arising from the rotation of the ^{129}Xe-Xe pair. The spin-rotation interaction is also believed to be responsible for the spin-relaxation of solid ^{129}Xe at temperature $50 \leq T \leq 120K$, where it gives rise to Raman scattering of phonons [Fitzgerald99]. Furthermore, it is also responsible for the chemical shift in both solid [Raftery92] and gaseous ^{129}Xe [Jameson73].

There have been measurements of the gaseous ^{129}Xe-Xe spin-relaxation cross section over the years and they all seem to agree fairly well [Moudrakovski01] [Brinkmann62]

[Hunt63]. However, these measurements were done at high gas pressures, where the primary spin-relaxation occurs through the binary collisions between ^{129}Xe-Xe. On the other hand, most practical applications require moderate or low gas pressures (less than 14 amagats) where van der Waals molecules can exist.

In this part of the thesis, we identified and observed a new gas phase spin-relaxation mechanism that occurs in bound ^{129}Xe-Xe van de Waals molecules. The interaction responsible is the same nuclear spin-rotation interaction. For a fixed gas composition, the spin-relaxation rate turns out to be independent of gas density. Hence, it is difficult to differentiate the relaxation rate due to the van der Waals molecules from the relaxation rate due to the wall. To observe the ^{129}Xe-Xe van der Waals molecules' spin-relaxation we measured the spin-relaxation rate as a function of gas composition. Since the wall spin-relaxation does not depend on gas composition and density, we were able to isolate this new gas phase ^{129}Xe nuclear spin-relaxation.

We measured the relaxation rate due to ^{129}Xe-Xe van der Waals molecules to be $(6.7 \times 10^{-5} s^{-1})$ or 4.1 hours for pure ^{129}Xe gas. At one amagat of ^{129}Xe the spin-relaxation due to binary collisions is 56 hours. Thus, the relaxation rate due to van der Waals molecules is more than an order of magnitude faster than the well-known spin-relaxation rate due to the binary collisions. This has very important implications for magnetic resonance imaging of human organs, where one would like to be able to store the polarized ^{129}Xe as long as possible before administering it to patients.

In section 3.2 I present the ^{129}Xe-Xe potential that we used to calculate the chemical equilibrium coefficient for the ^{129}Xe-Xe van der Waals molecules. Following this, the theory behind ^{129}Xe-Xe van der Waals spin-relaxation due to spin-rotation coupling is given in section 3.3. Section 3.4 is a description of the experimental procedure. Finally, I present the data and discussion in section 3.5.

3.2 ^{129}Xe-Xe Potential

The Hamiltonian describing the evolution of a ^{129}Xe nucleus in a ^{129}Xe-Xe pair is [Torrey63]

$$H = V(R) + \hbar \mathbf{K} \cdot \mathbf{\Omega} + c_K(R) \mathbf{K} \cdot \mathbf{N}, \tag{3.2}$$

where the first term is the spin-independent ^{129}Xe-Xe interaction potential. The second term is the Zeeman coupling between the nucleus and the external magnetic field $\mathbf{B} = K\mathbf{\Omega}/\mu_K$, where μ_K is the nuclear magnetic moment. $\mathbf{K}$ is the nuclear spin which is equal 1/2. The last term in the Hamiltonian is the spin-rotation coupling between the nuclear spin and the rotational angular momentum, $\mathbf{N}$, of the pair. $c_K(R)$ is the spin-rotational coupling energy.

The spin-independent ^{129}Xe-Xe interaction potential is taken from Dham et al. [Dham90]. It is plotted in figure 3.1. The potential $V(R)$ has a depth of 24.4 meV at $R_o = 4.36$A. The explicit expression for the potential is

$$V(R) = A\exp(-\alpha R + \beta R^2) - (C_6 R^{-6} + C_8 R^{-8} + C_{10} R^{-10}) F(R); \tag{3.3}$$

where

$$F(R) = \exp\Big[-(DR_m R^{-1} - 1)^2\Big], \qquad R < DR_m; \tag{3.4}$$

$$= 1, \qquad R \geq DR_m. \tag{3.5}$$

The parameters are:

$$R_m(a_0) = 8.249788, \tag{3.6}$$

$$C_6(\text{hartree } a_0^6) = 283.900, \tag{3.7}$$

$$C_8(\text{hartree } a_0^8) = 11214.00, \tag{3.8}$$

$$C_{10}(\text{hartree } a_0^{10}) = 619600.0, \tag{3.9}$$

$$\alpha(a_0^{-1}) = 0.912700, \tag{3.10}$$

$$\beta(a_0^{-2}) = -0.049061, \tag{3.11}$$

$$A(\text{hartree}) = 48.72733, \tag{3.12}$$

$$D = 1.114. \tag{3.13}$$

To make any reasonable spin-relaxation rate calculation we need to know the fraction of ^{129}Xe atoms that are in the molecules. The procedure is the same as in calculating triplet molecules in Cesium vapor. The relative motion of the pair of ^{129}Xe atoms is reduced to the motion of the relative particle of reduced mass [Bouchiat69]

$$\mu = \frac{m_1 m_2}{(m_1 + m_2)} \tag{3.14}$$

in the effective potential

$$U_{eff} = V(R) + \frac{N(N+1)\hbar^2}{2\mu R^2}, \tag{3.15}$$

where $\hbar N$ is the rotational angular momentum of the pair. We used the Fourier grid method (Appendix A) [Marston89] [Balint-Kurti92] [Borisov01] to find all the ro-vibrational wave functions $|i\rangle$ and energies E_i. Figure 3.2 shows all the eigen-energies plotted as a function of rotational angular momentum, N. From the eigen-energies we calculated the chemical equilibrium coefficient defined as [Kadlecek01]

$$\kappa_{chem} = \frac{1}{2}\left(\frac{h^2}{2\pi\mu kT}\right)^{3/2} \sum_i (2N_i + 1) e^{-E_i/kT}. \tag{3.16}$$

The resulting chemical equilibrium coefficient, κ_{chem}, at temperature of 297 K is

$$\kappa_{\text{chem}} = 230 \ \ \text{A}^3 \tag{3.17}$$

3.3 ^{129}Xe-Xe van der Waals Spin-Relaxation

Molecular spin-relaxations in van der Waals molecules were first discussed and derived in detail by Bouchiat and coworkers [Bouchiat69] [Kadlecek01]. Therefore, the details

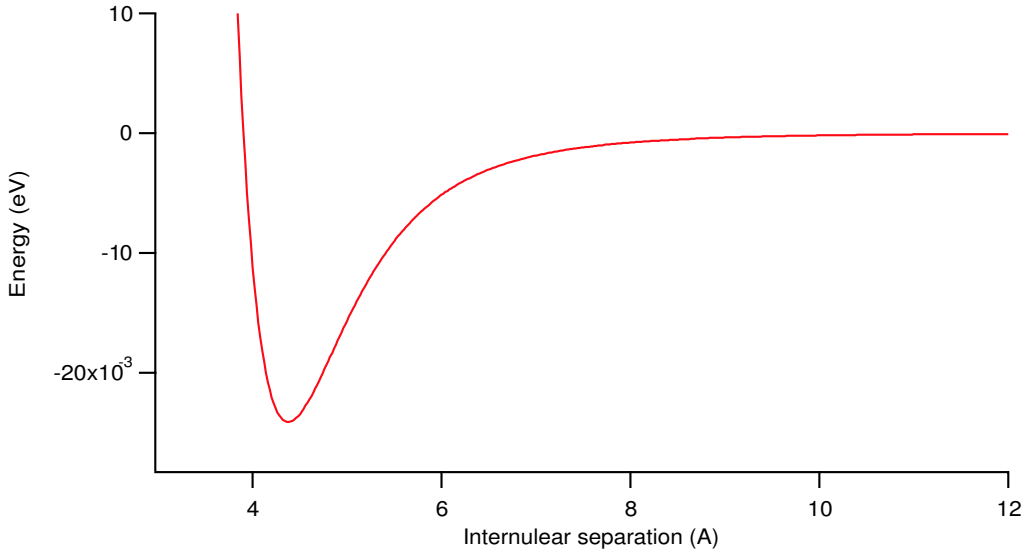

Figure 3.1: Xenon-Xenon Hartree-Fock-dispersion potential from Dham et al. The potential has a depth of 24.4 meV at $R_o = 4.36$A

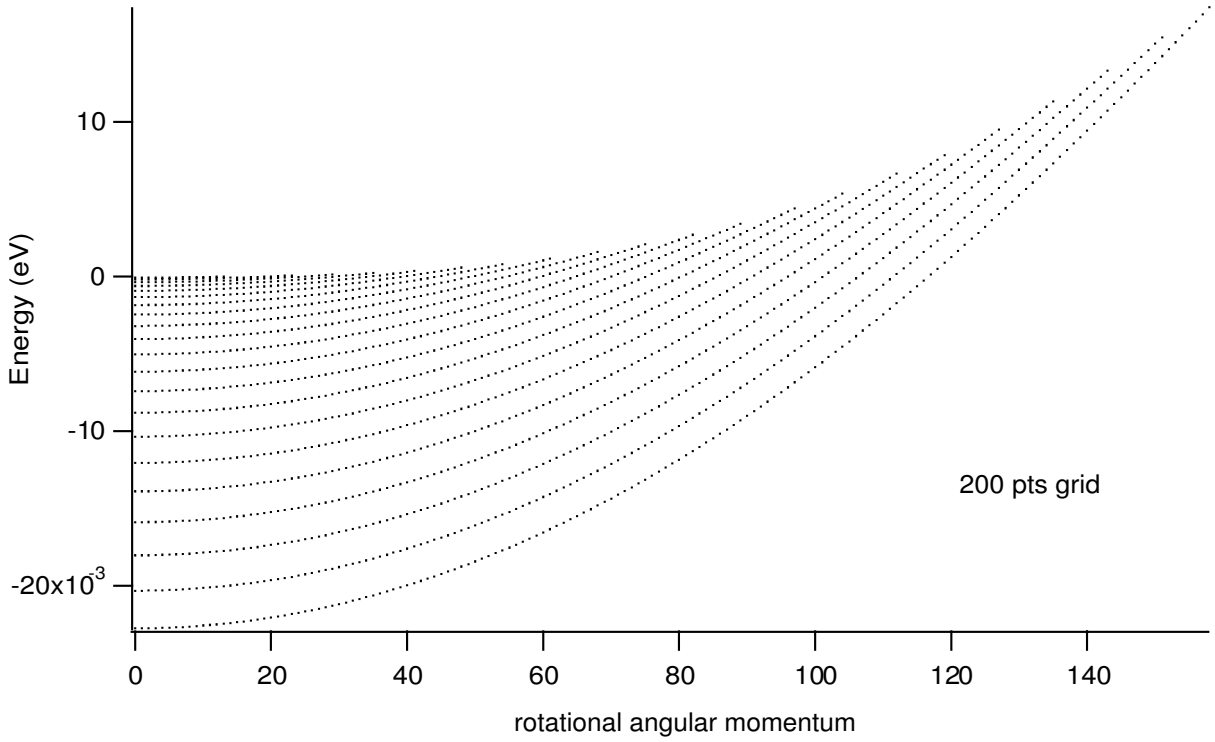

Figure 3.2: All eigen-energies as a function of rotational angular momentum.

of the derivation will be left out in this thesis and only the results will be summarized here.

The spin-relaxation rate due to the ^{129}Xe-Xe van der Waals molecules is the rate, $1/T_F$, at which the ^{129}Xe atoms are formed into molecules times the fraction, $W(\tau_B)$, of polarization lost during its molecular lifetime, τ_B. Here we assumed that each collision with a third body breaks the molecules apart. In other words, the coherence time of the molecules is the same as the molecular lifetime. By detailed balance, the molecular formation rate is [Happer84][Kadlecek01]

$$\frac{1}{T_F} = \frac{2\kappa_{chem}[Xe]}{\tau_B} \tag{3.18}$$

With these assumptions the ^{129}Xe nuclear spin-relaxation rate due to the van der Waals molecules is [Bouchiat69][Walker02][Kadlecek01]

$$\begin{aligned} \Gamma_{vdW} &= \frac{W}{T_F} = \frac{1}{T_F}\frac{2\langle c_K^2 N^2\rangle \tau_B^2}{3\hbar^2(1+\Omega^2\tau_B^2)} \\ &= \frac{4\kappa_{chem}[Xe]\langle c_K^2 N^2\rangle \tau_B}{3\hbar^2(1+\Omega^2\tau_B^2)}. \end{aligned} \tag{3.19}$$

In the typical spin-exchange optical pumping experiment the static applied magnetic field is less than 100 gauss. Thus, the magnetic field dependent part of the relaxation rate can be ignored and the resulting equation is

$$\Gamma_{vdW} = \frac{4\kappa_{chem}}{3\hbar^2}[Xe]\langle c_K^2 N^2\rangle \tau_B. \tag{3.20}$$

From the above equation, for a fixed pure ^{129}Xe gas, Γ_{vdW} is independent of Xenon density since $\tau_B \propto 1/[Xe]$. In the general case of two gases (or more), the molecular lifetime, τ_B, [Happer84] [Kadlecek00] [Kadlecek01] can parameterize it as

$$\frac{1}{\tau_B} = \kappa_B[B] + \kappa_{Xe}[Xe], \tag{3.21}$$

where κ_B and κ_{Xe} are the breakup rate coefficients due to buffer gas and ^{129}Xe, respectively. [B] is the buffer gas density. Substituting the above equation into Γ_{vdW}

$$\begin{aligned}\Gamma_{vdW} &= \frac{4\kappa_{chem}}{3\hbar^2}\frac{\langle c_K^2 N^2\rangle}{\kappa_{Xe}(1+r[B]/[Xe])} \\ &= \frac{\Gamma_{vdW}^{Xe}}{(1+r[B]/[Xe])},\end{aligned} \tag{3.22}$$

where $r = \kappa_B/\kappa_{Xe}$ and

$$\Gamma_{vdW}^{Xe} = \frac{4\kappa_{chem}\langle c_K^2 N^2\rangle}{3\hbar^2\kappa_{Xe}} \tag{3.23}$$

is the ^{129}Xe-Xe molecular spin-relaxation rate in pure ^{129}Xe gas.

The above equations tell us that for a fixed ratio of buffer gas to Xenon, the relaxation rate due to van der Waals molecules is inseparable from wall-relaxation. Also, the above equations tell us explicitly how to measure the relaxation rate due to the van der Waals molecules. By varying the ratio of buffer gas density to ^{129}Xe gas density, the relaxation due to van der Waals molecules can be varied in a way that is different from the wall-relaxation.

3.4 Experimental Design

The measurement of the spin-relaxation rate of ^{129}Xe as a function of gas composition is as follows. A prototype commercial continuous flow ^{129}Xe polarizer [Driehuys96] from Nycomed Amersham is used. The spin-exchange optical pumping cell is pumped by a 50 W fiber-coupled diode array bar. The continously-flowing polarized ^{129}Xe is frozen using liquid N_2 at a glass cold-finger in a 2000 gauss magnetic field. After collecting for about 10-20 minutes, corresponding to roughly about 100 cm^3 of gaseous polarized ^{129}Xe, the cold-finger is thawed and the gaseous ^{129}Xe is collected with a 7.5 cm diameter uncoated quartz cell. Typical ^{129}Xe polarization ranges from 10-30%. It

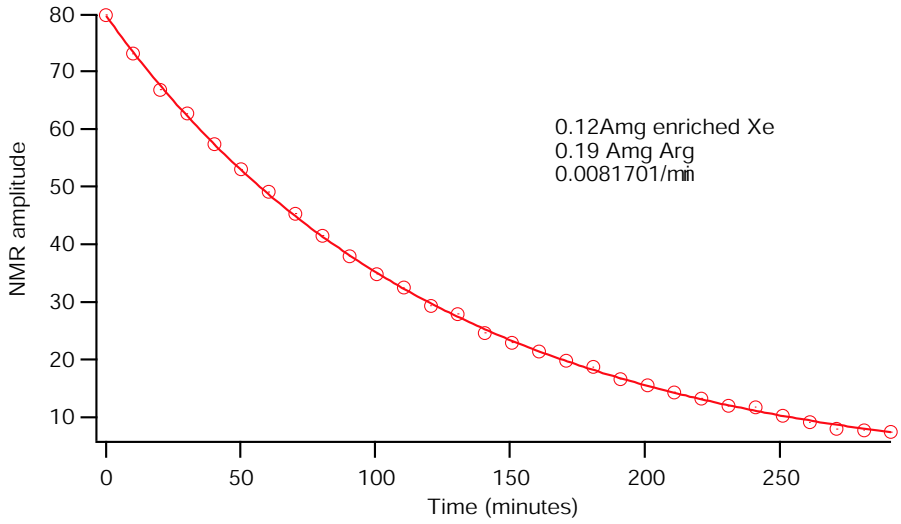

Figure 3.3: A sample exponential decay and the fit of Xe polarization as a function of time. Here the gas composition is 0.19 amagat of Argon and 0.12 amagat of Xe.

is then mixed with the desired buffer gas (^{4}He, Ar, N_2). The ^{129}Xe pressure is kept as low as possible to avoid spin-relaxation due to binary collisions. Most of the time the ^{129}Xe density is held at about 0.15 amagat. We use isotopically enriched ^{129}Xe with 82% ^{129}Xe composition to enhance the NMR signal.

After collecting the polarized gas, the cell is then placed on a low field magnetic resonance detection coil. The holding field is 20.4 gauss. The ^{129}Xe polarization as a function of time is then detected by sending a series of small angle tip to a surface mounted coil every 10 minutes. The free-induction decay (FID) signal is detected using the same coil. The loss due to FID pulses is determined experimentally to be negligible. The spin-relaxation rate is obtained by fitting the FID amplitudes as a function of time. The exponential decay time constant gives the spin-relaxation rate. Figure 3.3 shows a typical exponential decay of ^{129}Xe polarization as a function of time. Also shown is the exponential fit of the raw data.

3.5 Data and Discussion

The total ^{129}Xe relaxation rate in the cell comes from three parts: wall relaxation, binary collisions and ^{129}Xe-Xe van der Waals molecules. The binary collisions contribute [Moudrakovski01] [Brinkmann62] [Hunt63]

$$\Gamma_b = 5.0 \times 10^{-6} s^{-1} \quad \frac{[\mathrm{Xe}]}{1 \text{ amagat}} \tag{3.24}$$

to the relaxation rate. Since in our experiment the typical ^{129}Xe density is about 0.1 -0.3 amagat we will ignore the binary contribution. Therefore, we fit our data to the functional form

$$\Gamma = \Gamma_w + \frac{\Gamma_{vdW}^{Xe}}{(1 + r[B]/[Xe])}, \tag{3.25}$$

where Γ_w is the wall relaxation rate. Figures (3.4, 3.5, 3.6) show the ^{129}Xe relaxation rates as a function of buffer gas to ^{129}Xe density. Also shown is the fit of the data to equation 3.25. The fit results for the three buffer gases are shown in Table I. The results for r suggest that ^{4}He has the smallest breakup rate coefficient. Ar is twice as efficient as ^{4}He. N_2 has about the same breakup rate coefficient as ^{129}Xe. Notice that Γ_w is almost the same for all the buffer gases.

The mean weighted molecular spin-relaxation rate for pure ^{129}Xe-Xe is

$$\Gamma_{vdW}^{Xe} = 6.72 \ \pm \ 0.1 \times 10^{-5} \ s^{-1}. \tag{3.26}$$

This corresponds to a relaxation rate of 4.1 hours. This is very surprising. Compared to the binary collision rate, it is more than an order of magnitude larger.

From Γ_{vdW}^{Xe} we can deduce the value of ^{129}Xe breakup rate coefficient, κ_{Xe}. First we need to calculate $\langle c_K^2 N^2 \rangle$ which is a weighted sum over all the eigen-states:

$$\langle c_K^2 N^2 \rangle = \frac{1}{Z} \sum_i N_i^2 (2N_i + 1) \langle i | c_K(R) | i \rangle^2 e^{-E_i/kT}, \tag{3.27}$$

Buffer gas	Γ_{vdW}^{Xe} $(10^{-5}s^{-1})$	r	$\Gamma_w(10^{-5}s^{-1})$
^{4}He	8.23 ± 0.6	0.25 ± 0.8	9.05 ± 0.6
Ar	6.81 ± 0.2	0.49 ± 0.06	9.5 ± 0.2
N_2	6.63 ± 0.1	1.05 ± 0.08	9.9 ± 0.1

Table 3.1: ^{129}Xe-Xe molecular spin-relaxation rates Γ_{vdW} and the relative breakup rate coefficient r deduced from ^{129}Xe spin-relaxation in quartz cell with wall-relaxation rate Γ_w.

where Z is the partition function

$$Z = \sum_i (2N_i + 1)e^{-E_i/kT}. \tag{3.28}$$

$c_K(R)$ is related through the chemical shift as [Torrey63]

$$\frac{c_K(R)}{h} = \frac{\mu_K}{K\mu_B}\frac{3\hbar}{4\pi R^2}\sigma_1(R) = c_K(R_0)\Big(\frac{R_0}{R}\Big)^8, \tag{3.29}$$

where μ_K is the magnetic moment, μ_B is the Bohr magneton and the chemical shift, $\sigma_1(R)$, is assumed to be of the form [Jameson92]

$$\sigma_1(R) = \sigma_1(R_0)\Big(\frac{R_0}{R}\Big)^6. \tag{3.30}$$

The ^{129}Xe-Xe chemical shift at room temperature is measured [Jameson75] to be $\sigma_1 = -553$ ppb/amagat. Knowing this and the potential, we can estimate $\sigma_1(R_0)$ through [Jameson92]

$$\sigma_1(T) = \int dR\, 4\pi R^2 \sigma_1(R)\, e^{-V(R)/kT} = -553\ \ \frac{\text{ppb}}{\text{amagat}}. \tag{3.31}$$

This is only true if

$$\sigma_1(R_0) = 2.3 \times 10^{-5}. \tag{3.32}$$

Using this value of $\sigma_1(R_0)$, we obtain

$$c_K(R_0) = -24\text{Hz}. \tag{3.33}$$

This value is very comforting since $c_K(R_0)$ was deduced by Fitzgerald et al. [Fitzgerald99] in solid ^{129}Xe experiment to be about -27 Hz. Putting all of these together and evaluating the matrix element, we find

$$\sqrt{\langle c_K^2 N^2 \rangle} = h \times 820\text{Hz}. \tag{3.34}$$

Thus, using our measured value for Γ_{vdW}^{Xe} we deduce the breakup rate coefficient to be

$$\kappa_{Xe} = 1.2 \times 10^{-10}\text{cm}^3/\text{s}. \tag{3.35}$$

This corresponds to breakup cross section of

$$\sigma_{Xe} = 4.4 \times 10^{-15}\text{cm}^2. \tag{3.36}$$

We can also check the ^{129}Xe relaxation rate by fixing the ratio of the buffer gas density to ^{129}Xe density fixed and varying the total pressure. Figure 3.7 shows the relaxation rate with the ratio fixed at 1.75. The relaxation rate is independent of the total gas pressures as expected. Furthermore, as a consistency check, we estimate $c_K(R)$ by scaling it to the recently remeasured binary spin-relaxation rate [Moudrakovski01]. An energy dependent binary spin-relaxation cross section is defined as [Walker89]

$$\sigma(E) = \frac{8\pi\mu^2}{3\hbar^4} \int_0^\infty b^3 \, db \left| \int_{r_0}^\infty dR \frac{c_K(R)}{\sqrt{1 - b^2/R^2 - V(R)/E}} \right|^2, \tag{3.37}$$

where r_0 is the classical turning point or when [$(1 - b^2/r_0^2 - V(r_0)/E = 0)$] and b is the impact parameter. By averaging over all velocities we get

$$\sigma(T) = \frac{1}{(kT)^2} \int_0^\infty dE \, \sigma(E) \, E \, e^{-E/kT}. \tag{3.38}$$

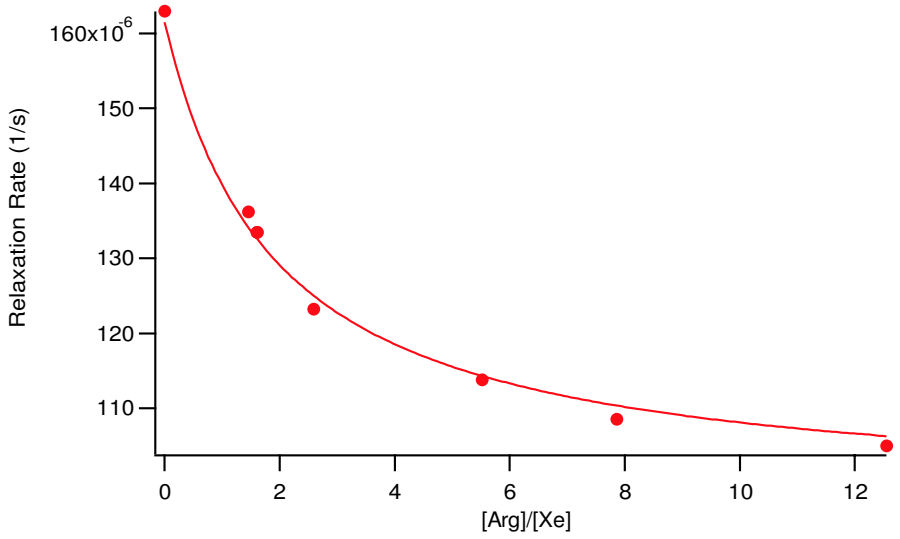

Figure 3.4: The relaxation rate of Xe as a function of the ratio of argon to xenon pressure. Also shown is the fit from equation 3.25.

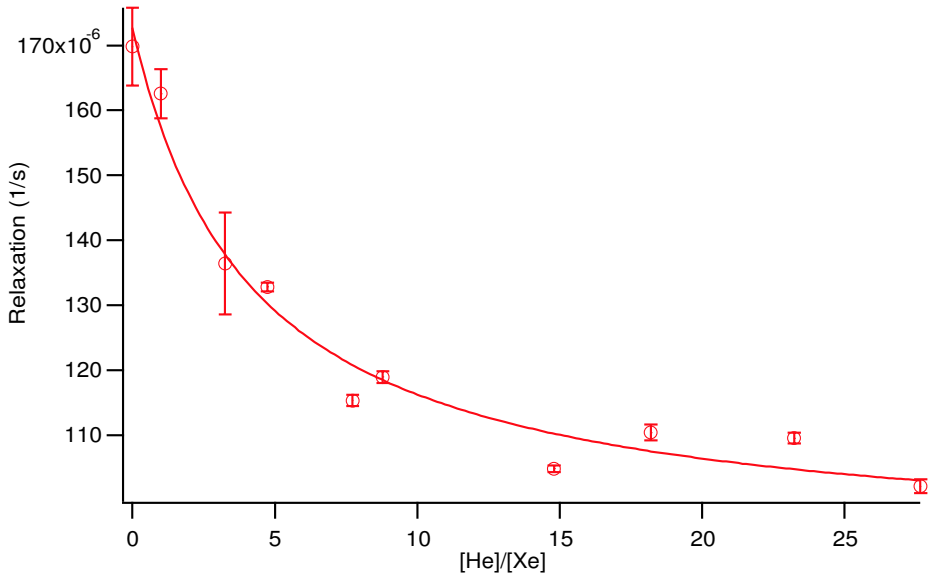

Figure 3.5: The relaxation rate of Xe as a function of the ratio of Helium buffer gas to Xe. Also shown is the fit from equation 3.25.

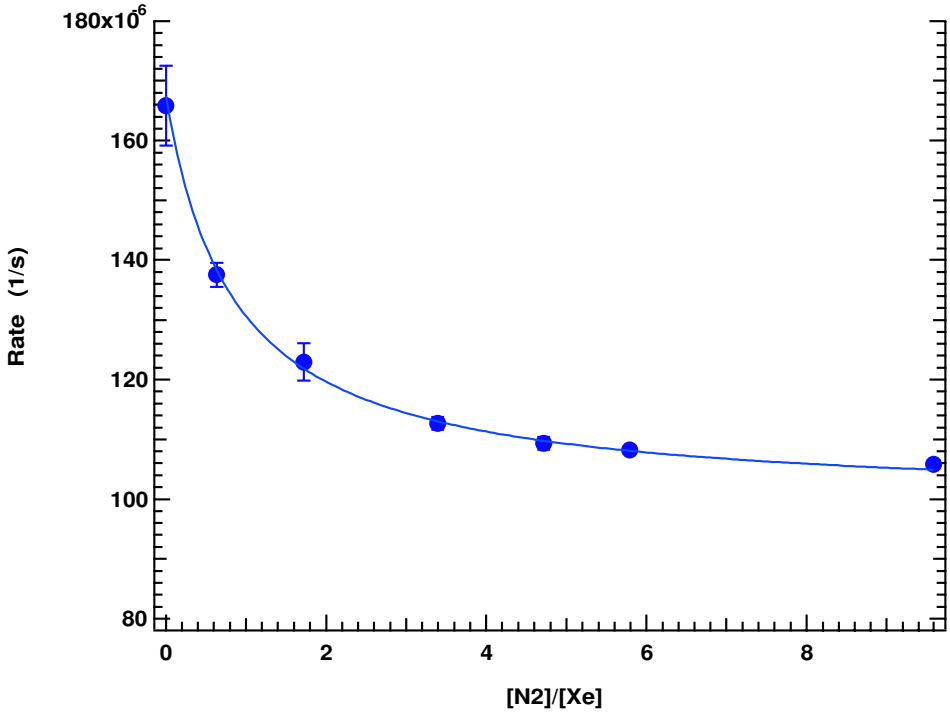

Figure 3.6: The relaxation rate of Xe as a function of the ratio of Nitrogen buffer gas to Xe pressure.

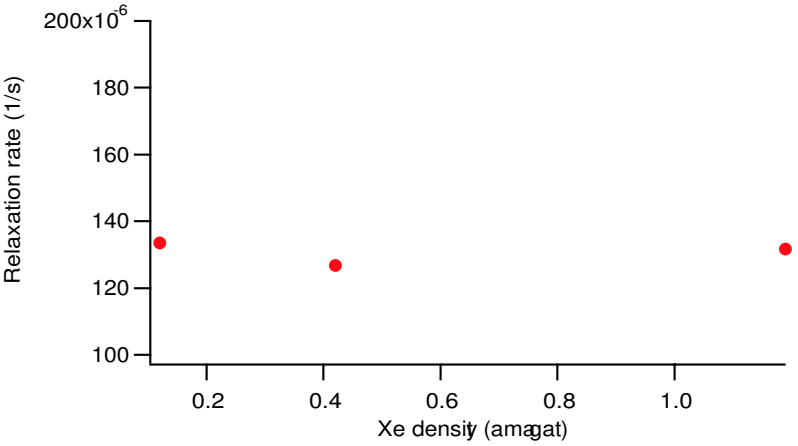

Figure 3.7: Graph showing Xe relaxation as a function of Xe pressure (Ar buffer gas). The ratio was kept at 1.75

At 25^{o}C the measured binary spin-relaxation cross section is $5.9 \times 10^{-30}\text{cm}^2$, which implies that

$$\mid c_K(R) \mid = h \times 41\text{Hz} \times \left(\frac{R_0}{R}\right)^8, \tag{3.39}$$

which is a fair agreement with the estimate using the frequency shift.

In addition to ^{129}Xe-Xe van der Waals molecules, there is also a possible relaxation from Xe-Ar, Xe-N_2 and Xe-He molecules which we have not taken into account. The binding energy for Xe-Ar and Xe-N_2 is about 16.2 meV [Aziz83] and 8.4 meV [Dios97], respectively. This is smaller than the ^{129}Xe-Xe binding energy but not negligible. The spin-relaxation rate by these molecules will have the exact form as ^{129}Xe-Xe,

$$\Gamma^{'}_{vdW} = \frac{2\kappa^{'}[B]\langle c^{'2}_K N^2\rangle \tau^{'}_B}{3\hbar^2(1+\Omega^2\tau^{'}_B)} \tag{3.40}$$

From the frequency shift [Jameson92] and the potential curve we estimate

$$\kappa^{'} = 185 \quad \text{A}^3 \tag{3.41}$$

$$\sqrt{\langle c^{'2}_K N^2\rangle} = h \times 765 \quad \text{Hz} \tag{3.42}$$

for the Xe-Ar pairs. Assuming that these molecules are more readily broken up implies that

$$\Gamma^{'}_{vdW}(\text{max}) < 0.35\ \Gamma^{Xe}_{vdW}. \tag{3.43}$$

This seems, however, to be unlikely since the deduced Γ_w are the same for all the buffer gases. Considering that the binding energy for Xe-He is only about 2.5 meV [Aziz89] [Aziz90], the spin-relaxation rate due to van de Waals molecules in Xe-He would be very small. Thus, it is unlikely that Xe-Ar and Xe-N_2 van der Waals molecules play a significant role in the spin-relaxation.

Chapter 4

External-Cavity Diode-Laser-Array Bar

4.1 Introduction

The steady state polarization of the noble gas is

$$P = \frac{R_p}{(R_p + \Gamma)} \frac{\kappa[Rb]}{(\kappa[Rb] + \Gamma_w)}, \tag{4.1}$$

where R_p is the alkali-metal pumping rate, Γ is the alkali-metal spin-relaxation rate, κ is the alkali-metal-noble gas spin-exchange rate coefficient, and Γ_w is the noble gas wall-relaxation rate. To achieve high noble gas polarization, as shown in equation 4.1, it is crucial to have a high pumping rate so that $R_p >> \Gamma$. This means that the laser plays a key role in maximizing P.

The lasers of choice for spin-exchange optical pumping are the diode array bars (DAB) with power from 15 watts to hundreds of watts. These are relatively inexpensive and easy to use compared to dye or Ti:Sapphire lasers. However, the DAB's linewidths are typically about 1000GHz and much bigger than the absorption linewidth of the Rb

atoms (20 GHz/bar) [Romalis97]. Conventionally, high ^{3}He or ^{4}He pressure (3 to 10 bar) is used to broaden the Rb absorption linewidth, but such high a pressure is not always desirable. For mechanical stability cells tend to be round with small diameters and thus further complicates the pumping of Rb atoms. Many applications including neutron spin filters require large cells with nice geometries.

The highest ^{3}He polarization attained using diode array bar reported in the literature is about 55% [Rich02]. In ^{129}Xe the typical observed polarization is about 10 to 15% [Driehuys96]. Thus, for example, the resolution of the magnetic resonance of the lungs using ^{129}Xe is still very much limited by this low ^{129}Xe polarization. Experiments which rely on high ^{3}He polarization could also greatly benefit from higher than 55% ^{3}He polarization. For example, one of the experiments at Los Alamos plans to measure the weak nucleon-nucleon coupling constant, H_π, by measuring the gamma ray emission directional parity-violating asymmetry (A_γ) in the $\overrightarrow{n} + p \rightarrow d + \gamma$ reaction. Here ^{3}He is used as a polarizer. The goal of the experiment is to measure A_γ with an uncertainty of $< 5 \times 10^{-9}$. Assuming the current value of 55% obtained for the ^{3}He polarization, this requires 500 days of run time on the accelerator. A ^{3}He polarization of 74% reduces the run time to 290 days.

In this part of the thesis I present the external cavity diode array bar that was invented by our group [Chann00]to improve on this state of affairs. We have obtained a linewidth as low as 47 GHz with only a loss of about 33% in output power which gives a much greater amount of light for the atoms to absorb. Therefore, pressure broadening is not as necessary, so efficient optical pumping of Rb atoms can be performed at a pressure of one bar or lower. In addition, it has the added benefit of allowing longer lifetimes for the cells, since the dipole-dipole interactions place the fundamental limit in bulk ^{3}He relaxation at $(807/P)$ hours, where P is the pressure of ^{3}He in units of bars at room temperature [Newbury93]. Since pressure broadening is not required cells can be

made with large diameters which would meet the demands of experiments such as the proposed $\overline{n} + p \rightarrow d + \gamma$ at LANSCE. Furthermore, work described later in this thesis suggests that the only way to achieve high ^{3}He polarization is using a large volume cell. This is due to an unknown mechanism that produces an excess of ^{3}He relaxation [Chann02a][Chann02b].

Section 4.2 describes in detail the external cavity diode array bar. Section 4.3 analyzes its performance.

4.2 External Cavity Diode Array Bar

A diode laser array bar (DLAB) consists of a large number of broad area lasers (BALS) or emitters, typically anywhere from 10 to 49 emitters, in a length of 1 cm. The dimension of each emitter is typically 1μm by 100μm with a separation of about 500μm. Light emitted perpendicular to the array (fast axis) has a typical diffraction-limited divergence of 40 degrees, while light emitted along the laser (slow axis) has a divergence of 10 degrees. Frequency narrowing a DLAB is difficult because of the large number of emitters and the large divergence of the emitted light. To make matters worse, most DLABs are not straight. There is a small curvature, or better known as "smile", usually about 3 μm to 10 μm. A picture of the "smiles" is shown in figure 4.1.

In an external cavity low power single mode diode laser [Wieman91] [MacAdam92], light in a Littrow-mounted cavity is collimated by a single fast aspheric lens and retro-reflected off a grating. The first order retro-reflected light is used as feedback to set the laser frequency and reduce its linewidth. The zeroth diffraction order is taken as the laser output. This simple cavity does not work for DLAB due to its large number of emitters and large divergence angles, but we found that a slightly more complex version is effective.

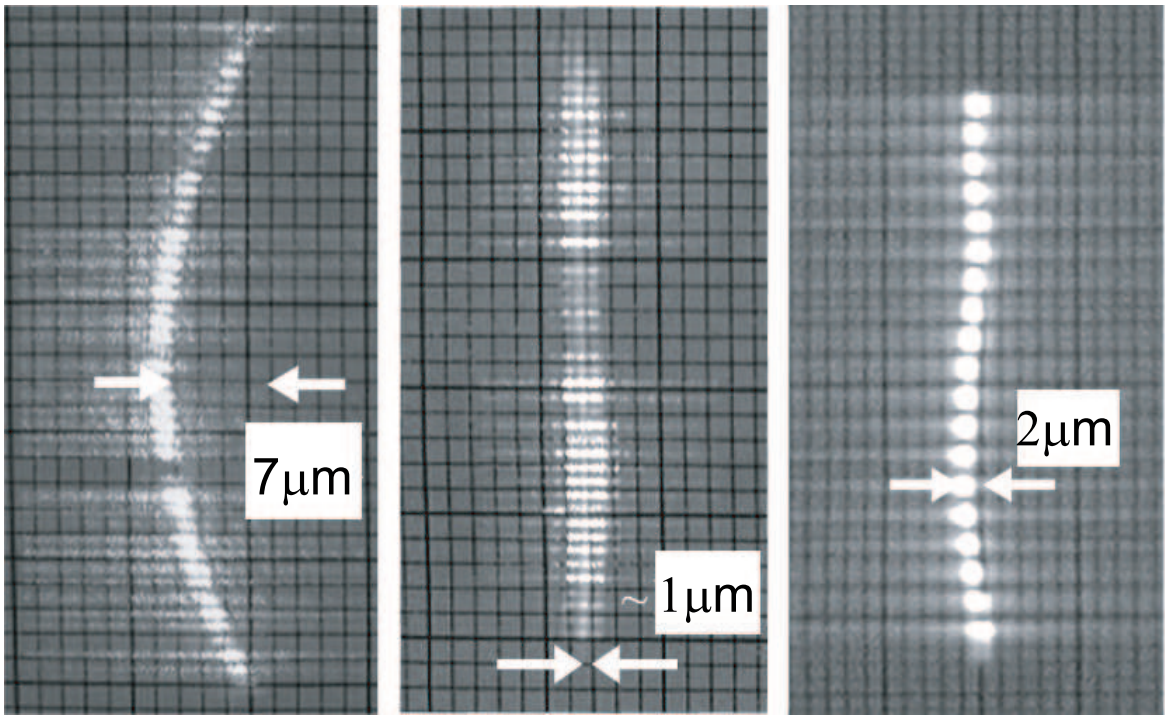

Figure 4.1: Picture showing the images of 3 different diode array bars. Notice the "smile" or curvature of the laser. The left image is a picture of a 7 μm "smile" 46-element CEO laser. The middle is an image of a 1 μm "smile" 46-element CEO laser. The right is an image of a 19-element Coherent laser with a 2 μm "smile".

The cavity that we developed is shown in figure 4.2. We use a fast cylindrical microlens to collimate the fast axis. This is followed by an afocal telescope which images each emitter onto the Littrow-mounted grating. Typical magnification of the telescope is about 4 to 5. The frequency-selected first order from the grating of each emitter is reimaged back onto itself.

For light striking the grating with direction $\hat{z}\cos\alpha\cos\phi + \hat{y}\sin\alpha + \hat{x}\sin\alpha\sin\phi$ with respect to the optical axis, the grating equation for a Littrow-mounted cavity reduces to [Chann00]

$$\lambda = 2d\sin(\theta - \phi)\cos\alpha \tag{4.2}$$

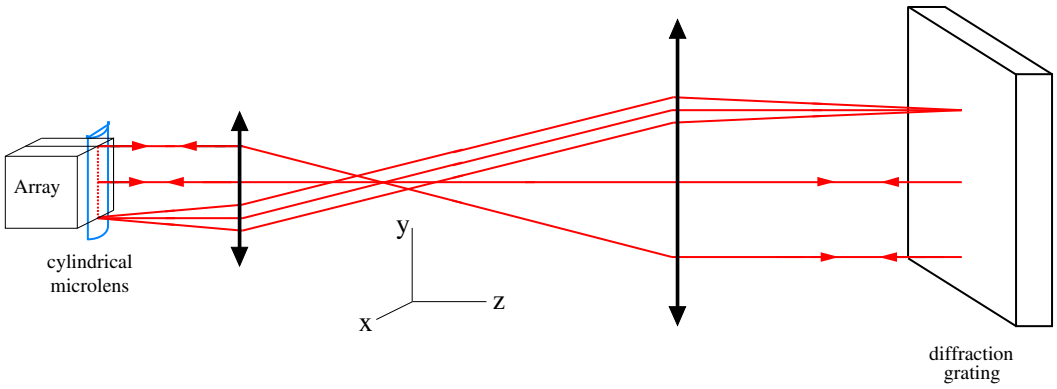

Figure 4.2: Diagram showing selected rays of the external cavity diode array bar cavity. The two vertical arrow-lines are the two spherical lenses of the telescope.

or

$$\delta\lambda/\lambda_0 \approx -\alpha^2/2 - \phi\cot\theta \tag{4.3}$$

where $\lambda_0 = 2d\sin\theta$. θ is the angle between the optical axis and the grating normal, α is the divergence of the light along the slow-axis, and ϕ is the angle due to the smile. $\delta\lambda = \lambda - \lambda_0$ and the angles α and ϕ are assumed to be small. Thus, from equation 4.3 spreads in α and ϕ both result in broadening of the laser spectrum. Also, the linewidth has a $\cot\theta$ dependence. From figure 4.2, the telescope reduces the angular spread, α_0, from the laser by a factor inversely proportional to the magnification of the telescope or $\alpha = \alpha_0/M$, where M is the magnification of the telescope. Thus, from equation 4.3 this reduces the broadening of the laser spectrum due to the slow axis divergence by the square of the magnification. The telescope also reduces the spread of the angle of curvature by a factor $\phi = x/Mf_c$, where x is the curvature or "smile" of the laser and f_c is the focal length of the micro-lens. The resulting linewidth due to the "smile" is

$$\frac{d\lambda}{\lambda} = \frac{x\cot\theta}{Mf_c}. \tag{4.4}$$

So for the cavity to work best it is desirable to have a low "smile" x, large diffraction angle θ, large telescope magnification M, and long micro-lens focal length f_c.

4.3 Results

We began by testing the narrowing of a 20W 801-nm laser that is 1 cm-long with 46-emitters from Cutting Edge Electronics [CEO]. The measured unnarrowed linewidth was 670Ghz. The array was preselected by the manufacturer to have a "smile" of about 1μm, which we verified by direct measurement. We used a f_c=0.73 mm cylindrical micro lens, a telescope with a magnification of four, and a 2400 lines/mm holographic grating. The output zeroth order beam was at about 72^o. The measured output power was 12.2W out of 18W total unnarrowed output power from the laser. We measured the linewidth with a home-made parallel-plate Fabry-Perot to be about 60 GHz. With some adjustments we have achieved a best linewidth of 47 GHz as is shown in figure 5.3. Thus a reduction of a factor of 15 in the linewidth was obtained with only 33% loss in power. Figure 4.4 shows the tuning range and spectral power of the external cavity diode array bar, which is suitable for spin-exchange optical pumping where precise frequency is required. Using a similar laser from Coherent Inc. [Cohr] with a "smile" of about 2μm we obtained 14W of power out of 22W free-running. The spectral width measured was about 125 GHz at 795 nm.

We now compare the performance between the narrowed light and the unnarrowed light. Using a 14W narrowed Coherent external cavity diode array bar with about 125GHz linewidth, the measured Rb polarization is 100% at a Rb density as high as 3.5×10^{14} cm^{-3} in a cylindrical cell with diameter 4.7 cm and length 4.9 cm. The ^{3}He polarization is as high as 73% in the same cell (the cold-lifetime of the cell is 240 hours). This is the highest reported ^{3}He polarization using the diode array. A plot

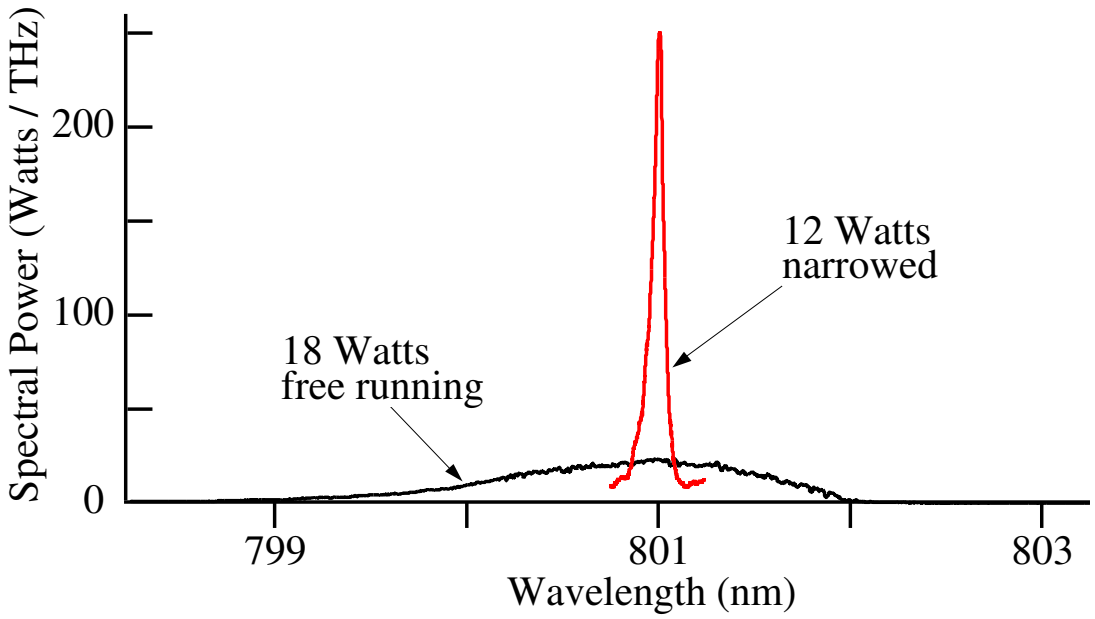

Figure 4.3: Graph comparing the spectral density of a free-running diode array bar and an external cavity diode array bar. The spectral density of the narrowed array is about 10 times greater than the free-running power density.

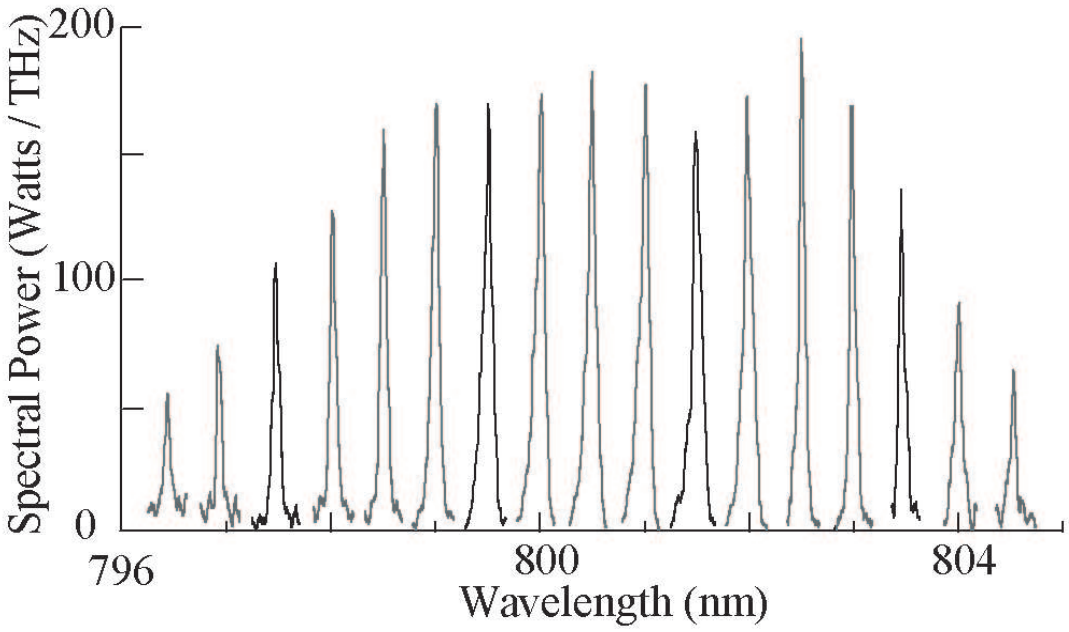

Figure 4.4: Tuning range and spectral power density of the external cavity diode array bar.

comparing the advantages of using the external cavity diode array for spin-exchange optical pumping is shown in figure 4.5. The graph plots the ^{3}He polarization using a 14W Coherent external cavity diode array bar as compared to 42W of unnarrowed light (22W from the Coherent diode array and 20W from the Spectra Physics diode array). The spectral width of the unnarrowed diode array is about 1500 GHz for the Spectra Physics diode array and about 750 GHz for the Coherent diode array.

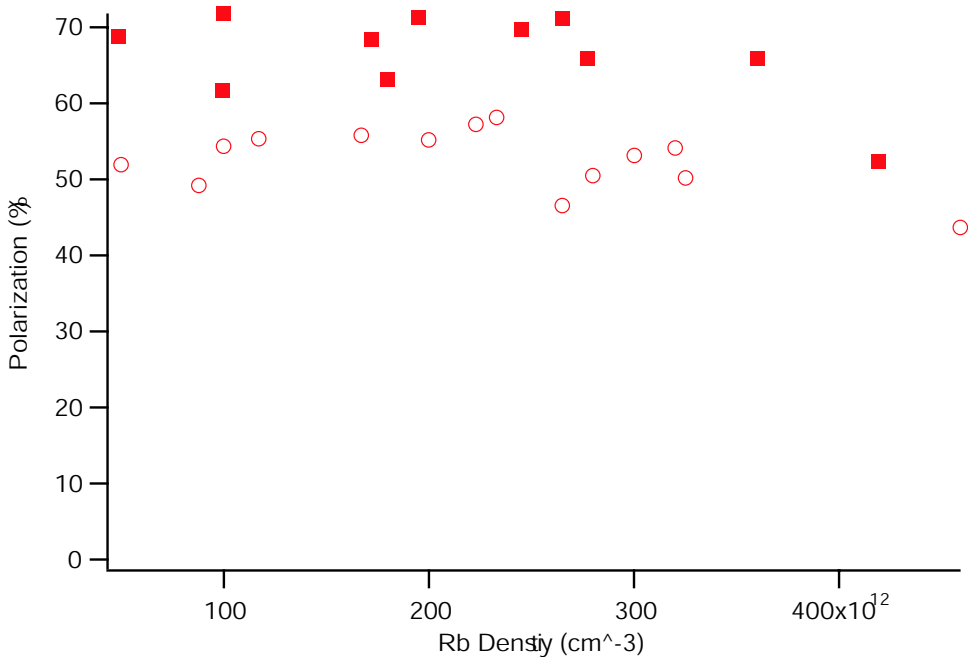

Figure 4.5: Graph showing the ^{3}He polarization obtained using a 14W narrowed Coherent external cavity diode array bar as compared to 42W of unnarrowed light (22W unnarrowed Coherent array and 20W Spectral Physics diode array bar) in NIST cell "Betty" with a cold lifetime of 240 hours. Circles are for the unnarrowed light and squares are the narrowed light. The spectral width of the unnarrowed diode array bar is about 750 GHz for the Coherent diode array and 1500 GHz for the Spectra Physics diode array.

Chapter 5

Rb-^{3}He Experimental Design

5.1 Introduction

The rest of this thesis describes extensive measurements on the Rb^{3}He spin-exchange rate coefficients. This chapter describes in detail the experimental methods and hardware use to measure the Rb-^{3}He spin-exchange rate coefficients. The rate coefficient measurements require us to measure the absolute ^{3}He polarization, ^{3}He relaxation rate, ^{3}He density Rb density, Rb polarization, Rb repolarization and Rb spin-relaxation.

Sections 5.2 to 5.4 describe the experimental hardware. In section 5.2 gives short description of the forced-air oven used for optical pumping and section 5.3 gives a list of all the Rb-^{3}He spin-exchange cells that were used to measure the Rb-^{3}He spin-exchange rate coefficients. Finally, in section 5.4 all the magnetic field coils are listed.

Sections 5.5 to 5.9 describe the experimental theory and methods. Section 5.5 is a description of the theory and experiment we used to determine the Rb polarization. It is a variant of the rf-spectroscopic method recently introduced by Young and coworkers [Young97] which is based on measuring the number of atoms in all the Zeeman sublevels. Section 5.6 describes in detail the three methods we used to measure the Rb density. We

used absorption spectroscopy, field-Faraday rotation, and polarization-Faraday rotation [Kadlecek00]. The Rb spin-relaxation rate is measured with a weak probe beam at low Rb polarization and is briefly described in section 5.7. Finally, in section 5.8 I describe the experimental method we used to measure the Rb repolarization.

Section 5.10 describes the absorption spectroscopy method for measuring ^{3}He density. The absolute ^{3}He polarization is measured using the well-established method of EPR resonance frequency shift of Rb atoms due to the polarized ^{3}He atoms [Romalis98]. Furthermore, we introduced a new method which is based on the NMR frequency of the ^{3}He atoms. These two methods are described in detail in section 5.11. The ^{3}He relaxation rate is measured by observing the free induction decay (FID) of the ^{3}He NMR signal using our custom-built low magnetic field NMR detection circuit [Abragam61]. This is described in detail in section 5.9.

The basic experimental set up to measure most of these parameters is shown in figure 5.1. Not included in the figure is the NMR pick up and sensing coil.

5.2 Forced-Air Oven

Our oven is made mostly from half-inch Teflon sheets with two glass windows in the front and back for optical access. It is assembled mostly from brass, aluminum and a few stainless steel screws. The front and back windows are 7"×7" square Pyrex with 3/8" thickness. The bottom of the oven is attached to a hot air duct provided by two heaters (Omega part-AHP5051). The air is delivered by 1/4" diameter copper tubing.

We use an infrared sensor that is mounted 10 cm above the oven to monitor the temperature. We avoid any detector that has to be attached directly next to the cell, since it might contaminated our NMR signal. The top of the oven has a 1" slot where a salt-glass window is inserted for best infrared transmission. On the cell

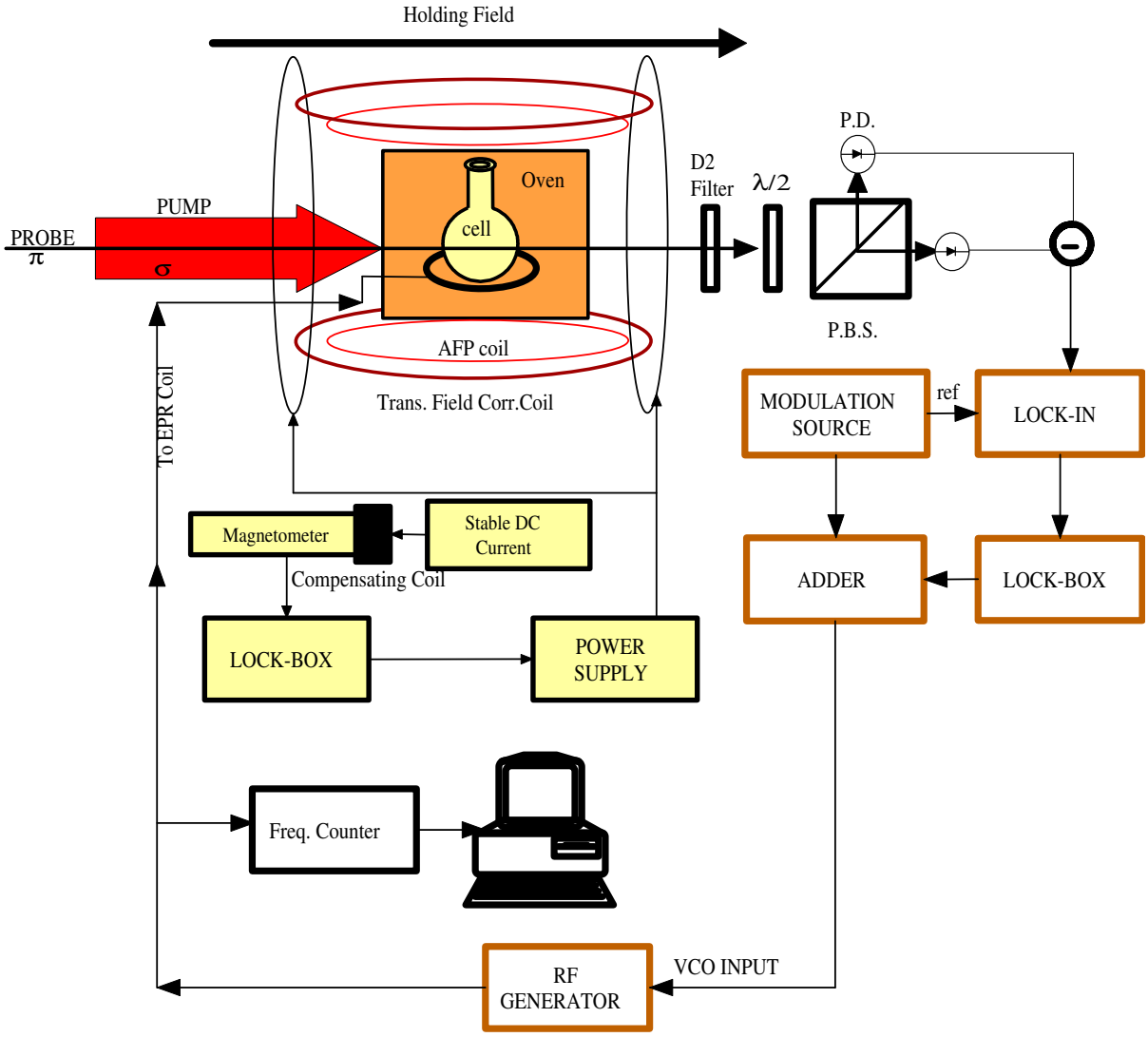

Figure 5.1: Experimental layout for measurements of Rb polarization, Rb re-polarization (field and polarization rotation), Rb spin-relaxation, and ^{3}He polarization. The transverse field correction coils are used to cancel the Earth's magnetic field. The magnetometer is used to stabilize the static holding field. Not shown in the figure is the ^{3}He NMR coil.

itself is a piece of high-heat black tape for the emission of the infrared signal. The infrared sensor is connected to a PID temperature controller (Omega-CN77000), which in turn provides 110 Volts to the process air heater as needed through a solid-state relay (Omega-SSR240DC25). The infrared sensor is calibrated with the standard RTD. The temperature controller stabilizes the oven to within a degree Celsius.

The oven is mounted on an XY-translation stage which in turn is mounted on an optical lab jack. This allows us to adjust the position of the cell for minimum magnetic field gradient.

5.3 Cells

We are very fortunate to have several beautiful cells on loan from Tom Gentile at NIST-Gaithersburg, two cells from New Hampshire, one from Amersham Health, one from Michigan, and one cell from Utah. Their life times range from 8.12 hours to 436 hours. All the cells and their parameters are listed in table 5.1. A picture of some of the cells is shown in figure 5.2. "Betty", "MichCell" and "Boris" are cylindrical cells with very well-defined geometries. They are made with a stock Corning 1720 body with GE180 windows. "BamBam" is also a cylindrical cell with the same stock Corning body but with ^{10}B-depleted Corning 1720 windows. "Barney" and "Natasha" are reblown GE180 cells. "Miti", "Saam", "Rb-K1", Bonnie, and "Rb-K2" are spherical GE180 cells.

5.4 Field Coils

Our spin-exchange optical pumping experiment is done at a low magnetic field. The holding field is about 9 gauss. For a shorter period of time the field can be turned up to 60 gauss. Other magnetic field coils are listed in table 5.2. These coils are:

Cell Name	[^{3}He]1 (amg)	[^{3}He]2 (amg)	[^{3}He]3 (amg)	Place	Lifetime (hrs)	Geometry (cm)	S/V (1/cm)
Betty	0.7443	0.7865	0.800	NIST	240	D=4.5 L=4.9	1.297
BamBam	0.839	0.7686	0.7542	NIST	119	D=9.6,L=4.7	0.842
Natasha	0.6	0.7684		NIST	436	D=5,L=5	1.2
Saam	2.5			Utah	115	D=3.25	2.7
Miti	2.725			N.C	182	D=7.1	0.845
MichCell	0.65	0.6656		Mich.	8.12	D=4.3, L=4.5	1.375
Barney	0.983	1.07		NIST	391	D=8, L=4	1
Boris		0.7732	0.7686	NIST	70	D=4.5,L=4.9	1.297
Bonnie		3.165		NIST	110	D=2.8	2.15
TimeBomb		2.713		NIST	6.8	D=4.0, L=1.4	2.3
SunShine				NIST	550	D=11.43	0.525
Rb-K1		3.27		N.H.	90	D=3.5	1.714
Rb-K3		3.3		N.H.		D=3.5	1.714

Table 5.1: Rb-^{3}He cells that were used in our experiment. "Betty", "MichCell" and "Boris" are cylindrical cells with a stock Corning 1720 body with GE180 windows. "BamBam" is also a cylindrical cell with the same stock Corning body but with ^{10}B-depleted Corning 1720 windows (for neutron beam). "Barney" and "Natasha" are reblown GE180 cells. "Miti", "Saam", "Bonnie", "SunShine", "Rb-K1", and "Rb-K2" are spherical GE180 cells. [^{3}He]1 density is measured using absorption spectroscopy. [^{3}He]2 is the density measured at the time of filling. [^{3}He]3 is the density measured using neutron beam spectroscopy. The density is in units of amagat. The lifetime is in hours and the length is in units of cm. All NIST cells are filled to 50 torr of N_2. The "Miti" cell has (3/4)% of N_2. S/V are the "actual" surface-to-volume ratio to account for some cells that have non-negligible stems.

Figure 5.2: Picture showing some of the Rb-^{3}He cells used to measure spin-exchange rate coefficients.

the adiabatic fast passage coil (AFP) used to measure the Helium polarization, the electron paramagnetic resonance (EPR) coil use to generate RF signal to measure the rubidium polarization, and transverse coil use to cancel the Earth's magnetic field and for studying skew light propagation (Appendix C). Also, we use a 2-turn correction coil to stabilize the magnetic field with the magnetometer. We use a single coil of 300 turns to detect the ^{3}He NMR signal . It is wound from 34 gauge magnet wire around a 9mm Teflon form. It serves as both the pulse and sensing coil. The coil is placed in a Teflon form with the appropriate cell sitting on top.

5.5 Rb Polarimetry

5.5.1 Introduction

Recently, Happer and coworkers [Young97] introduced a method to measure the absolute Rb polarization in an optically pumped cell. They used a weak circularly polarized probe beam perpendicular to the alkali polarization direction. Application of a transverse rf field at the Rb resonance frequency caused a polarization-dependent transmission modulated at the rf frequency. By scanning the rf frequency across all the Rb Zeeman sublevels, the relative populations of the levels can be obtained. The absolute Rb polarization is the appropriate ratio of these integrated areas of the sublevels. Here

Coil	Diameter(cm)	Wire gauge	Number turns	B-field	Power source
NMR coil	7	300	34	<<1	LabView
Holding field	100	14	135	30	Sorensen DHP
Holding field	58.5	14	54	30	HP 6574A
AFP	22	14	20	1	SRS DS345
EPR	9	14	7	1	SRS DS345
Tranverse	43	14	20	1	HP 6574A
Correction	100	14	2	0.5	HP 6574A

Table 5.2: Field coils used in our experiment. Diameter is in units of cm and the magnetic field is in units of gauss.

we introduce a variation of this method. It is based on polarization-Faraday rotation [Kadlecek00] [Wu86][Vliegen01]. Instead of sending the probe beam perpendicular to the pumped cell, we send a linearly polarized weak probe beam along the alkali-metal polarization axis. Since the alkali-atoms are polarized, when rf frequency is applied at the Rb resonance this causes the probe beam to rotate due to polarization-Faraday rotation. This rotation angle is proportional to the Rb density. By scanning the rf frequency across all the Zeeman sublevels of the Rb atoms we can get the relative populations of all the sublevels.

5.5.2 Theory

The Hamiltonian for an alkali-metal atom sitting in a transverse sinusoidal magnetic field with amplitude B_x is

$$H = \sum_m E_m |m\rangle\langle m| + g_s \mu_B S_x B_x \cos\omega t \tag{5.1}$$

If we assume well-resolved resonances, the equation of motion for the coherence between state $|m\rangle$ and state $|m-1\rangle$, $\rho_{m,m-1}$, is

$$\frac{\mathrm{id}\rho_{\mathrm{m,m-1}}}{\mathrm{dt}} = (E_m - E_{m-1} - \omega)\rho_{m,m-1} - i\gamma\rho_{m,m-1} + V_{m,m-1}(\rho_{m-1} - \rho_m), \tag{5.2}$$

where ρ_m and ρ_{m-1} is the probability to be in state $|m\rangle$ and $|m-1\rangle$ with energy E_m and E_{m-1}, respectively. γ is the decay rate. If we assume that the coherence can be written as $\rho_{m,m-1} = \sigma \exp^{-i\omega t}$, then the above equation can be written as

$$id\sigma/dt = (E_m - E_{m-1} - \omega)\sigma - i\rho\sigma/2 + \langle m|V|m-1\rangle(\rho_{m-1} - \rho_m)/2 \tag{5.3}$$

where $V = g_s\mu_B S_x B_x$. In steady state, equation 5.3 becomes

$$\sigma = \frac{\langle \mathrm{m|V|m-1}\rangle}{2(\Delta + \mathrm{i}\gamma/2)}(\rho_{m-1} - \rho_m), \tag{5.4}$$

where $-\Delta = (E_m - E_{m-1} - \omega)$. The equations of motion that govern the behavior of the density of the sublevels $|m\rangle$ and $|m-1\rangle$ can be shown to be

$$id\rho_m/dt = \langle m|V|m-1\rangle\sigma^*/2 - \langle m-1|V|m\rangle\sigma/2 \tag{5.5}$$

$$id\rho_{m-1}/dt = \langle m-1|V|m\rangle\sigma/2 - \langle m|V|m-1\rangle\sigma^*/2 \tag{5.6}$$

From the last three equations it can be shown that, assuming a single resonance is being driven by the RF field,

$$\begin{aligned} dF_z/dt &= \frac{|\langle \mathrm{m|V|m-1}\rangle|^2\gamma(\rho_{\mathrm{m-1}} - \rho_{\mathrm{m}})}{\Delta^2 + \gamma^2/4} \\ &= (\frac{\gamma}{\Delta^2 + \gamma^2/4})(g_s\mu_B B_x/(2I+1))^2(F(F+1) - m(m-1))(\rho_{m-1} - \rho_m)/4 \end{aligned} \tag{5.7}$$

where $dF_z/dt = d(\rho_m - \rho_{m-1})/dt$. Thus, the signal observed will be proportional to $(F(F+1) - m(m-1))(\rho_m - \rho_{m-1})$.

From the last equation and assuming a "spin-temperature" distribution equilibrium [Anderson59], the ratio of area under two successive peaks is

$$\frac{\mathrm{F(F+1) - m(m-1)}}{\mathrm{F(F+1) - (m-1)(m-2)}}e^{\beta} \tag{5.8}$$

For ^{85}Rb atoms in hyperfine level $F = 3$, the ratio of the two areas is (F=3, $m_F = 3 \rightarrow F = 3, m_F = 2$ and $F = 3, m_F = 2 \rightarrow F = 3, m_F = 1$ resonances)

$$A = (3/5)e^{\beta}. \tag{5.9}$$

Also, the equation for the electron spin polarization in terms of spin-temperature parameter β is [Happer72] [Walker97]

$$P = 2\langle S_z \rangle = \tanh(\beta/2) = \frac{\mathrm{e}^{\beta/2} - \mathrm{e}^{-\beta/2}}{\mathrm{e}^{\beta/2} + \mathrm{e}^{-\beta/2}} = \frac{\mathrm{e}^{\beta} - 1}{\mathrm{e}^{\beta} + 1} \tag{5.10}$$

But from equation 5.9 $e^{\beta} = (5/3)A$, hence for ^{85}Rb, the polarization is

$$P = \frac{5\mathrm{A} - 3}{5\mathrm{A} + 3} \tag{5.11}$$

In practice we work with a magnetic field that is less than 50 Gauss, the ($F = 2, m_F = 2 \rightarrow F = 2, m_F = 1$) and the ($F = 3, m_F = 2 \rightarrow F = 3, m_F = 1$) peaks are very close together. In that case the ^{85}Rb polarization can be shown to be

$$P = \frac{7\mathrm{A}_{85} - 3}{7\mathrm{A}_{85} + 3}, \tag{5.12}$$

where A_{85} is the ratio of the ($F = 3, m_F = 3 \rightarrow F = 3, m_F = 2$) area to the combined area of ($F = 3, m_F = 2 \rightarrow F = 3, m_F = 1$) and ($F = 2, m_F = 2 \rightarrow F = 2, m_F = 1$) resonances. A similar equation in ^{87}Rb is

$$P = \frac{3A_{87} - 2}{3A_{87} + 2}, \tag{5.13}$$

where A_{87} is the ratio of the ($F = 2, m_F = 2 \rightarrow F = 2, m_F = 1$) area to the area of ($F = 2, m_F = 1 \rightarrow F = 2, m_F = 0$). In the unresolved case, the equation becomes

$$P = \frac{2\mathrm{A}_{87} - 1}{2\mathrm{A}_{87} + 1}, \tag{5.14}$$

where A_{87} is the ratio of the ($F = 2, m_F = 2 \rightarrow F = 2, m_F = 1$) area to the combined area of ($F = 2, m_F = 1 \rightarrow F = 2, m_F = 0$) and ($F = 1, m_F = 1 \rightarrow F = 1, m_F = 0$) resonances.

5.5.3 Experiment

Of course, if the magnetic field is low, all the sublevels are roughly degenerate and there is only one resonance. The magnetic field we need to separate the resonances can be estimated using the famous Breit-Rabi formula [Ramsey56]

$$E_{F,m} = -\frac{\Delta \mathrm{E}}{2(2\mathrm{I}+1)} - g_I \mu_o B_o m \pm \frac{\Delta \mathrm{E}}{2}\sqrt{1 + \frac{4\mathrm{mx}}{2\mathrm{I}+1} + x^2}, \tag{5.15}$$

where F is the total angular momentum, m is the quantum projection of F along the quantized axis, and

$$x = \frac{-\mathrm{g_J}\mu_\mathrm{o} + \mathrm{g_I}\mu_\mathrm{o}}{\Delta \mathrm{E}} B_o. \tag{5.16}$$

ΔE is the energy difference between the two hyperfine energy levels. The $(\pm)$ signs are for $F = I \pm 1/2$ hyperfine levels. We expand the formula to the second order in terms of x^2 which gives

$$E_{F,m} = -\frac{\Delta \mathrm{E}}{2(2\mathrm{I}+1)} - g_I \mu_o B_o m \pm \frac{\Delta \mathrm{E}}{2}\left[1 + \frac{4\mathrm{mx}}{2\mathrm{I}+1} + x^2/2(1 - \frac{4\mathrm{m}^2}{(2\mathrm{I}+1)^2})\right] \tag{5.17}$$

The resonance frequency between two Zeeman sublevels $(F, m \leftrightarrow F, m-1)$ is

$$|\omega| = \frac{\left|\mathrm{E_{F,m}} - \mathrm{E_{F,m-1}}\right|}{\hbar}, \tag{5.18}$$

or approximately

$$|\omega| \approx \frac{\omega_\mathrm{o}}{2\mathrm{I}+1} + \frac{\omega^2}{(2\mathrm{I}+1)^2}\left[\frac{1-2\mathrm{m}}{\omega_\mathrm{HFS}}\right] \pm \frac{g_I}{g_j}\omega_o, \tag{5.19}$$

where

$$\omega_{HFS} = \frac{\Delta E}{\hbar} \tag{5.20}$$

$$\omega_o = \frac{g_J \mu_o B_o}{\hbar}, \tag{5.21}$$

and the sign $(\mp)$ applies to $F = I \pm 1/2$ hyperfine levels. From equation 5.19 we can make a quick approximation of the splitting between the adjacent transitions

$$|\omega|_{F,m\to F,m-1} - |\omega|_{F,m-1\to F,m-2} = \frac{2\omega_o^2}{\omega_{HFS}(2I+1)^2} \tag{5.22}$$

Thus, the splitting is proportional to the square of the magnetic field.

Assume that the width of each resonance is about 50 KHz, which corresponds to a cell temperature of about 170C, hence we want a separation of at least 100 KHz between two adjacent sublevels. With 100 KHz separation, the above equation says that we need at least 25 gauss for ^{85}Rb. Experimentally, you need at least this much magnetic field. At higher temperatures, since the width of each resonance is dominated by spin-exchange, you need a higher field to separate the peaks. Most of the time the applied static magnetic field we used was 34 gauss.

To measure the Rb polarization, we set the oven to the desired temperature and tune the pump beam on resonance. We fix the rf frequency at 16 MHz and amplitude-modulate it at about 500 Hz to 2 KHz. We then sweep the magnetic field across the Rb resonances. The total sweep span is about one to two gauss. The raw signal is sent to the lock-in amplifier and is mixed with the reference frequency. The output is sent to the oscilloscope, where it is recorded. Figure 5.3 shows the experimental setup. Figure 5.4 shows a sample of ^{85}Rb polarization spectrum taken at temperature 155C with low Rb polarization to show all the 6 peaks from $F = 3$ and 4 peaks from $F = 2$ ground states. Figure 5.5 shows the ^{85}Rb polarization spectra taken at 183C at various positions on the cell. Notice the narrowing of the F=3, $m_F = 3 \rightarrow F = 3, m_F = 2$ peak as the polarization is getting higher [Appelt99].

5.6 Rb Density Measurement

5.6.1 Introduction

To make any reasonable measurement of spin-exchange rate coefficients, we need to measure the absolute Rb density. Inferring the Rb density from the temperature sensor

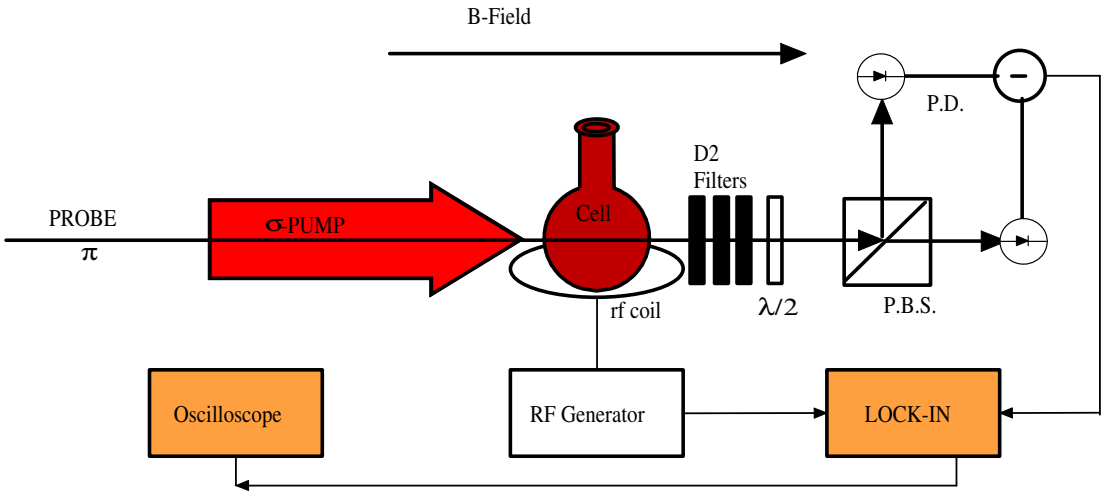

Figure 5.3: EPR spectroscopy optical setup.

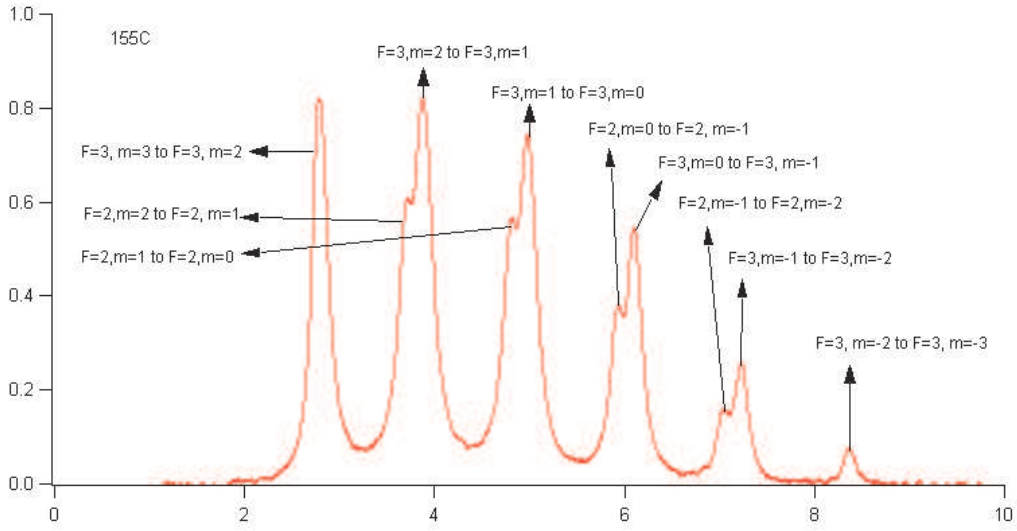

Figure 5.4: ^{85}Rb polarization spectrum taken at 155C and low polarization. Note the 6 peaks from $F = 3$ states and 4 peaks from $F = 2$ states. The relative areas under the resonance peaks determine the Rb polarization.

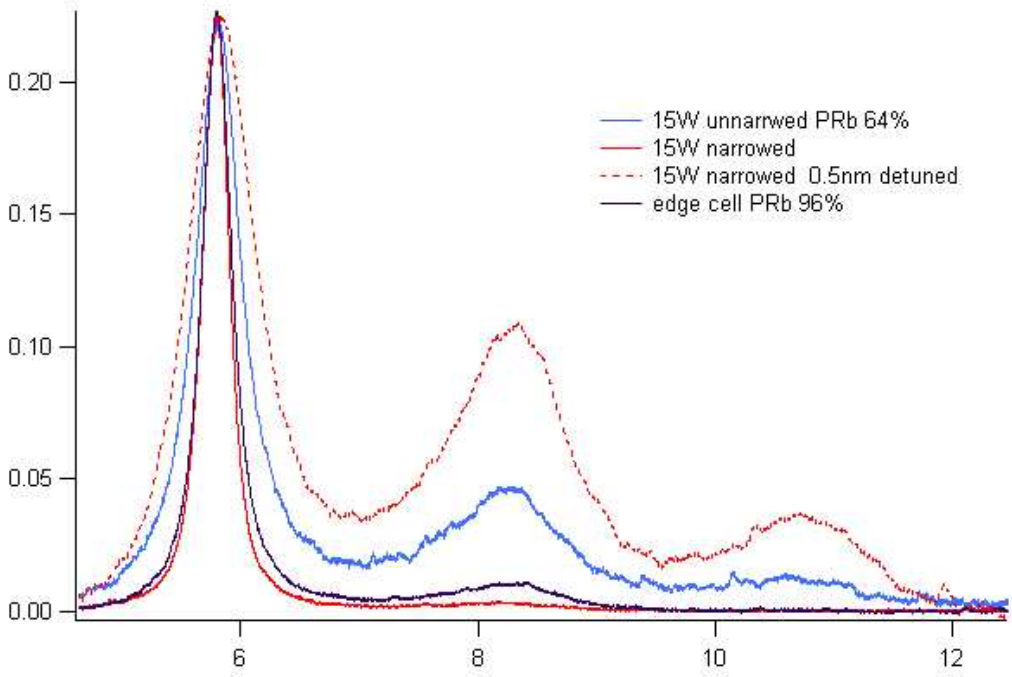

Figure 5.5: ^{85}Rb polarization spectra taken at 183C. The four spectra shown are with the probe at the center of the cell and 1 mm from the edge of the cell, with laser off resonance, and broadband laser. Notice the narrowing of the F=3, $m_F = 3 \rightarrow F = 3, m_F = 2$ peak as the polarization is getting higher.

and the vapor pressure curve is not reliable enough. Most of the time the Rb density that we measured did not correspond to what was expected from the temperature reading on the cell. This is probably due to a combination of an inaccurate sensor and the fact that temperature at the surface of the cell is not the same temperature as at the center of the cell [Walter01] and possible unknown chemical reactions.

We rely mostly on Faraday rotation of the probe light to do our density measurements [Kadlecek00] [Wu86] [Vliegen01]. We use field Faraday rotation, polarization Faraday rotation, and sometimes absorption spectroscopy to deduce the Rb density.

5.6.2 Field Faraday Rotation

The rotation angle, for probe detuning much greater than the atomic linewidth and hyperfine structure, as a function of Rb density and magnetic field is [Kadlecek00] [Vliegen01] [Chann02a] (Appendix D)

$$\theta_B = \big[Rb\big] \frac{le^2 \mu_B B}{18mhc} \left(\frac{4}{\Delta_{1/2}^2} + \frac{7}{\Delta_{3/2}^2} - \frac{2}{\Delta_{3/2}\Delta_{1/2}} \right), \tag{5.23}$$

where, for example, $\Delta_{3/2} = \nu - \nu_{3/2}$ is the detuning of the probe from the $nS_{1/2} \rightarrow nP_{3/2}$ transition. Here e is the electronic charge, μ_B is the Bohr magneton, m is the electron mass, h is Planck's constant, l is the path length of the probe through the cell, c is the speed of light, B is the external applied magnetic field, and $[Rb]$ is the Rb density.

We do not have a one Tesla magnetic field available for the Rb^{3}He apparatus. Thus, our rotation angle at about 150 GHz detuning from resonance is only a fraction of a degree. To measure such a small angular rotation, we use a photoelastic modulator (PEM) and a lock-in amplifier. When a circularly polarized probe light is passed through the PEM it gets modulated at the PEM's frequency, 50 KHz. After the probe passes through the cell, it goes through our standard Faraday rotation detector as first described in 2.3.3. The raw signal is then mixed with the 50 KHz reference signal at the

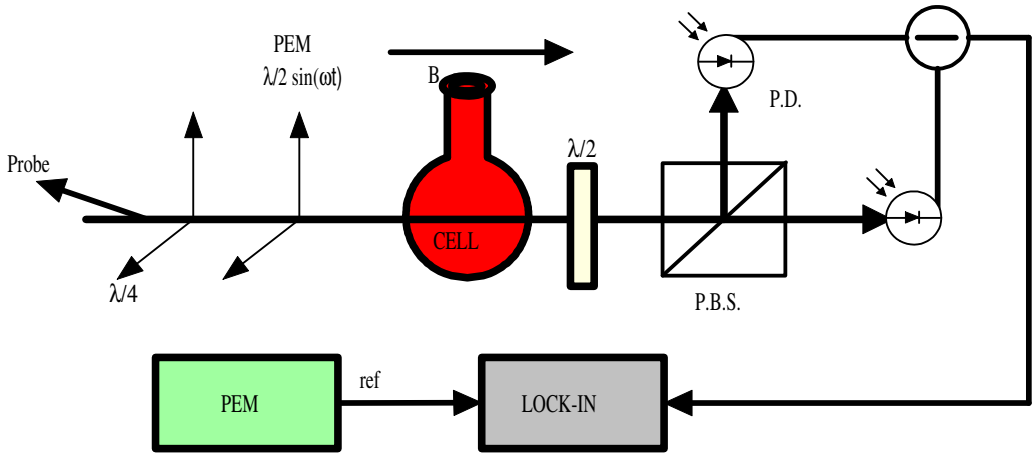

Figure 5.6: Optical setup using field Faraday rotation with photoelastic modulator to measure Rb density.

lock-in amplifier. The optical setup is shown in figure 5.6. It can be shown that, after mixing with the raw signal with the fundamental frequency with a lock-in amplifier the output signal is [Nelson01]

$$V = -2J_1(\beta)\sin 2\phi e^{-n\sigma l}, \tag{5.24}$$

where J_1 is the first order Bessel function and β is the retardation of the photoelastic modulator.

5.6.3 Polarization Faraday Rotation

At large detuning compared to atomic linewidth and hyperfine structure, the Faraday-rotation angle as a function of polarization is given as [Kadlecek00] [Vliegen01] [Chann02a] (Appendix D)

$$\theta_P = \frac{[Rb]le^2}{6mc}\left(\frac{1}{\Delta_{3/2}} - \frac{1}{\Delta_{1/2}}\right)P. \tag{5.25}$$

To measure the Rb density we send a linearly polarized probe light to the cell. The pump beam is then chopped at a few Hertz by an optical chopper. The probe is passed

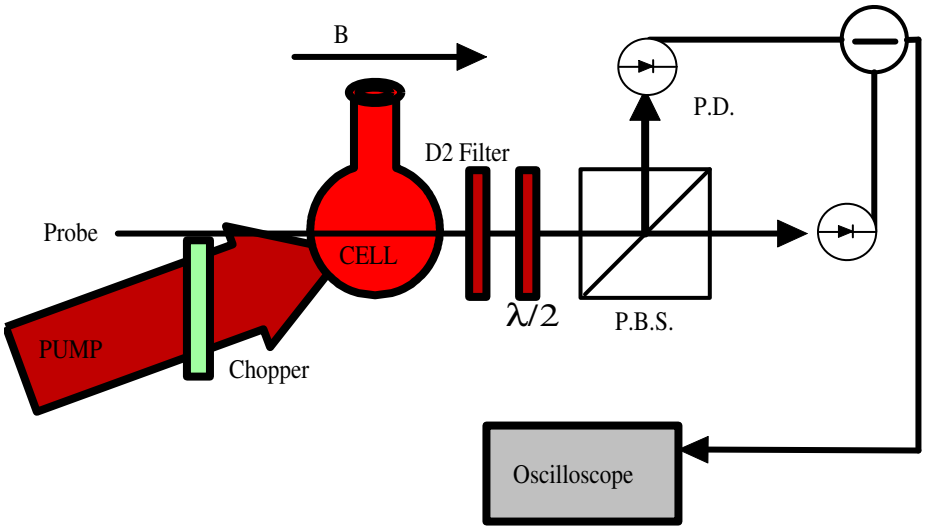

Figure 5.7: Optical setup using polarization Faraday rotation to measure Rb density.

through the cell and is then detected with our Faraday rotation detector. When the pump beam is blocked by the chopper we make sure that the Rb atoms are completely depolarized by allowing the blocking time to be at least 5 relaxation time-constants. If the Rb is not completely depolarized the measured rotation angle will be smaller than the actual rotation which will result in inaccurate Rb density measurement. The rotation angle is measured by rotating the signal and calibrating to the angle on the half-wave plate. The rotation angle is typically many tens of degrees at about 1000 GHz from resonance. We then measure the Rb polarization. From the rotational angle and Rb polarization, the Rb density can be determined through equation 5.25. The optical set up is shown in figure 5.7.

5.6.4 Absorption Measurement

As a further consistency check, we also measure the Rb density using a more laborious method of absorption spectroscopy of the $5s \rightarrow 6p$ transitions. The two transitions of interest are 420.185nm and 421.552 nm which correspond to the $p_{3/2}$ and $p_{1/2}$, respec-

tively. The $5s \rightarrow 5p$ transitions are not suitable for this because the large oscillator strengths make the cell extremely optically thick under our experimental conditions.

The absorption spectroscopy is based on the following formula [Kadlecek00] [Romalis97]

$$\int_{-\infty}^{\infty} \sigma(\nu) d\nu = \pi r_e f c, \tag{5.26}$$

where f is the oscillator strength, $r_e = 2.82 \times 10^{-13}$ cm is the classical electron radius, and $\sigma(\nu)$ is the absorption cross section. Also, the intensity transmitted through the cell I_T is given by

$$I_T = I_0 e^{-[Rb]\sigma(\nu)L}, \tag{5.27}$$

where $[Rb]$ is the Rb density and L is the length of the cell. From these two equations and the known oscillator strengths [Migdalek98], the Rb density can be determined. For the $6p_{1/2}$ state, we take the average of the two experimental values of 4×10^{-3} and 3.75×10^{-3}. For the $6p_{3/2}$ state, we take the average of the two experimental values of 9.37×10^{-3} and 9.54×10^{-3}.

We use an external cavity 830nm-Hitachi diode with maximum free-running power output of 150mW. We double about 80-90 mW of 838-846nm to fully resolve the $s_{1/2} \rightarrow p_{1/2}$ and $s_{1/2} \rightarrow p_{3/2}$ resonances [Hetch87]. The pump beam output is focused onto the 1 cm cube $LiIO_3$ crystal by a 200mm biconvex lens. Typical blue-light power output is a fraction of a microwatt. The blue light is split before the cell into two beams. One beam is for measuring the laser power. The second beam passes through the cell where the transmission is measured as the frequency is scanned across the resonances. In both cases we use a narrowband interference filter (CVI part F10-420-0-4-0.5) and a blue-light sensitive photodiodes (Hamamatsu G1893). For better signal-to-noise ratio we chop the pump beam with an optical chopper.

The resulting transmission spectra are then fitted to determine the areas under the $5s \rightarrow 56p_{(1/2,3/2)}$ peaks. With the known oscillator strengths, the Rb density can be

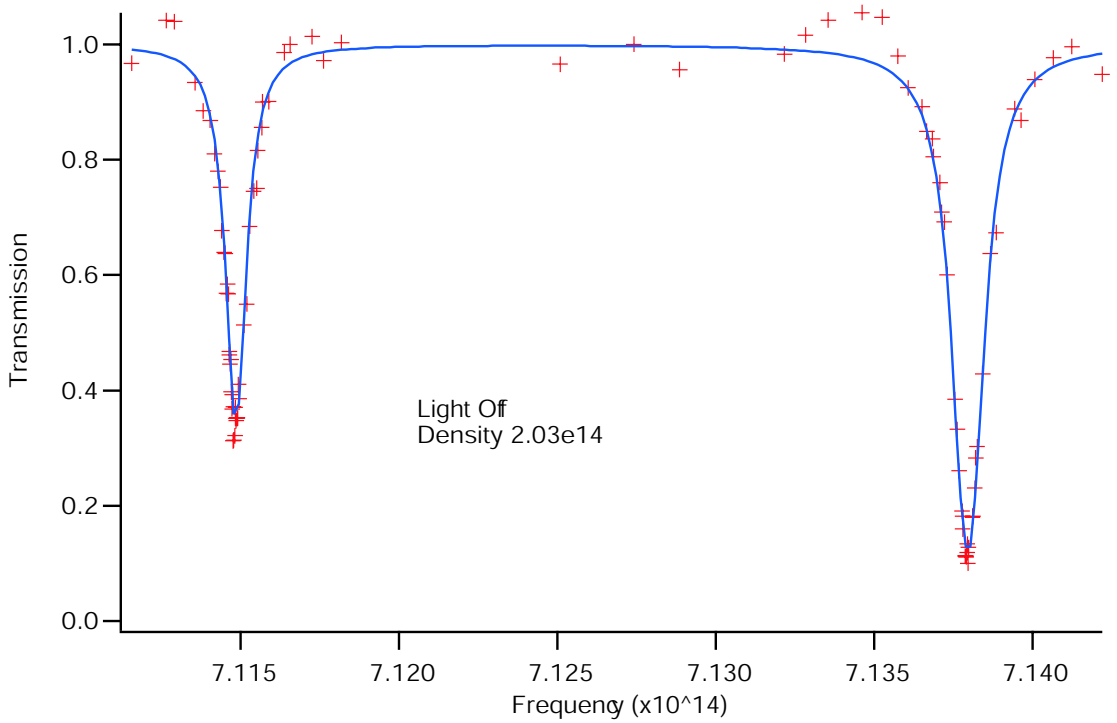

Figure 5.8: Measurement of transmission of probe light on the second resonance as a function of probe frequency with the pump light off. Points are the experimental data and the line is the fit.

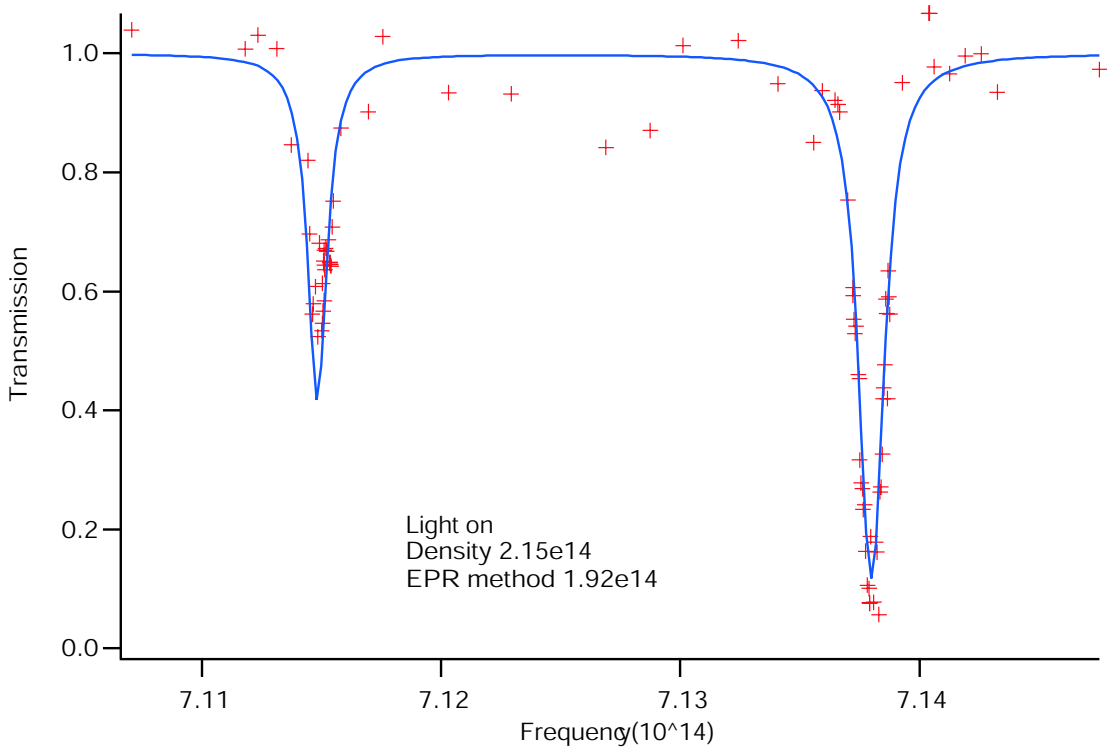

Figure 5.9: Transmission of probe light of the second resonance as a function of probe frequency with the pump light on

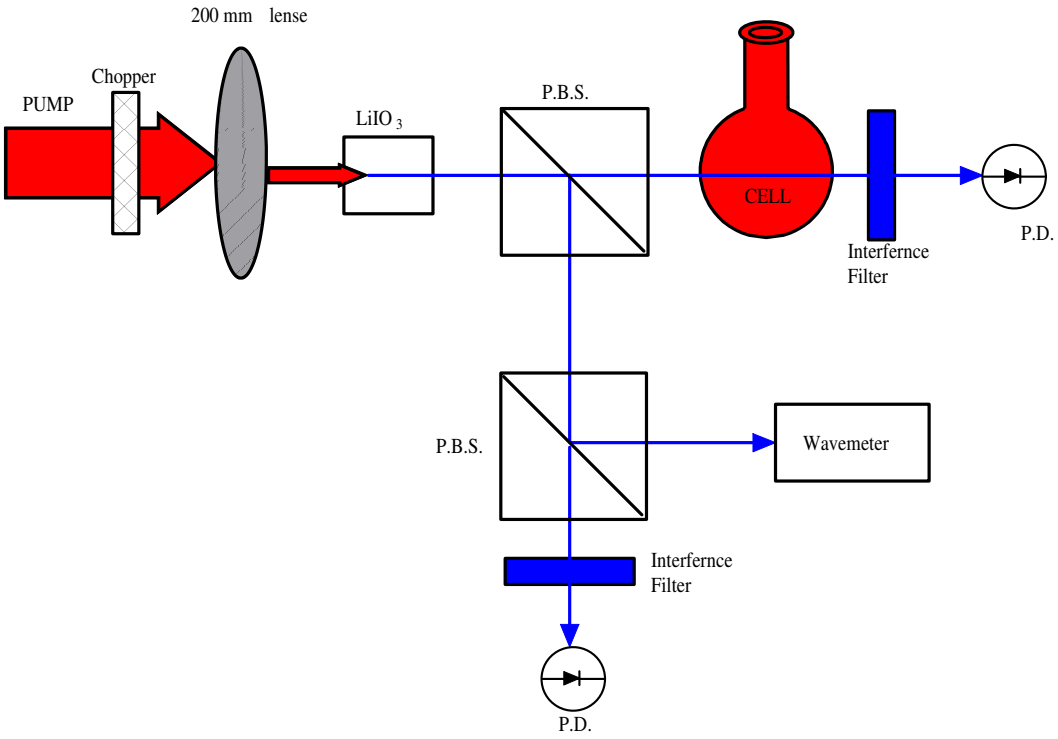

Figure 5.10: Frequency doubling cavity used to measure Rb density.

deduced.

Figure 5.8 shows the spectra taken with the pump light off. Figure 5.9 shows the spectra with the pump light on. The noise is due to a combination of very low blue light probe intensity, spurious pump light, and the alignment associated with frequency doubling. The optical setup is shown in figure 5.10. As shown in table 5.3 the discrepancy in Rb density between the pump light on and off is about 15%. Also shown in table 5.3 are the results of the different methods: field Faraday rotation, polarization Faraday rotation, and absorption spectroscopy .

Method	Density (10^{14} cm^{-3})
Field Faraday Rotation	1.91
Polarization Faraday rotation	1.92
Absorption- light on	2.15
Absorption- light off	2.03

Table 5.3: Table shows the results of the different methods: field Faraday rotation, polarization Faraday rotation, and absorption spectroscopy to measure the Rb density.

5.7 Rb spin-relaxation

The Rb spin-relaxation measurement is done using the standard "relaxation in the dark" method [Franzen59]. In our experiment, first we turn down the pump laser power to a few watts. At the same time we detune it a few nm from resonance. This is done to ensure that the Rb polarization is less than a few percent. We also check this method with the repolarization rate method, as described in the next subsection. The two methods agree to within a few percent.

5.8 Rb repolarization

In the absence of pumping light, the Rb atoms are polarized through spin-exchange with the polarized ^{3}He [Baranga98]. Typical Rb repolarization is a small fraction of a percent, hence we use the photoelastic modulator to enhance our signal-to-noise ratio. The setup is shown in figure 5.11. To measure the Rb repolarization, we apply a 2 Hz square-wave amplitude-modulated rf frequency at the Rb resonance that strongly saturates the Rb resonance. The applied static magnetic field is kept less than 8 gauss. This ensures that all the RB sublevels are roughly degenerate and hence the rf pulse is

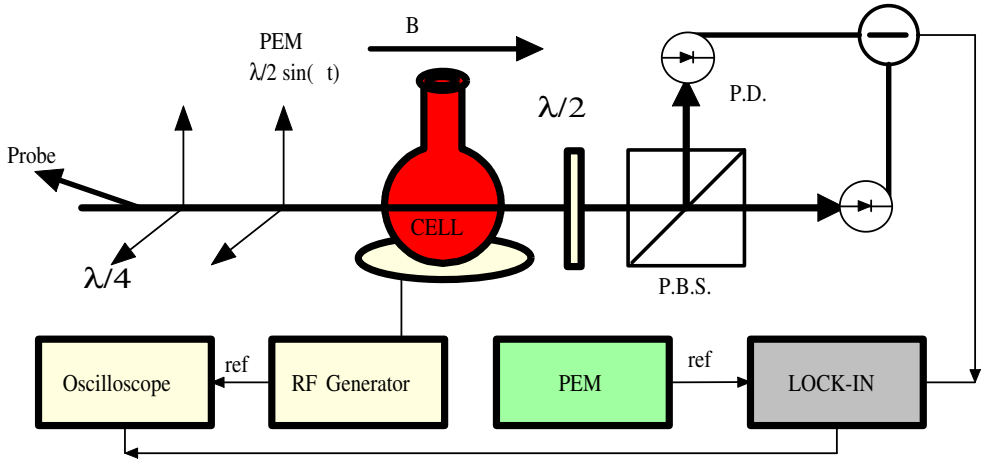

Figure 5.11: Optical setup used to measure the Rb repolarization.

very efficient in destroying the Rb repolarization. The Rb repolarization is calibrated by comparing the Faraday rotation angle of the re-polarized Rb atoms with the fully polarized atoms. A sample of Rb repolarization signal is shown in figure 5.12.

5.9 ^{3}He NMR

To detect the polarization of ^{3}He we use a custom-built Labview controlled NMR system. A single coil of 300 turns is wound from 34 gauge magnet wire around a 9mm Teflon form. It serves as both the pulse coil and sensing coil. The coil is placed in a Teflon form with the appropriate cell sitting on top. To detect the polarization, a short pulse of about 0.4 ms with an amplitude typically of about 0.4V is sent to the coil. The pulse is generated by the Labview program. The resonance pulse, at 24.54 KHz (3.243 KHz per Gauss), tips the longitudinal polarization of the Helium polarization. This tip creates a transverse magnetization [Abragam61]

$$M = M_z \sin\theta e^{-t/T_2}, \tag{5.28}$$

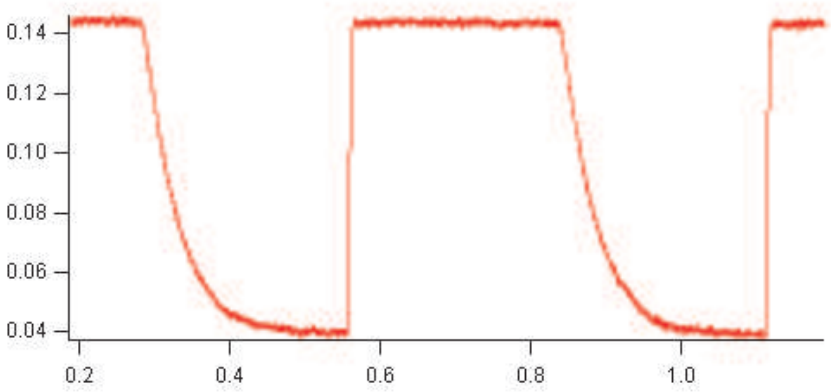

Figure 5.12: A typical repolarization signal of Rb atoms using the rf chopper.

where T_2 is the transverse relaxation of the polarization and θ is the tipping angle. The transverse magnetization induces a voltage in the pick up coil

$$V = QE, \tag{5.29}$$

where Q is the Q of the coil and E is the emf induced in the coil by the precessing magnetization, which is given by Faraday law

$$E = \omega M_z A \sin\theta e^{-t/T_2}, \tag{5.30}$$

where ω is the Larmor precession frequency and A is the area of the pick up coil. The picked up signal is sent to a Stanford Research Systems 830 lock-in amplifier. The lock-in phase sensitive detector (PSD) multiplies the atoms' signal,

$$V_a \sin(\omega_a t + \phi_a) \tag{5.31}$$

by the reference signal,

$$V_{ref} \sin(\omega_{ref} t + \phi_{ref}), \tag{5.32}$$

The output signal is

$$V_{out} = (1/2) V_a V_{ref} \sin\left((\omega_a - \omega_{ref})t + (\phi_a - \phi_{ref})\right) e^{-t/T_2} \tag{5.33}$$

Using the lock-in amplifier, we mix the signal down to 50-100 Hz from the ^{3}He resonant frequency. The mixed down signal is read by the DAQ card. Both the time and frequency domain are displayed on the computer and both are fitted by Labview. The time domain signal is fitted to the form

$$V(t) = V\sin(\omega t + \phi)e^{-t/T_2}, \tag{5.34}$$

where V, ω, ϕ and T_2 are the free parameters. V is the initial induced voltage, which is proportional to the ^{3}He magnetization. Since the signal is mixed down, V is sensitive to the mixed down frequency or the fluctuation in the magnetic field. Thus, we correct for this with the appropriate roll-off gain. Figure 5.13 shows the NMR detection circuit. Figure 5.14 shows a typical free-induction decay signal of the ^{3}He atoms and figure 5.15 shows a typical ^{3}He spin-up curve.

5.10 ^{3}He Density Measurement

A potentially important uncertainty in our ^{3}He polarization and thus the spin-exchange rates is due to the uncertainty in ^{3}He density. We independently measure the ^{3}He density using the absorption profiles of the pressure broadened D1 and D2 lines of the Rb atoms. We use a New Focus laser (model 6200) in the Littman-Metcalf configuration as the probe laser. The probe is sent through a half-wave plate which is then passed through an optical chopper. After it passes through the optical chopper the probe is sent through two pieces of glass. The reflection from the first piece of glass is sent to a photodiode to monitor the laser power. The reflection from the second piece of glass is sent to the New Focus Fizeau wavemeter. The rest of the probe is sent to the cell. The setup is shown in figure 5.16.

We heat the cell to about 80C. Using the precision line-broadening parameters of

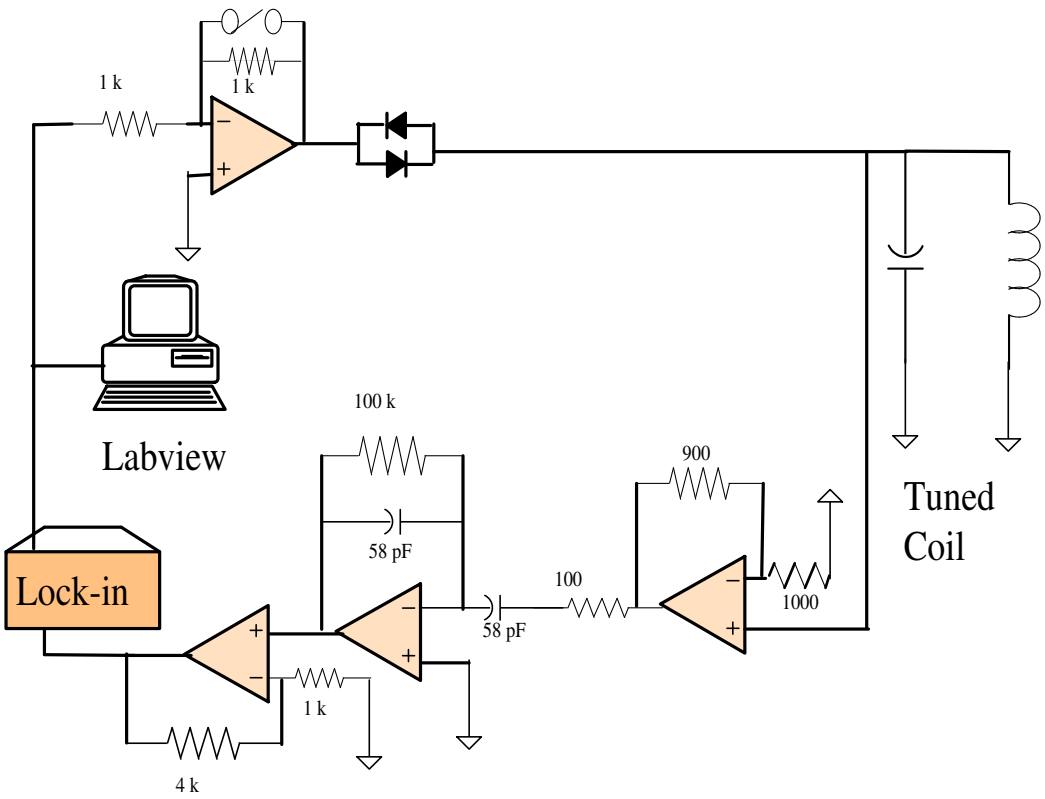

Figure 5.13: NMR detection circuit used to observe the ^{3}He relaxation rate.

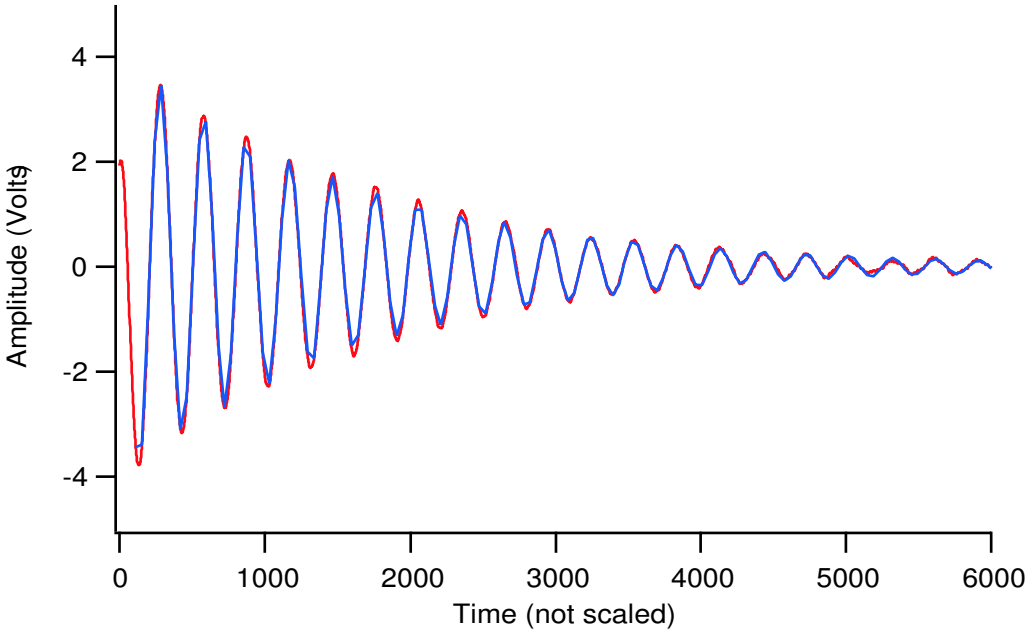

Figure 5.14: Free induction decay (FID) signal of Helium atoms. Also shown is a fit.

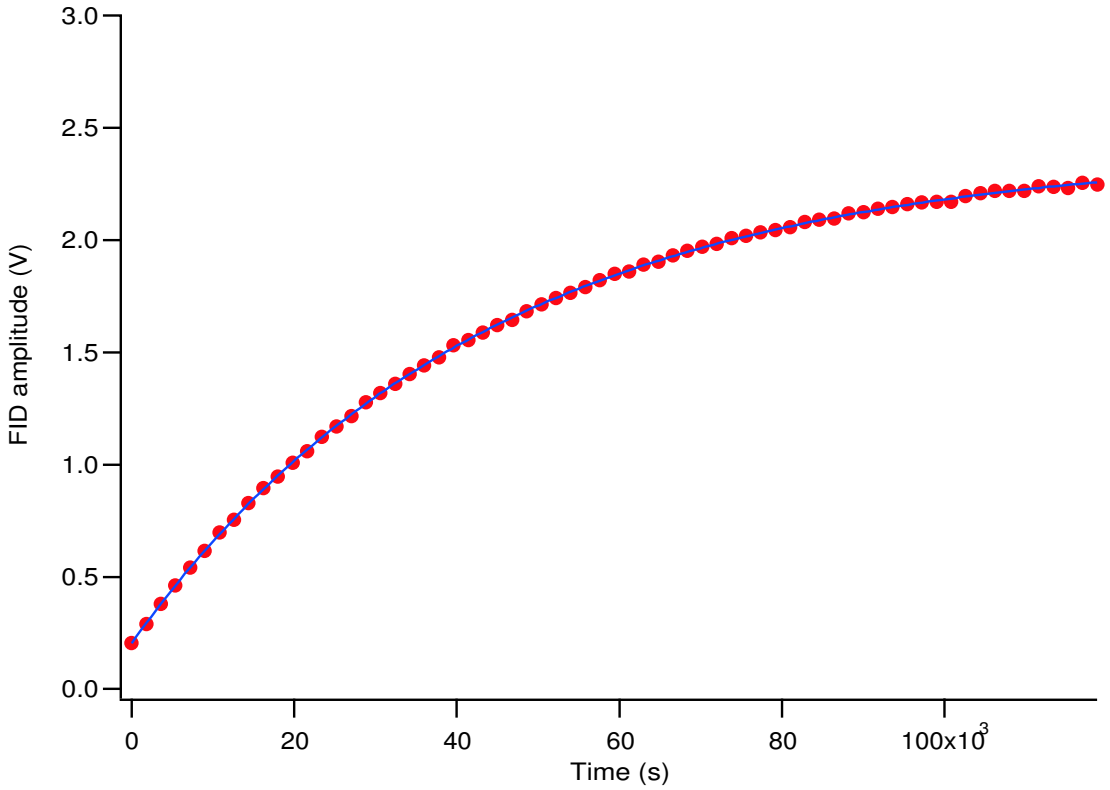

Figure 5.15: A sample ^{3}He NMR FID amplitude plotted as a function of time.

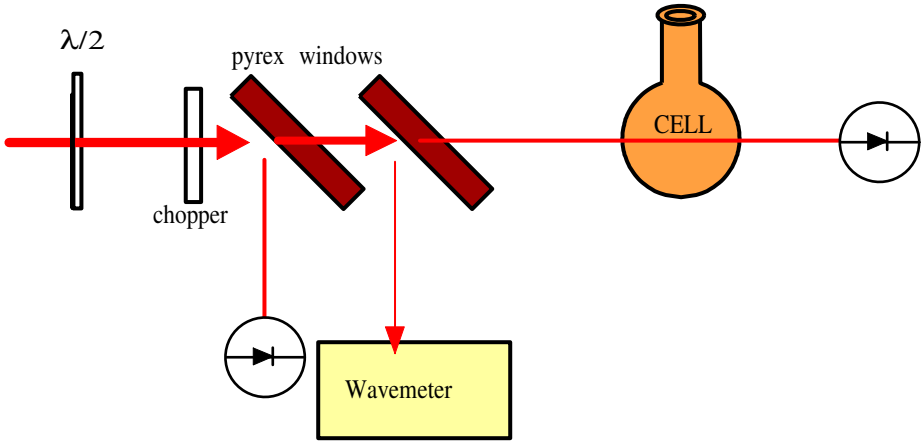

Figure 5.16: Optical setup used to measure ^{3}He density.

Romalis and coworkers [Romalis97] we fit the absorption profiles to four Lorenzians, two for each Rb isotope. The only free parameter is the width of the spectrum. We ignore the hyperfine structure of the excited states. The contribution should be very small compared to the ground states splitting. After the contribution from the buffer gas is subtracted out of the total width of the absorption spectrum, the density of the ^{3}He can be determined. A sample density absorption spectrum of one of our cells (Betty) is shown in figure 5.17.

5.11 ^{3}He polarimetry

5.11.1 Introduction

It is very important for us to have an accurate method of measuring the ^{3}He polarization. One of the most common methods is to compare the NMR signal of the polarized ^{3}He with the signal of the thermally polarized protons in an identically shaped water cell [Romalis98b]. This can be done with high precision but it is difficult to implement. To have an reasonable signal requires a high magnetic field, on the order of a Tesla

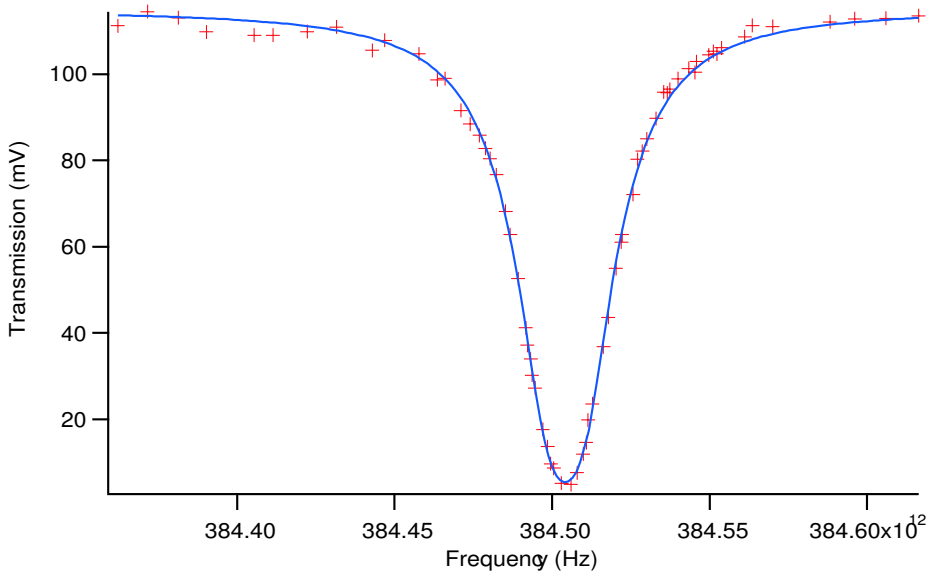

Figure 5.17: Pressure broadening spectra of the Rb atoms due to ^{3}He.

or higher. Furthermore, complications with cell geometry, and signal -temperature-variation have to be taken into account. Another method is to measure the static magnetic field produced by the noble nuclei directly outside the cell [Wilms97]. A third method of measuring ^{3}He polarization relies on neutron beam spectroscopy [Jones00] [Heil99].

We cannot measure the ^{3}He polarization using any of these three methods. Firstly, our NMR system works at low magnetic field, where proton polarization is small. Secondly, our Rb-^{3}He cells are low pressure, thus the magnetic field produced outside the cell is extremely small. Lastly, we do not have a nuclear reactor at our disposal to implement the neutron beam method. Hence, we choose to measure the ^{3}He polarization using the well-established method of measuring the Rb Zeeman frequency shift due to the polarized ^{3}He [Schaefer89] [Newbury93] [Barton94] [Romalis98]. This Rb Zeeman frequency shift is proportional to the ^{3}He polarization and density. The frequency shift also depends on the enhancement factor k_0 which is known very accurately [Romalis98].

In addition, we introduce a fourth method to measure the ^{3}He polarization. We measured the ^{3}He polarization by measuring the NMR frequency shift of the ^{3}He atoms due to its own field.

The procedure to measure the Rb EPR shift is as follows. First, we look for the Rb resonance frequency using our EPR spectroscopy. Once the Rb resonance frequency is found, we frequency modulate the Rb rf frequency to get a dispersion signal from the probe beam. The dispersion signal is fed to a control circuit that locks to the zero crossing of the Rb resonance. The ^{3}He polarization is then flipped using AFP. The new Rb resonance frequency is then compared to the old one. The difference in the two is twice the total shift. The following subsections go into more detail.

5.11.2 Rb EPR Frequency Shift Polarimetry

Using the Breit-Rabi formula [Ramsey56] (equation 5.15), the transitional angular frequency between $(F, m \rightarrow F, m-1)$ states is

$$\omega_{F,m\rightarrow F,m-1} = g_I \mu_o B - \frac{\Delta E x}{\hbar(2I+1)} + \frac{\Delta E x^2}{\hbar(2I+1)^2} + \frac{\Delta E 2mx}{\hbar(2I+1)^2}. \tag{5.35}$$

What we are interested is in the change of electronic frequency of the alkali-atoms with respect to the change of the magnetic field due to the Fermi-contact interaction. Taking the derivative with respect to the magnetic field in the last equation we get

$$\delta\omega = \frac{g_I \mu_o \delta B}{\hbar} - \frac{(-g_J \mu_o + g_I \mu_o)}{\hbar(2I+1)}\delta B + \frac{(-g_J \mu_o + g_I \mu_o)}{\hbar(2I+1)^2} 2m\delta B + \frac{(-g_J \mu_o + g_I \mu_o)^2}{\Delta E \hbar(2I+1)^2} 2mB\delta B. \tag{5.36}$$

But $g_j \approx g_S \gg g_I$, thus for the $F = I + \frac{1}{2}$ hyperfine state

$$\delta\omega = \frac{g_S \mu_o}{\hbar(2I+1)}\delta B - \frac{g_S \mu_o}{\hbar(2I+1)^2} 2m\delta B - \frac{g_S \mu_o}{\Delta E \hbar(2I+1)^2} 2mB\delta B. \tag{5.37}$$

In our case we are working in a low magnetic field, thus the frequency shift is, ignoring everything except the first term,

$$\delta\omega = \frac{g_S \mu_o}{\hbar(2I+1)}\delta B. \tag{5.38}$$

The change in the magnetic field that is seen by the atoms is roughly a spherical volume that surrounds each atom or

$$\delta B = \frac{8\pi M}{3}, \tag{5.39}$$

where M is the magnetization due to the polarized ^{3}He. Substituting for M

$$\delta B = \frac{8}{3}\pi\mu_K[He]P_{He}, \tag{5.40}$$

where μ_K is the ^{3}He magnetic moment. Still this is not correct because a lot of times the Rb's electron has a enhanced probability of being at the nucleus of the ^{3}He atoms during binary collisions [Romalis98][Walker89]. Thus, the field that the electron feels enhances by a factor, κ_0. Taking this into account, the magnetic field seen by the Rb's electron due to the polarized ^{3}He is

$$\delta B = \frac{8}{3}\pi\kappa_0\mu_K[He]P_{He}. \tag{5.41}$$

Combining all the terms together we get

$$\Delta\nu = \frac{8}{3}\pi\frac{\mu_o g_S}{h(2I+1)}\kappa_o\mu_K[He]P_{He}. \tag{5.42}$$

$$= \left(1.13\ \frac{\text{KHz}}{\text{Amagat}}\right)\kappa_0[He]P_{He}, \tag{5.43}$$

for ^{85}Rb and where $[He]$ in the last equation is assumed to be in units of amagat. κ_0 has been measured very precisely [Romalis98] and is

$$\kappa_0 = 4.52 + 0.00934 \times T, \tag{5.44}$$

where T is the temperature of the cell and in units of Celsius.

The above value of κ_0 assumes that the cell is spherical. In our experiment, most of the cells are not spherical. We need to add the contribution to κ_0 due to the classical magnetic field that the Rb atoms feel due to the polarized Helium.

5.11.3 Geometric Correction of a Magnetized Cylinder

For a uniform magnetized cylinder, the magnetic scalar potential ϕ_M is [Jackson75]

$$\phi_M = \int d^2r' \frac{M.\hat{n}}{|\bar{r} - \bar{r}'|}, \tag{5.45}$$

where M is the magnetization due to the polarized Helium, and $\hat{n}$ is the unit vector. We can use the expansion in the cylindrical coordinate (ρ, ϕ, z) [Jackson75]

$$\frac{1}{|\bar{r} - \bar{r}'|} = \sum_m \int_0^\infty dk e^{im(\phi-\phi')} J_m(\kappa\rho) J_m(\kappa\rho') e^{-k(z_> - z_<)} \tag{5.46}$$

and cylindrical symmetry to obtain, for $-L/2 < z < L/2$

$$\phi_M(\bar{r}) = 4\pi M \int_0^a \rho' d\rho' \int dk J_0(\kappa\rho) J_0(\kappa\rho') e^{-\kappa L/2} \sinh \kappa z, \tag{5.47}$$

where L is the length of the cylinder with radius a. The magnetic field produced by the polarized ^{3}He nuclei is

$$\begin{aligned} B_{M_z}(\bar{r}) &= \frac{4\pi}{3} M + H_z \\ &= \frac{4\pi}{3} M - \delta_z \phi_M \\ &= \frac{4\pi}{3} M - 4\phi M \int \kappa d\kappa \cosh \kappa z J_0(\kappa\rho) e^{-\kappa L/2} \int_0^a \rho' d\rho' J_0(\kappa\rho') \\ &= \frac{4\pi}{3} M - 4\pi M a \int d\kappa \cosh \kappa z J_0(\kappa\rho) J_1(\kappa a) e^{-\kappa L/2} \end{aligned} \tag{5.48}$$

We are interested in the magnetic field at the cylindrical axis $\rho = 0$

$$B_{M_z}(0, \phi, z) = 4\pi M \left(\frac{-2}{3} + \frac{(L-2z)}{2\sqrt{4a^2 + (L-2z)^2}} + \frac{(L+2z)}{2\sqrt{4a^2 + (L+2z)^2}} \right). \tag{5.49}$$

This is the same axial magnetic field of a solenoid minus $8\pi M/3$, as expected. Since our probe samples the cell through the middle, to get the correction factor we need to average from $z = L/2$ to $z = -L/2$

$$\begin{aligned} \langle B_{M_z}(0,\phi)\rangle &= \int \frac{dz}{L} B_{M_z}(0,\phi,z) \\ &= \frac{8\pi M}{3}\left[-1 + \frac{3}{2L}\left(\sqrt{a^2+L^2} - a\right)\right] \end{aligned} \tag{5.50}$$

Thus, our $\delta\kappa_0$ is the term in the square bracket. This is the geometric correction term for a cylinder. The total enhancement factor κ taking into account the geometric correction of the cylinder becomes

$$\begin{aligned} \kappa &= \kappa_0 + \delta\kappa \\ &= 4.52 + 0.00934 \times T + \frac{1}{2} - \frac{3}{2}\left[1 + \frac{a}{L} - \sqrt{1+(a/L)^2}\right] \end{aligned} \tag{5.51}$$

5.11.4 Adiabatic Fast Passage

The effect of an alternating transverse magnetic field upon the nuclear spin of the Helium atoms is analyzed using classical physics [Slichter90]. Let the transverse magnetic field be

$$B_x = B_{xo}\cos\omega t. \tag{5.52}$$

This transverse magnetic field can be decomposed into two counter propagating components. One component rotating counterclockwise and one in the opposite direction. The two components can be written as

$$B_R = B_1(\mathbf{i}\cos\omega t + \mathbf{j}\sin\omega t) \tag{5.53}$$

$$B_L = B_1(\mathbf{i}\cos\omega t - \mathbf{j}\sin\omega t), \tag{5.54}$$

where $2B_1 = B_{xo}$. The subscripts R and L refer to left and right propagation or counterclockwise and clockwise, respectively. We may neglect one component of the

field since in the rotating frame, as will be shown, it rotates at twice the frequency and has no effect on the atoms. The equation of motion for the ^{3}He atoms due to the total field is

$$\frac{d\mu}{dt} = \mu \times \gamma\Big[B_o + B_R\Big], \tag{5.55}$$

where B_o is the static holding field along the z-direction. In a rotating frame with angular velocity ω, the equation of motion becomes [Slichter90]

$$\begin{aligned} \frac{\delta\mu}{\delta t} &= \mu \times \gamma\Big[\mathbf{k}(B_o - \frac{\omega}{\gamma}) + \mathbf{i}B_1\Big] \\ &= \mu + \gamma B_{eff}, \end{aligned} \tag{5.56}$$

where

$$B_{eff} = \mathbf{k}(B_o - \frac{\omega}{\gamma}) + \mathbf{i}B_1. \tag{5.57}$$

Thus, in the rotating frame the ^{3}He atoms see only this effective magnetic field. They precess in a fixed cone at an angular frequency of γB_{eff}.

This last equation is the basis of the two most popular ways of detecting ^{3}He atoms, namely free induction decay (FID) and adiabatic fast passage (AFP). For our frequency shift measurements, we rely on AFP. We use AFP not to detect the ^{3}He polarization but rather to flip the ^{3}He polarization. How it works can be seen easily from equation 5.57. If we were to start the rf frequency above resonance or

$$B_o \gg \frac{\omega}{\gamma}, \tag{5.58}$$

and assume that

$$B_o \gg B_1, \tag{5.59}$$

which is always the case experimentally, then the effective field seen by the ^{3}He atoms is roughly the static holding field. The Helium atoms will precess around this static field which points in the, say, positive z-direction. If we now sweep the transverse field

frequency closer to resonance, the effective field will lie somewhere between the static field and the transverse field. At resonance, the effective field will be just $B_1\mathbf{i}$. So the ^{3}He atoms will precess at this new effective field, which is perpendicular to the static holding field. If we continue sweeping the transverse field, the ^{3}He atoms will end up in the negative z-direction. Thus, the ^{3}He polarization has been flipped.

The magnitude of the rf field and the sweep rate must satisfy the AFP conditions [Slichter90]

$$\gamma B_1 \gg \frac{\dot{\omega}}{\gamma B_1} \gg D\frac{|\Delta B_z|^2}{B_1^2}, \tag{5.60}$$

where D is the diffusion coefficient of the ^{3}He atoms and ΔB_z is the field gradient of the static applied magnetic field. In our experiment, the Rb resonance frequency is 24.54 Hz. We sweep the rf frequency from 11950 Hz to 26050Hz at a rate of 0.170Hz. The loss per AFP flip is about 0.5%.

5.11.5 Rb EPR Frequency Shift Measurement

To lock the RF to the Rb Rf resonance, and then measure the frequency shift, we need a dispersion shaped signal. To do this we rely on the standard practice that is used in locking the diode laser. Assume that the resonance lineshape $T(\nu)$ is a Lorentzian. If the signal is modulated with an amplitude A, and frequency ν_m, then the transmitted signal will be

$$I_T(\nu) = I_T(\nu + A\sin\nu_m t) \tag{5.61}$$

We expand this using Taylor series

$$\begin{aligned} I_T(\nu) &= \sin\nu_m t(AdI_T/d\nu + ...) \\ &+ \cos 2\nu_m t(-A^2d^2I_T/4d\nu^2 + ...) + ... \end{aligned} \tag{5.62}$$

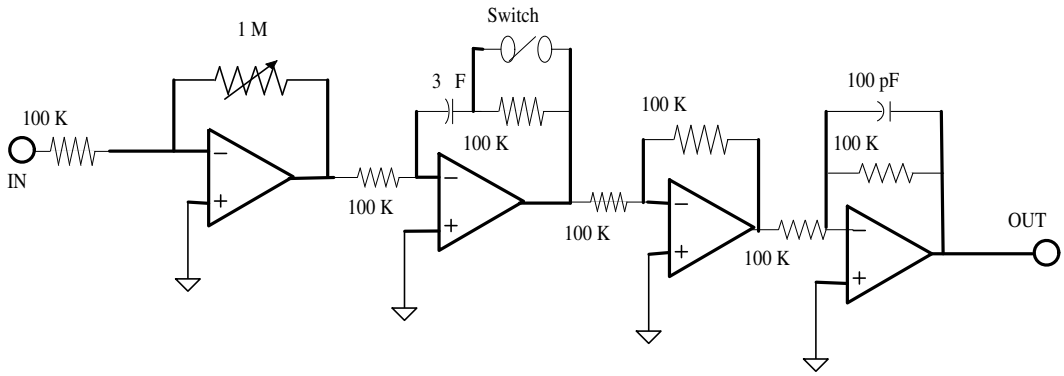

Figure 5.18: Locking circuit for EPR frequency shift measurement and magnetic field stabilization using the magnetometer.

When this signal is put into a lock-in amplifier and detected at the fundamental frequency, the signal is proportional to the derivative of the Lorentzian and therefore has the needed dispersion-like shape. Once the dispersion signal of the Rb atoms is obtained, we feed the signal to the locking circuit shown in figure 5.18. The locking circuit locks to the zero crossing signal of the Rb resonance frequency.

To get the Rb dispersion signal we send a modulation source signal to a voltage-controlled-oscillator (VCO) analog input of an rf generator (Tektronic CFG253). We use a function generator (SRS DS345) as our modulator. Typically we modulate the RF at 500Hz to 5000Hz, depending on the experimental conditions. Also, coupled with the modulation source is the output from the lock-box. The frequency of the rf generator is measured using a digital frequency counter (HP53131A). The output of the counter is sent to a computer where it is recorded. The computer reads the frequency at a one-second interval. The basic diagram is shown in figure 5.19. The ^{3}He polarization is then flipped and the frequency remeasured. The frequency shift of the Rb resonance as explain in section 5.10.2 is then just half this shift. A sample of a typical frequency shift is shown in figure 5.20.

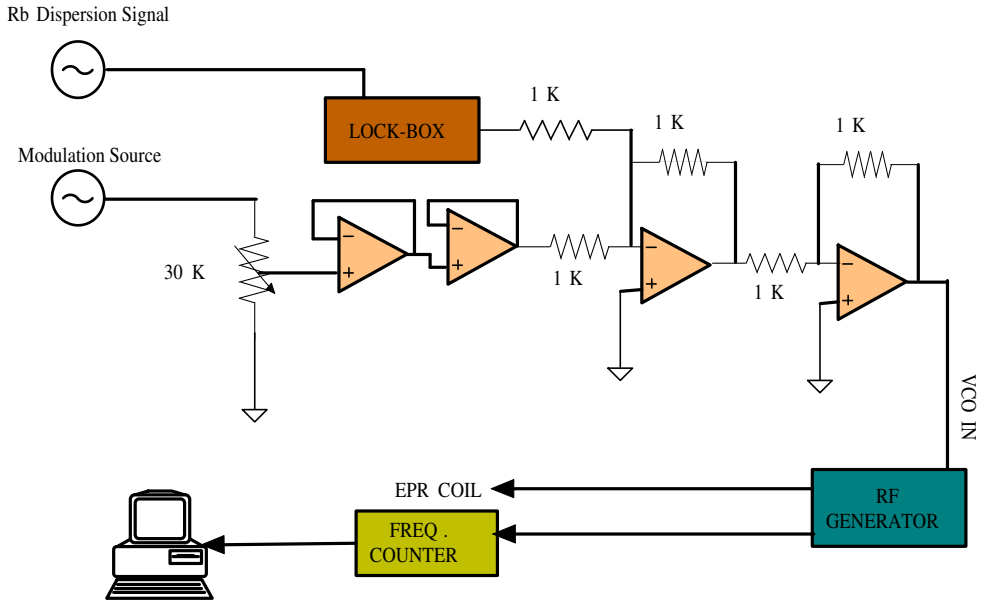

Figure 5.19: Set up for EPR frequency shift.

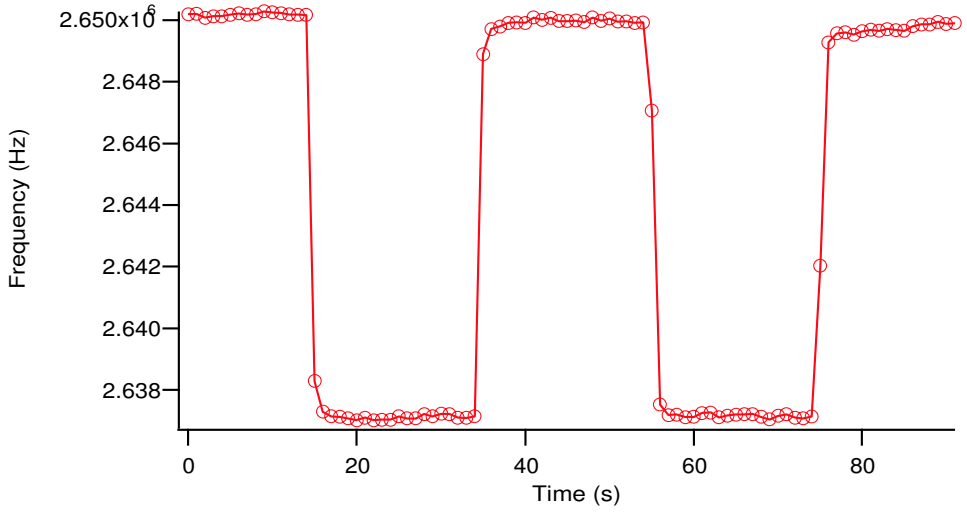

Figure 5.20: Typical Frequency shift of the Rb atoms. Here we flipped the ^{3}He atoms four times. The quality of the signal is limited by the stability of the magnetic field.

5.11.6 NMR frequency shift

Theory

We also introduce another method of measuring the ^{3}He polarization. It is based on the NMR frequency shift of the polarized ^{3}He due to its own field. This is non-zero for a non-spherical cell.

The magnetic field produced by the polarized ^{3}He nuclei in a cylindrical cell is, as shown in equation 5.48,

$$B_{M_z}(r) = \frac{4\pi}{3}M - 4\pi M a \int d\kappa \cosh \kappa z J_0(\kappa\rho) J_1(\kappa a) e^{-\kappa L/2}. \tag{5.63}$$

We are interested in the magnetic field at the surface of the cell or $\rho = a$

$$B_{M_z}(a,\phi,z) = M\left(\frac{-2\pi}{3} + 2K\left[\frac{-16a^2}{(L-2z)^2}\right] + 2K\left[\frac{-16a^2}{(L+2z)^2}\right]\right), \tag{5.64}$$

where $K(m)$ is the complete elliptic integral of the first kind [Abramowitz72]. At $z = 0$ and $\rho = a$ the equation simplifies to

$$B_{M_z}(a,\phi,0) = M\left(\frac{-2\pi}{3} + 4K\left[\frac{-16a^2}{L^2}\right]\right). \tag{5.65}$$

Figure 5.22 plots the field as a function of the aspect ratio of the cell. For our cell "Betty" with $L = 4.9$ cm and $a = 2.25$ cm and density $[He] = 2.067 \times 10^{19}$ cm^{-3}, the magnetic field is

$$B_{M_z}(a,\phi,0) = 4.6773 \times 10^{-4} \text{ Gauss} \tag{5.66}$$

assuming 100% polarization. The total (two times) NMR frequency shift is then

$$\begin{aligned} \delta\nu &= \nu_1 - \nu_2 \\ &= 2 \times 4.6773 \times 10^{-4} \times 3.243 \times 10^3 \text{ Hz} \\ &= 3.034 \text{ Hz}. \end{aligned} \tag{5.67}$$

This shift is large enough that, with care, it can be detected even at this low ^{3}He density.

Experiment

The experimental setup is shown in figure 5.1. A small surface coil (1.2 cm diameter, 0.6 cm long with 320 turns) is mounted on the side of the cylindrical cell. It is used both as a sending and pick-up coil. We actively stabilize the applied static magnetic field using a 2-gauss fluxgate magnetometer (Bartington single-axis fluxgate magnetometer MAG-01) placed about 20 cm from the cell. The magnetic field is stabilized to about 100 μG, which is close to the resolution of the magnetometer.

The experimental procedures is as follows. A pulse is sent to tip the ^{3}He atoms by a small angle and the free-induction decay (FID) signal is detected and mixed down to about 100 Hz with a lock-in amplifier. The resulting signal is fitted to the function

$$\sin(2\pi\nu_1 t + \phi)e^{-t/\tau} \tag{5.68}$$

to determine the center frequency ν_1. The ^{3}He atoms are then flipped using adiabatic fast passage (AFP). A second FID is then detected and analyzed using the same fit function to get the new center frequency ν_2. The two frequencies are than subtracted out to get the NMR frequency shift.

The primary source of error in this experiment is the applied static magnetic field drift which is not completely eliminated by the fluxgate field stabilization. In order to further reduce the magnetic field drift, we increase the sweep speed of the AFP. This increases the loss of the AFP to about 3% per pulse. Figure 5.23 shows the experimental result for our cell "Betty". Plotted in the figure are the NMR frequency shifts, NMR amplitudes and EPR frequency shifts. Notice the correlation amongst the three signals, as expected. The ^{3}He polarization using EPR frequency shift and NMR frequency shift differs by a few percent.

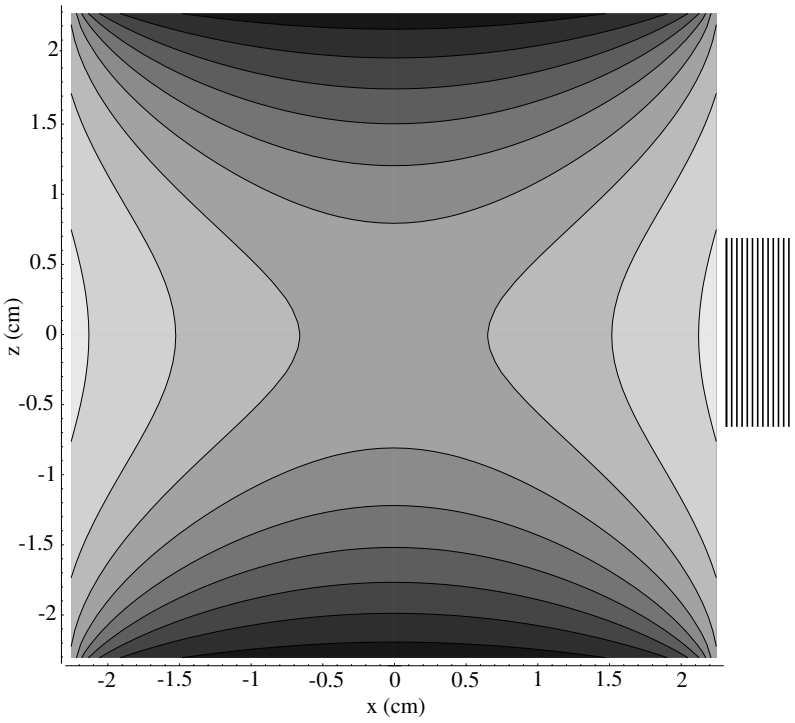

Figure 5.21: Magnetic field contours for the cell "Betty" used in this experiment. Also shown is the NMR pickup coil.

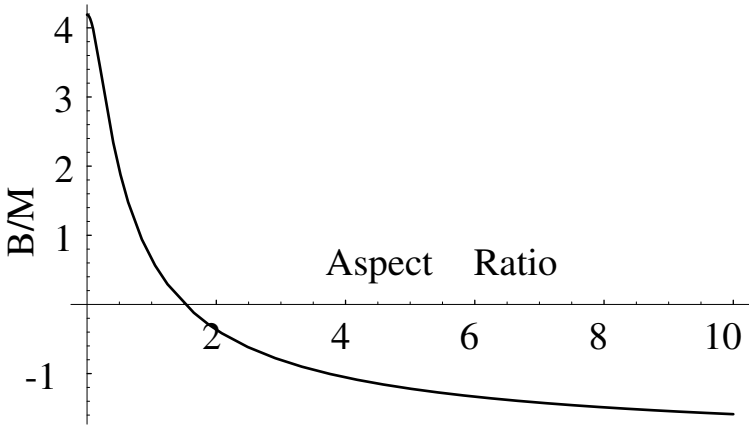

Figure 5.22: Classical magnetic field experienced by a noble gas nucleus due to the other nuclei. The field goes to zero for aspect ratio $a/L = 1.515$.

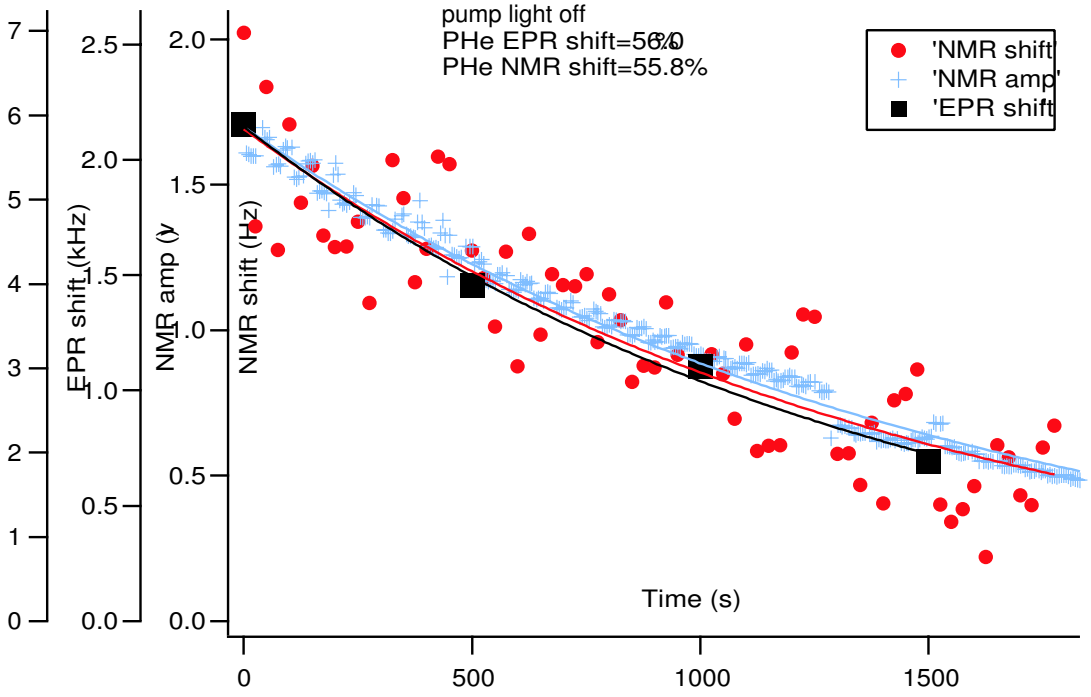

Figure 5.23: NMR frequencies, amplitudes, and EPR frequency shifts plotted as a function time. The noise is dominated by the static applied magnetic field drift. Note the correlation between all three parameters.

Chapter 6

Measurements of Rb-^{3}He Spin-Exchange Rates

6.1 Introduction

One of the very perplexing problems in Rb-^{3}He spin-exchange optical pumping is the low measured ^{3}He polarization compared to theory. With the current laser technology [Chann00], good lifetime spin-exchange cells [Hsu00][Rich02], and with current understanding of Rb-^{3}He spin-exchange, there should be no barrier to producing ^{3}He polarizations close to 100%. With very few exceptions [Coulter90][Larson91], the highest polarization that has been measured is about 55 %. Of the two noble gases, ^{3}He and ^{129}Xe, currently used in spin-exchange optical pumping, the fundamental physics behind Rb-^{3}He spin-exchange optical pumping is thought to be fully understood. Unlike ^{129}Xe, the basic spin-exchange mechanism in Rb-^{3}He occurs primarily due to binary collisions [Walker89] [Walker97] [Appelt98].

Until the work of Baranga *et al.* [Baranga98], only two measurements of the most fundamental parameter of the Rb-^{3}He spin-exchange, the spin-exchange rate coeffi-

cient, had been reported. Coulter *et al.* [Coulter90] measured the spin-exchange rate coefficient to be $12 \pm 2 \times 10^{-20}$ cm^3/s. Larson *et al.* [Larson91] using the same method measured the spin-exchange rate coefficient to be $6.2 \pm 0.2 \times 10^{-20}$ cm^3/s. In both of these measurements, the spin-exchange rate coefficient was deduced from the relaxation rate of ^{3}He as a function of temperature. In both cases the wall relaxation is assumed to be temperature-independent. Also, both experiments deduced the Rb vapor pressure using published saturated vapor curves [Killian26][Smithells65], a procedure that can be in error by a factor of 2 or more [Jau02] [Borel02].

Recently, Baranga *et al.* [Baranga98] remeasured the spin-exchange rate coefficient. They deduced the spin-exchange rate coefficient to be 6.7×10^{-20} cm^3/s. Baranga used a different method. The method did not rely on Rb density measurement. Furthermore, the method makes no assumption about the wall-relaxation of the cell. Therefore, it should be quite reliable.

To better understand the discrepancies between these three measurements, we re-measured the Rb-^{3}He spin-exchange rate coefficients. We measured it three different ways [Chann02b]. The first method we use is the same one used by Coulter [Coulter90] and Larson [Larson91] , which we call the "relaxation method". The second method is the one used by Baranga [Baranga98], which we call the "repolarization method". The third method is a new "rate balance method" which is based on the equilibrium ^{3}He polarization attained in a cell of known Rb density and ^{3}He polarization. In all these spin-exchange rate coefficients, we make no assumption about the magnitude of the anisotropic spin-exchange rate as briefly described in the first chapter.

Section 6.2 describes the theory of spin-exchange optical pumping which includes the often neglected anisotropic spin-exchange. Section 6.3 describes the experimental procedures. Section 6.4 gives the result of the measurements of the spin-exchange rates and discussions.

6.2 Theory

Including the anisotropic spin-exchange rate, the fundamental rate-equation governing the build-up or decay of the ^{3}He polarization is [Walter98]

$$\frac{\mathrm{dP_{He}}}{\mathrm{dt}} = \kappa_a[Rb](\langle P_{Rb}\rangle - P_{He}) - \Gamma_w P_{He} + \kappa_b[Rb](-\langle P_{Rb}\rangle/2 - P_{He}), \tag{6.1}$$

where κ_a is the isotropic spin-exchange rate coefficient, κ_b is the anisotropic spin-exchange rate coefficient. [Rb] is the rubidium density, and Γ_w is the wall depolarization rate of the ^{3}He atoms. The first term is the well-known spin-exchange interaction between Rb and ^{3}He. The second term is the loss due to the wall. The last term is the spin transfer to the ^{3}He nucleus due to the anisotropic hyperfine interaction and is usually assumed to be small. Note that the anisotropic term polarizes the ^{3}He nuclei antiparallel to the Rb spin [Walter98]. Thus, a substantial value of κ_b is a potential explanation for the low observed ^{3}He polarization.

From equation 6.1, the steady state polarization, P_{He}, of the ^{3}He atom is

$$P_{He} = \frac{(\kappa_\mathrm{a} - \kappa_\mathrm{b}/2)[\mathrm{Rb}]\langle \mathrm{P_{Rb}}\rangle}{(\kappa_\mathrm{a} + \kappa_\mathrm{b})[\mathrm{Rb}] + \Gamma_\mathrm{w}}. \tag{6.2}$$

The time constant, Γ_{He}, for build-up or decay of ^{3}He polarization is

$$\Gamma_{He} = (\kappa_a + \kappa_b)[Rb] + \Gamma_w. \tag{6.3}$$

Writing the ^{3}He polarization in terms of Γ_{He} we get

$$P_{He} = \frac{(\kappa_a - \kappa_b/2)[Rb]}{\Gamma_{He}}\langle P_{Rb}\rangle. \tag{6.4}$$

The above two equations provide us with two ways to measure and isolate κ_a and κ_b, and can be written as

$$\kappa_a - \kappa_b/2 = \frac{P_{He}\Gamma_{He}}{\langle P_{RB}\rangle[Rb]} \tag{6.5}$$

$$\kappa_a + \kappa_b = \frac{\delta(\Gamma_{He})}{\delta([Rb])}, \tag{6.6}$$

where $\frac{\delta(\Gamma_{He})}{\delta([Rb])}$ is just the slope of the ^{3}He relaxation rate as a function of the Rb density. The spin-exchange rate coefficient's measurement based on equation 6.5 is called the "rate balance method". Note that the "rate balance method" makes no assumption about the wall-relaxation. The spin-exchange rate coefficient's measurement based on equation 6.6 is called the "relaxation method".

Another method of measuring the spin-exchange rate coefficient was introduced by Baranga and coworkers [Baranga98]. This is the "repolarization method". In the absence of optical pumping, the Rb total longitudinal spin $\langle F_z\rangle_0$ obeys

$$\frac{d\langle F_z\rangle_0}{dt} = D\Delta^2\langle F_z\rangle_0 - \Gamma_{Rb}\langle S_z\rangle_0 + \kappa_a[He](\langle K_z\rangle - \langle S_z\rangle_0) + \kappa_b[He](-\langle K_z\rangle/2 - \langle S_z\rangle_0). \quad (6.7)$$

Here $\langle F_z\rangle_0 = \langle I_z\rangle_0 + \langle S_z\rangle_0$, where I_z and S_z is the nuclei and electron projection, respectively. The first term in the equation represents the loss of the spin to diffusion, where D is the diffusion coefficient. The second term is the loss due to the randomization of the electron spin [Happer72]. The last two terms are the spin-transfer terms. Due to the small diffusion coefficient [Happer72][Appelt98], the first term can be neglected completely. Thus, for $\Gamma_{Rb} \gg (\kappa_a + \kappa_b)[He]$ we can write the spin-exchange rate coefficient as

$$\kappa_a - \kappa_b/2 = \frac{\Gamma_{Rb}P_{Rb0}}{P_{He0}[He]}, \quad (6.8)$$

where P_{Rb0} is the Rb repolarization due to the spin-exchange being between Rb and ^{3}He in the absence of optical pumping. Note that the equation does not contain Rb density and makes no assumption about the wall. This makes the "repolarization method" probably the most reliable of the three methods.

6.3 Experiment

The spin-exchange rate coefficient measurements require us to determine the absolute Rb density, polarization and spin-relaxation rate. Also, we need to measure the absolute ^{3}He polarization and density. The methods to do this are described in detail in the previous chapter. Here I will just briefly describe the procedures.

The procedures to measure Rb-^{3}He spin-exchange rates are as follows. First we set our oven to the desired temperature, usually between 140C and 200C. Using our external cavity diode array with about 14W of power and about 125 GHz linewidth at 795 nm, we polarize the ^{3}He nuclei through spin-exchange optical pumping with the Rb atoms. The spin-up data is recorded on a personal computer using a Labview program. The spin-up is taken at a 30-minute time interval. After about 3 time-constants, we stop the spin-up. The ^{3}He polarization is then measured using the Rb EPR frequency shift. Next, the Rb polarization is measured using EPR spectroscopy. We then turn on the optical chopper and measure the polarization-Faraday rotation angle. From the rotation angle and the Rb polarization, we can deduce the Rb density. We then measure the Rb spin-relaxation. We use the optical chopper to chop the pump beam on and off. The Rb spin-relaxation is obtained by fitting the exponential decay of the Rb polarization when the pump beam is blocked.

The Rb repolarization is measured by blocking the pump beam and using an rf chopper. The repolarization rotation is then calibrated to the rotation angle when the Rb is fully polarized. This gives us the absolute repolarization. Finally, while the pump is still blocked we measure Rb density using field-Faraday rotation.

From all these measured parameters we can deduce the "repolarization method" and "rate balance method" spin-exchange rate coefficients. We get the "relaxation method" spin-exchange rate coefficient by measuring the ^{3}He relaxation rate, Γ_{He}, as

a function of Rb density, [Rb].

6.4 Spin-Exchange Rates and Discussion

Primarily, we use two cells for our measurements of the three spin-exchange rate coefficients. Both of them are cylindrical cells with well-defined geometries. The first one is "Betty" from NIST. She has a lifetime of 240 hours with a diameter of 4.7 cm and a length of 4.9 cm. Our second cell is "MichCell" from Michigan which has a lifetime of 8.16 hours with a diameter of 4.8 cm and a length of 4.5 cm. We have several more cells, most with much longer lifetimes than "MichCell". However, due to the lack of nice geometries for optical pumping we only use them to measure the spin-exchange rate using the "relaxation method".

Figure 6.1 shows spin-exchange rate coefficients deduced using the "repolarization method" and the "rate balance method" in "Betty" and "MichCell". In all of these measurements, we assume that the spin-exchange rate coefficients have no temperature-dependence [Walter98]. With "Betty" the statistical averages of the "repolarization method" gives $6.83 \pm 0.18 \times 10^{-20}$ cm^3/s for the spin-exchange rate coefficient. The "rate-balance method" gives $6.61 \pm 0.15 \times 10^{-20}$ cm^3/s. In "MichCell", the "repolarization method" gives the spin-exchange rate of $6.62 \pm 0.15 \times 10^{-20}$ cm^3/s, and the "rate-balance method" gives $6.60 \pm 0.21 \times 10^{-20}$ cm^3/s. Combining these measurements of the two cells, the deduced spin-exchange rate coefficient for the "repolarization method" is $6.73 \pm 0.12 \times 10^{-20}$ cm^3/s. The combined deduced spin-exchange rate coefficient for the "rate-balance method" gives $6.61 \pm 0.12 \times 10^{-20}$ cm^3/s.

The close agreement between the "repolarization method" and the "rate-balance method" is strong evidence that the systematic errors in the experiment are well controlled. The only common quantity measured in the two methods is the absolute ^{3}He

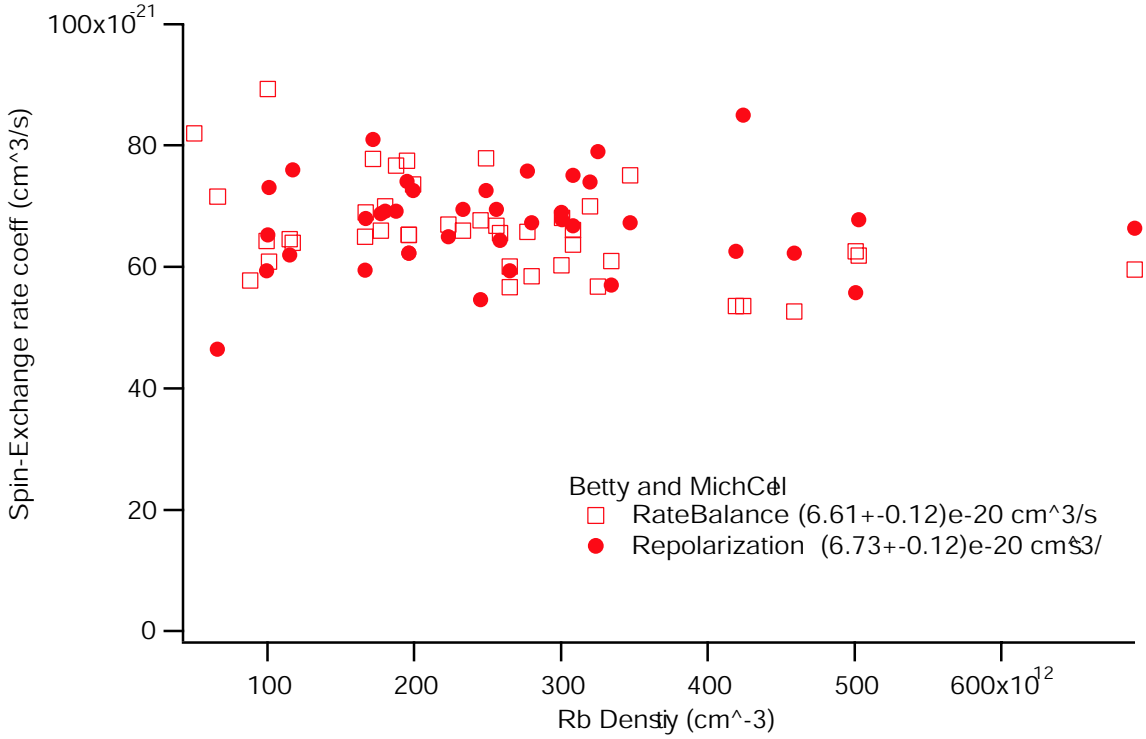

Figure 6.1: Spin-exchange rate coefficients deduced using the repolarization method and the rate balance method in "Betty" and "MichCell" with a lifetime of 240 and 8.16 hours, respectively.

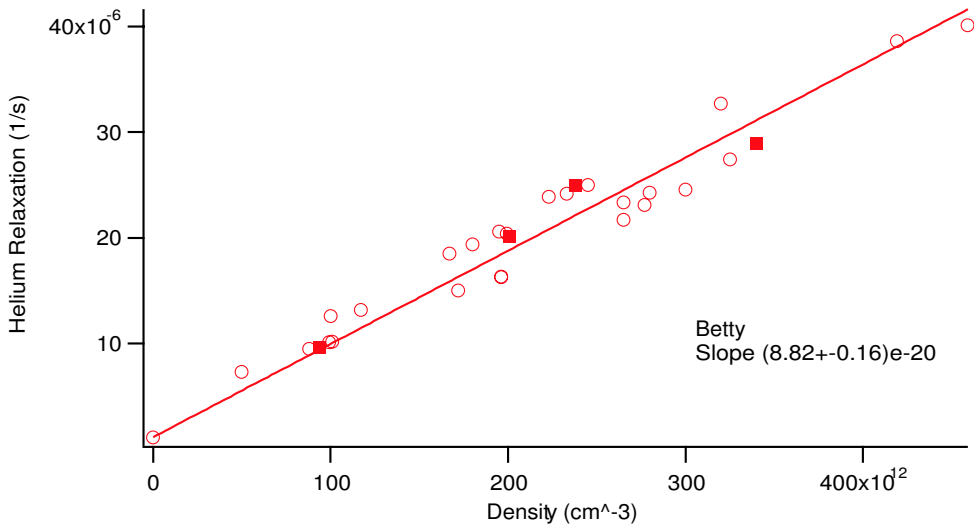

Figure 6.2: ^{3}He relaxation rate as a function of Rb density in "Betty". The circles are the points taken with the pumping laser on, the squares have the pumping laser off.

polarization. It occurs in the numerator for the rate balance method and the denominator for the repolarization method. Thus, the systematic errors in the two methods should be very different. Also it agrees very well with Baranga's deduced measurement of $6.7 \pm 0.6 \times 10^{-20}$ cm^3/s for the "repolarization method".

Figure 6.2 shows the ^{3}He relaxation rate as a function of Rb density for "Betty". This is the relaxation rate method. The slope of the data gives us the spin-exchange rate coefficient. The bulk of the data were taken with the light on, and few were taken with the light off. The slope of the data gives $\kappa_a + \kappa_b$ of $8.82 \pm 0.16 \times 10^{-20}$ cm^3/s. Compared to the two previous measurements using the same method [Coulter90][Larson91] our measurement lies almost exactly in the middle between the two.

The significantly larger value of the spin-exchange rate coefficient with the relaxation method indicates that there is an excess ^{3}He relaxation. This is most likely due to a temperature-dependent wall-relaxation and/or unexpectedly large anisotropic spin-exchange contributions. In order to explain the wall-dependent effect, the wall-

relaxation must produce a ^{3}He relaxation that is Rb-density dependent. If it is due to this, the mechanism responsible for it is entirely a mystery at this stage.

If it is due to the anisotropic optical pumping, the "measured" anisotropic spin-exchange rate coefficient is an order of magnitude larger than theoretical prediction. Assuming the anisotropic is present in all three methods, the deduced anisotropic spin-exchange rate would be about $1.4 \pm 0.34 \times 10^{-20}$ cm^3/s. The theoretical calculation predicted by Walter and coworkers [Walter98] is 0.17×10^{-20} cm^3/s, which is nearly an order of magnitude smaller. Using the same wave-functions, Walter and coworkers [Walter98] calculated the isotropic spin-exchange rate coefficient to be 5.6×10^{-20} cm^3/s, which is very close to the experimental value. Thus, at this stage, it is probably unlikely that the excess ^{3}He relaxation is due to the anisotropic optical pumping.

We also measure the spin-exchange rate coefficient using the relaxation rate method in 7 other cells. If the excess ^{3}He relaxation is due to the wall, then the spin-exchange rate coefficient due to the relaxation method should depend on the surface-to-volume ratio. We can parameterize the ^{3}He relaxation rate as

$$\Gamma_{He} = \eta S/V, \tag{6.9}$$

where S and V is the surface and volume of the cell, respectively. In the limit of surface-to-volume ratio equal zero, or no surface, the ^{3}He relaxation rate should go to 6.7×10^{-20} cm^3/s; since the ^{3}He relaxation only comes from the Rb-^{3}He spin-exchange. Figure 6.3 plots the relaxation rate of ^{3}He as a function of surface to volume ratio. Also shown is the line fit with 6.7×10^{-20} as the constraint to the intercept.

References	Method	Spin-Exchange Rate Coeff. (10^{-20} cm^3/s)
This work	Relaxation Method	8.82 ± 0.16
[Coulter90]	Relaxation Method	12± 2
[Larson91]	Relaxation Method	6.2 ±0.2
This work	Repolarization	6.73 ±0.12
[Baranga98]	Repolarization	6.7 ± 0.6
This work	Rate Balance	6.61 ± 0.12

Table 6.1: Rb-^{3}He spin-exchange rate coefficients using three different methods in this thesis and previously measured spin-exchange rates.

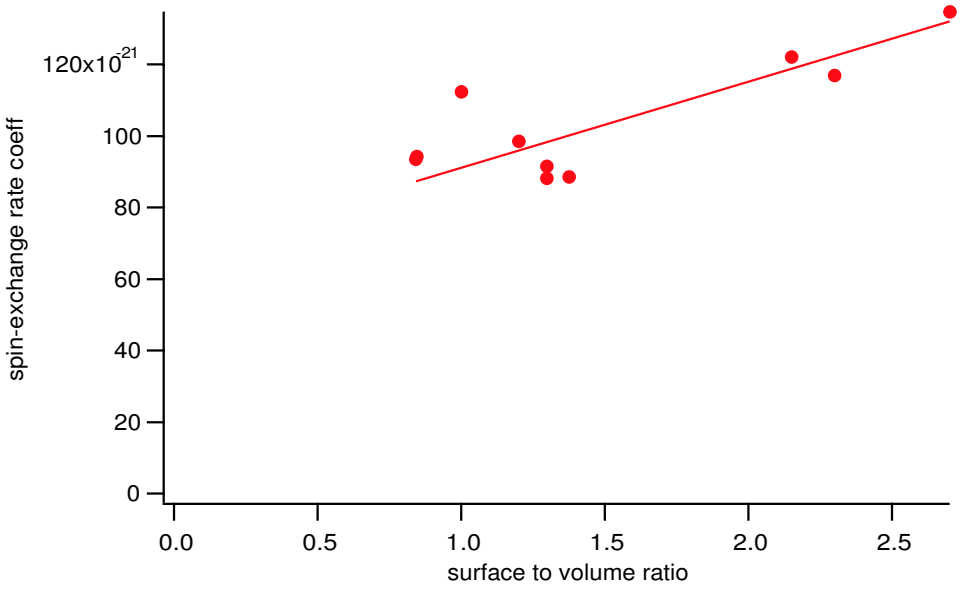

Figure 6.3: Spin-exchange rate coefficient using the relaxation rate method plotted as a function of surface-to-volume ratio for all the cells. Also shown is the line fit with 6.7×10^{-20} as the constraint to the intercept.

Chapter 7

Summary

In this thesis I have described a comprehensive study that was undertaken in the last four years in trying to understand the fundamental processes in spin-exchange optical pumping. One of the main underlying problems in spin-exchange optical pumping is the discrepancy between the measured noble gas polarization, ^{3}He and ^{129}Xe, and the theoretical prediction.

This thesis tries to answer that question in four parts. The first part deals with alkali-alkali relaxation, specifically with cesium-cesium relaxation. To achieve high noble gas polarization, the alkali-metal vapor must first be polarized. The limit of the alkali-metal vapor polarization is imposed by the alkali spin-relaxation. Most of this spin-relaxation comes from alkali-alkali collisions. Until recently, alkali-alkali relaxations were thought to arise from binary collisions where the correlation time is on the order of a few picoseconds. This, however, was proven to be incorrect by Kadlecek, Anderson, and Walker who showed that the relaxation can be reduced by a factor of two or more with a few thousand Gauss of external magnetic field. In this thesis we have shown that, although we still do not understand fully the relaxation at pressures of an atmosphere or more, an important part of the spin-relaxation comes from the classical

dipole-dipole anisotropic spin-axis interaction acting in triplet dimer molecules. The key observation is the existence of magnetic resonances in the magnetic decoupling curves which are predicted from the spin-axis interaction.

The second part of the thesis concerns ^{129}Xe-Xe van der Waals spin-relaxation. Here we identified a new gas-phase, room temperature spin relaxation that is due to the spin-rotation coupling in bound ^{129}Xe-Xe van der Waals molecules. In the practical condition of spin-exchange optical pumping, less than 10 amagats, this ^{129}Xe-Xe van der Waals relaxation is the primary relaxation. One of the reasons why this relaxation mechanism was not identified before is because for a fixed gas composition the relaxation is independent of the gas density, making it hard to separate this relaxation from the wall relaxation. By measuring the ^{129}Xe-Xe spin-relaxation as a function of gas composition we were able to isolate the ^{129}Xe-Xe relaxation from the wall relaxation. This ^{129}Xe-Xe spin-relaxation is more than an order of magnitude stronger than the well-known ^{129}Xe-Xe binary spin-relaxation.

The third part of the thesis deals with the pumping laser itself. The laser of choice used in spin-exchange optical pumping is the diode array bar (DAB) with power from 15 watts to hundreds of watts. However, the DAB's linewidth is typically about 1000GHz and much bigger than the absorption linewidth of the Rb atoms (20 GHz/bar) [Romalis97]. Conventionally, high ^{3}He or ^{4}He pressures (3 to 10 bar) are used to broaden the absorption linewidth, but such high pressures are not always desirable. Furthermore, most of the pump light is still wasted. With our external cavity diode array bar, we find, based on tests of several cells, that the power required to reach the same polarization is typically three times lower for the spectrally narrowed laser. This last result indicates that spectrally narrowed lasers are critical to obtaining the highest polarizations in large volume cells.

The fourth part of the thesis concerns Rb-^{3}He spin-exchange rates. Until the work of

Baranga et al. [Baranga98], only two measurements of the most fundamental parameter of the Rb-^{3}He spin-exchange, the spin-exchange rate coefficient, had been reported. Coulter et al. [Coulter90] measured the spin-exchange rate coefficient to be $12 \pm 2 \times 10^{-20}$ cm^3/s. Larson et al. [Larson91] measured and obtained the spin-exchange rate coefficient to be $6.2 \pm 0.2 \times 10^{-20}$ cm^3/s. Both of these measurements relied on the relaxation rate ("relaxation method") of ^{3}He as a function of temperature. In both cases the wall relaxation is assumed to be temperature-independent. Baranga and coworkers [Baranga98] remeasured the spin-exchange rate coefficient ("repolarization method"). They deduced the spin-exchange rate coefficient to be 6.7×10^{-20} cm^3/s. This method does not rely on Rb density and makes no assumption about the wall-relaxation.

In this thesis we measured the spin-exchange rate coefficients using three different methods. We obtained $6.73 \pm 0.12 \times 10^{-20}$ cm^3/s for the "repolarization method". Thus, it agrees very well with Baranga. We deduced the spin-exchange rate coefficient to be $6.61 \pm 0.12 \times 10^{-20}$ cm^3/s for the "rate balance method". Thus, these two methods agree very well with each other. For the "relaxation method" we deduced the value to be $8.85 \pm 0.32 \times 10^{-20}$ cm^3/s. This is about 30% higher than the other two methods. This implies a temperature-dependence wall-relaxation or a large value of anisotropic spin-exchange rate coefficient for Rb-^{3}He and would explain the shortfall ^{3}He measured polarization.

Appendix A

Fourier Grid Hamiltonian

The derivation of the Fourier Grid Hamiltonian to follow is taken from Marston and Balint-Kurti [Marston89] [Balint-Kurti92].

The basic idea behind Fourier Grid Hamiltonian method is the Fourier transforms between the coordinate and momentum space [Marston89] [Balint-Kurti92] [Borisov01]. The non-relativistic Hamiltonian, H, can be written as a sum of kinetic energy and potential energy operator

$$\begin{aligned} H &= \hat{T} + \hat{V}(x) \\ &= \frac{\hat{P}^2}{2m} + \hat{V}. \end{aligned} \tag{A.1}$$

The potential energy is diagonal in the coordinate representation.

$$\langle \acute{x}|\hat{V}(x)|x\rangle = V(x)\delta(\acute{x} - x) \tag{A.2}$$

The kinetic energy operator is orthogonal in the momentum representation.

$$\langle \acute{k}|\hat{T}|k\rangle = \frac{\hbar^2 k^2}{2m}\delta(\acute{k} - k) \tag{A.3}$$

where k is the wave-number. The transformation between the coordinate and momen-

tum representation is

$$\langle k|x\rangle = \frac{1}{(2\pi)^{1/2}} e^{-ikx}. \tag{A.4}$$

Thus if can write the Hamiltonian in one representation, we would be all set. It is easier to work in the spatial coordinate representation. We begin by taking the matrix element of the Hamiltonian in the coordinate representation

$$\begin{aligned} \langle x|\hat{H}|\acute{x}\rangle &= \langle x|\hat{T}|\acute{x}\rangle + V(x)\delta(x-\acute{x}), \\ &= \langle x| \int_{-\infty}^{\infty} \hat{T}|k\rangle\langle k|\acute{x}\rangle + V(x)\delta(x-\acute{x}), \\ &= \frac{1}{2\pi}\int_{-\infty}^{\infty} e^{ik(x-\acute{x})} T_k dk + V(x)\delta(x-\acute{x}). \end{aligned} \tag{A.5}$$

If we now discretize we obtain [Marston89] [Balint-Kurti92] [Borisov01]

$$\begin{aligned} H_{ij} &= \langle x|\hat{H}|\acute{x}\rangle = \frac{1}{2\pi}\sum_{l=-(n-1)}^{n} e^{il\Delta k(x_i - x_j)}\Big[\frac{\hbar^2}{2m}(l\Delta k)^2\Big]\Delta k + \frac{V(x_i)\delta_{ij}}{\Delta x}, \\ &= \frac{1}{\Delta x}\left[\sum_{l=-(n-1)}^{n} \frac{e^{il2\pi(i-j)/N}}{N}\Big[\frac{\hbar^2}{2m}(l\Delta k)^2\Big]\Delta k + V(x_i)\delta_{ij}\right], \end{aligned} \tag{A.6}$$

where the momentum spacing is $\Delta k = \frac{2\pi}{N\Delta x}$ and $\Delta x = L/N$ the grid spacing in the coordinate representation. L is the length of the grid, N (even) is the number of grid points and $n = N/2$. The above equation in the big bracket is just the normalized Hamiltonian

$$H^0_{ij} = \frac{1}{N}\left[\left[\sum_{l=1}^{n-1} 2T_l \cos\left(2l\pi(i-j)/N\right)\right] + (-1)^{(i-j)} T_{N/2}\right] + V(x_i)\delta_{ij}, \tag{A.7}$$

where

$$T_l = \frac{\hbar^2}{2m}(l\Delta k)^2 = \frac{1}{2m}(\frac{lh}{L})^2. \tag{A.8}$$

The summation can be shown to yield:

$$H^0_{ij} = \frac{h^2}{4mL^2}\left[\frac{(N-1)(N-2)}{6} + 1\right] + V(x_i)\delta_{ij}, \tag{A.9}$$

$$= \frac{(-1)^{(i-j)}}{m}\left[\frac{h}{2L\sin\left(\pi(i-j)/N\right)}\right]^2, \tag{A.10}$$

where the first equation is for $i = j$ and the second line is for $i \neq j$.

Thus, to calculate all the eigenvalues and eigenvectors, the matrix elements are calculated. The solutions of the matrix are all eigenvalues and eigenvectors, including all the continuum ones.

Appendix B

Alignment

B.1 Parts List:

Below are the parts and equipment that we used to build our external cavity diode array bar.

1. Low "smile" high power diode array bar with or without microlens (Coherent Inc. or CEO Inc. diode array bar)
2. Diode current driver (Newport 5045) [Newport]
3. Temperature controller (Melcor MTCA Series-120W) [Melcor]
4. Water-cooled high power diode laser mount (Newport-762 includes TEC for temperature control)
5. Cylindrical microlens (Doric lenses 1.500 mm diameter, 3.0 cm length, BBAR coated) [Doric]
6. 2× Newport GM-1R 3-axis waveplate/polarizer holder

7. 2× Newport RSA-1TI solid insert
8. 25.4 mm diameter, 50 mm focal length lens, BBAR coated (plano-convex singlet or achromat)
9. $\lambda/2$ plate in a rotating optics mount
10. 100 mm diameter, 250 mm focal length lens, BBAR coated (Melles Griot) [MellesGriot]
11. 50mm x 50mm 2400 lines/mm holographic diffraction grating (Edmund Industrial Optics K43-226) [Edmund]
12. Cylindrical lens, 75.6 mm focal length
13. 2-axis translator (New Focus EZ-track) [NewFocus]
14. assorted posts, bases, optical breadboard or table

B.2 Detailed Alignment Procedure

The alignment procedures for building the external cavity diode array bar are listed in detail in the following subsections. The first two subsections explain the alignment of the microlens to the array bar. We have found that the external cavity diode array bar works just as well if the diode array bar is already attached with a microlens by the manufacturers. Thus, the first two subsections can be skipped altogether.

B.2.1 Machining:

First we mill a 2cm diameter hole in one of the Newport RSA-1TI solid inserts. This solid insert will be used to mount the micro cylindrical lens. We then mill a 1.5mm

diameter hole, semicircular in cross section, across the insert. Using glue the micro cylindrical lens is then attached into the groove.

B.2.2 Align microlens

After the micro-lens is attached, we screw the machined cylindrical microlens holder RSA-1TI solid insert into one of the GM-1R holders. Place the GM-1R holder onto the 2-axis translational stage. Position the translational stage about 5 mm from the diode array bar. Make sure that the center of the microlens and the center of the diode array bar are at the same height. Also align the vertical axis of the diode array bar with the vertical axis of the microlens. We then position the 75.6 mm focal length cylindrical lens at z = 9 cm, and place a white screen at z = 58 cm. Turn the diode array bar on, running just above threshold. Using one of the knobs on the translational stage, we carefully translate the microlens in towards z = 0 while observing the image of the diode array at the screen (x,y,z=0 at the center of the diode array bar). As the microlens is moving closer to the diode array, make adjustments to the microlens to make sure that the vertical axis of the diode array is parallel to the axis of the microlens. As the microlens is getting closer to the diode array, at some point an image of some portion of the array should begin to come into focus on the white screen. Stop moving the microlens. If the image on the screen is not symmetric about the y-axis, adjust the rotation of the microlens with one of the knobs. Then, if only a portion of the diode array image is focused on the screen, it means that the vertical position, the y-axis, of the microlens is not yet parallel with the diode array. Keep in mind that the image is inverted. Thus, for example, if the vertical portion is imaged on the screen that means the bottom part of the microlens is closest to the diode array bar. Move the microlens away from the diode array bar and adjust the position of the microlens

using the vertical adjustment on the knob on the GM-1R holder. Move the microlens back to the original position. Now there should be more of the diode array imaged on the screen. Move the microlens out again and continue adjusting the vertical position of the microlens and move the microlens back until the whole diode array is imaged on the screen. Figure 4.1 shows the image of the diode array bar on the screen. Notice the curvatures of the diode array bars. After the diode array bar is properly imaged, remove the cylindrical lens and screen. Put the light beam of the diode array bar far(5m-10m) away and adjust the microlens until the beam is collimated. The beam size should be a few millimeters. Figure B.2 shows a picture of the diode array bar mounted on the diode mount and the microlens.

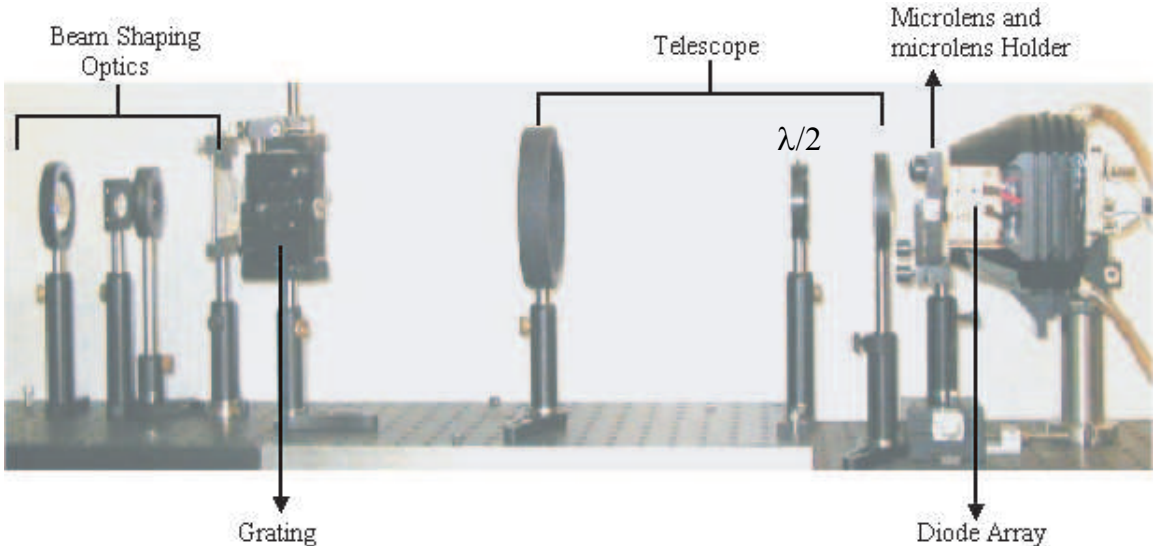

Figure B.1: External cavity diode array bar picture

B.2.3 Align telescope

Place the first telescope lens at z=50 mm. Project the beam onto the wall again. Make sure that the height of the center of the beam is at the same height as the diode array

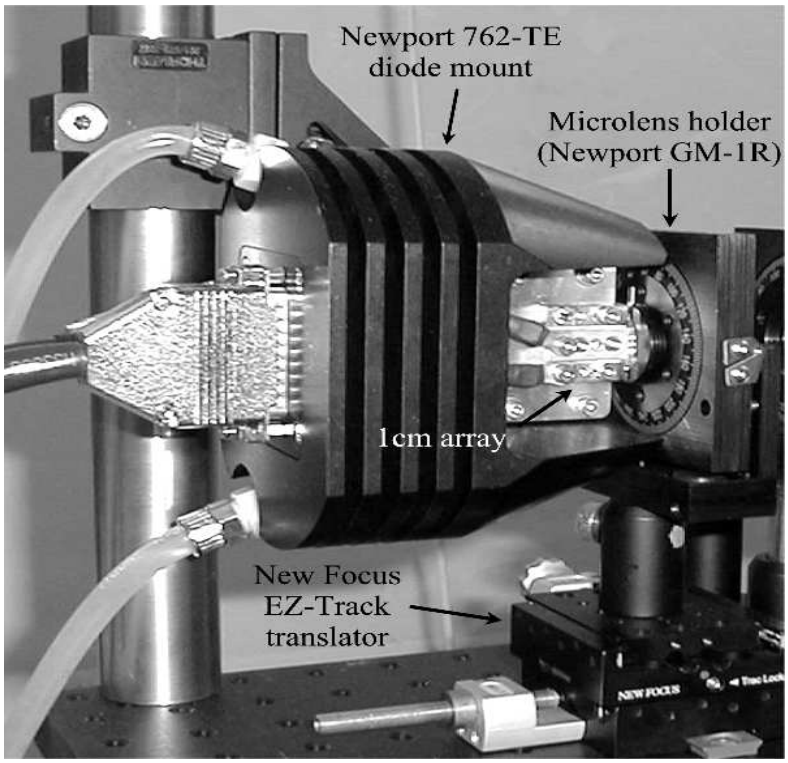

Figure B.2: Detailed picture of the diode array on the mount with the microlens attached

bar. Place the $\lambda/2$ plate a few cm from the first lens. Then place the second telescope lens at z=350mm. Again make sure the vertical and horizontal position of the beam is aligned with the diode array bar.

B.2.4 Position grating

Screw the second RSA-1TI insert into the GM-1R holder. Cement the holographic grating onto the RSA-1TI insert. Position the center of the grating at z=600 mm. An image of the diode array should be shown on the grating. Make sure that the groove of the grating is along the y-direction. Measure the power output and adjust the $\lambda/2$ plate for maximum power output.

B.2.5 Adjust feedback

Once all the lenses and grating are in place, use some appropriate spectrometer for observing the frequency of the array output in real time (e.g. Ocean Optics S2000 spectrometer). Adjust the position of the grating to allow for the first order diffraction light as the feedback back to the laser. A tuning peak with a broad background should show up in the spectrometer. Care must be taken to make sure that the spectrometer samples all of the diode bar elements equally. We found a good method is to focus the output beam onto a small spot on a holographic diffuser. The spectrometer is then placed behind the diffuser to sample the light.

Most likely the external cavity diode array is not working properly yet and needs further adjustments. The goal is to maximize the tuning peak. Make sure the groove of the grating is pointed along the y-direction; adjustment can be made with one of the knobs on the grating holder. Once that is maximized and if the diode array bar did not come with the microlens attached, further improvement can usually be made with the microlens by adjusting the horizontal position. Be extremely careful with this adjustment, since the microlens is very close to the diode array bar already. Once all these adjustments are maximized adjust the feedback using the $\lambda/2$ plate until the desired spectrum is obtained. Usually, the feedback required is about 20-30% of the free-running power output. Then turn the laser current to the desired power output. Figure B.1 shows the picture of the external cavity diode array bar.

B.2.6 Output Coupling

The high, spatially asymmetric output of the laser is efficiently coupled to the cell using the optical system set up as shown in figure C.2 (Appendix C). The choice of lenses depends on the distance and setup of the experiment. Shown in figure C.2 is a

set up for pumping one of our cylindrical cells with D=4.7 cm and L=4.9 cm. Here we use a 200-mm cylindrical lens to produce a symmetric, uniform beam on the $\lambda/4$ plate. A 62.7 mm spherical lens then images this plane onto the front face of the cell. Thus, depending on the experimental conditions a variation of this scheme can be implemented. Note that an additional lens is needed to fix skew light [Appendix C].

Appendix C

Skew Light Propagation in Optically Pumped Cell

For a neutral anisotropic vapor, Maxwell's equation can be written as

$$\nabla^2 \overrightarrow{E} - \nabla(\nabla \cdot \overrightarrow{E}) - \frac{1}{c^2}\frac{\partial^2 \overrightarrow{E}}{\partial t^2} = \frac{4\pi}{c^2}\frac{\partial^2 \mathbf{P}}{\partial t^2}, \tag{C.1}$$

where $\mathbf{P}$ is the induced polarization. If we assume we have a plane wave of the form

$$\overrightarrow{E} = \mathbf{E}e^{i(\mathbf{k}.\mathbf{r}-wt)} \tag{C.2}$$

with amplitude $\mathbf{E}$, frequency ω, and propagation wavenumber $k = \mathbf{k}/k$, the induced polarization $\mathbf{P}$ is defined as

$$\mathbf{P} = \chi \cdot \overrightarrow{E}, \tag{C.3}$$

where χ is the susceptibility tensor.

From equations C.1, C.2, C.3 the propagation of the light wave through an anisotropic vapor becomes

$$(k^2 - \mathbf{kk.})\mathbf{E} = k_0^2(1 + 4\pi\vec{\chi}\cdot)\mathbf{E}, \tag{C.4}$$

where $k_0 = \omega/c$. In our experiment we are interested in the effect of pump light propagating at an angle θ with respect to the quantization axis, z. First, we write the electric field amplitude as the superposition

$$\mathbf{E} = E_a\hat{a} + E_b\hat{b}, \tag{C.5}$$

where $\hat{a} = \hat{z}\times\hat{k}/\sin\theta$ and $\hat{b} = \hat{k}\times\hat{a}$ are the unit vectors and orthogonal to $\hat{k}$ and θ is the angle between the quantization z-axis and the propagation vector. The wavenumber k, amplitude E_a and E_b can be written as

$$k = (\sin\theta\cos\phi, \sin\theta\sin\phi, \cos\theta) \tag{C.6}$$

$$E_a = (\sin\phi, -\cos\phi, 0) \tag{C.7}$$

$$E_b = (\cos\theta\cos\phi, \cos\theta\sin\phi, -\sin\theta) \tag{C.8}$$

For an optically pumped vapor with B-field along the z-direction the alkali-metal susceptibility can be written in the simple form [Happer72][Appelt98]

$$\chi = \chi_0(1 - i\mathbf{P}\hat{z}\times). \tag{C.9}$$

Here χ plays the role of the Hamiltonian as in the Schrodinger equation. Taking the matrix elements

$$\hat{a}\cdot\chi\cdot\hat{a} = \hat{b}\cdot\chi\cdot\hat{b} = \chi_0, \tag{C.10}$$

$$\hat{b}\cdot\chi\cdot\hat{a} = -iP\chi_0\cos\theta = -\hat{a}.\cdot\chi\cdot\hat{b}. \tag{C.11}$$

Thus, the matrix of χ is just

$$\begin{pmatrix} \chi_0 & i\chi_0 P\cos\theta \\ -i\chi_0 P\cos\theta & \chi_0 \end{pmatrix}$$

The eigenvectors and eigenvalues of χ are

$$e_\pm = \frac{\hat{a} \pm i\hat{b}}{\sqrt{2}} \tag{C.12}$$

$$\chi_\pm = \chi_0(1 \mp P\cos\theta) \tag{C.13}$$

For a highly polarized vapor $P \approx 1$, the e_- mode is rapidly attenuated at the entrance to the vapor cell [Bhaskar80]. The interior of the cell the light is primarily in the e_+ mode. Note, however, that the transparency of this mode is not perfect even for $P = 1$ due to the $\cos\theta$ factor. To see this more clearly we find the wavenumber by substituting equation C.13 into equation C.4, assuming $k \cdot E = 0$,

$$k^2 = k_0^2 + 4\pi k_0^2 \chi_0 (1 - P\cos\theta). \tag{C.14}$$

$$k \approx k_0 (1 + 2\pi\chi_0 (1 - P\cos\theta)). \tag{C.15}$$

Hence, from this last equation, the attenuation of the light obeys

$$\frac{dI}{dr} = -n\sigma I(1 - P\cos\theta), \tag{C.16}$$

instead of $\frac{dI}{dr} = -n\sigma I$.

We now consider how the optical pumping is affected by the imperfect polarization of the light along the magnetic- field direction. Write out all the terms

$$e_+ = \frac{E_a + E_b}{\sqrt{2}} \tag{C.17}$$

$$= (\sin\phi + i\cos\theta\cos\phi, -\cos\phi + i\cos\theta\sin\phi, -\sin\theta)/\sqrt{2}. \tag{C.18}$$

It can then be resolved into σ^+, π, and σ^- polarization components. The fraction of light contains in each polarization is

$$f_+ = \cos^4(\theta/2) \tag{C.19}$$

$$f_\pi = 2\cos^2(\theta/2)\sin^2(\theta/2) \tag{C.20}$$

$$f_- = \sin^4(\theta/2) \tag{C.21}$$

In steady state, the rate at which angular momentum is added to the alkali-metal atoms by depopulation pumping from the $m_s = -1/2$ state must be balanced by the rate at

which angular momentum is removed by depopulation pumping from the $m_s = 1/2$ state and by spin relaxation

$$\frac{dt\langle F_z\rangle}{dt} = R\Big(\frac{f_\pi}{2} + f_+\Big)\Big(\frac{1}{2} - \frac{P}{2}\Big) - R\Big(\frac{f_\pi}{2} + f_-\Big)\Big(\frac{1}{2} + \frac{P}{2}\Big) - \frac{\Gamma P}{2} \tag{C.22}$$

At steady state the above equation reduces to

$$R\Big(\frac{f_\pi}{2} + f_+\Big)\Big(\frac{1}{2} - \frac{P}{2}\Big) = R\Big(\frac{f_\pi}{2} + f_-\Big)\Big(\frac{1}{2} + \frac{P}{2}\Big) + \frac{\Gamma P}{2} \tag{C.23}$$

solving for the polarization, P, gives

$$P = \frac{R(f_+ - f_-)}{R + \Gamma} = \frac{R\cos\theta}{R + \Gamma}. \tag{C.24}$$

Combining equation C.24 with equation C.16 gives

$$\frac{dI}{dr} = -n\sigma I\left(\frac{R\sin^2\theta + \Gamma}{R + \Gamma}\right) \tag{C.25}$$

Thus, the ratio of the differential equation with the pump beam propagating at an angle θ to when $\theta = 0$ is

$$\left.\frac{dI}{dr}\right|_\theta \Big/ \left.\frac{dI}{dr}\right|_{\theta=0} = \frac{R\sin^2\theta}{\Gamma} + 1. \tag{C.26}$$

The last equation tells us explicitly that when the pump beam makes an angle θ with the quantization axis, the absorption of the pump beam is greater by a factor

$$\frac{R\sin^2\theta}{\Gamma} + 1. \tag{C.27}$$

This can be quite severe in Rb-^{3}He optical pumping (worst in K-^{3}He), where R can be quite high and Γ is small. For a 50-W, 1-THz-broad 795-nm laser with a cell area of 40 cm^2, since the laser linewidth is much broader than the atomic linewidth, we estimate

$$R \approx \phi(\nu)\int d\nu\sigma(\nu) = \phi(\nu)\pi r_e f c = 4.4 \times 10^4\ s^{-1}. \tag{C.28}$$

A typical relaxation rate for Rb in Rb-^{3}He cell might be 500 s^{-1}, so that an $\theta = 0.11$ radian, the light absorption rate at the entrance to the cell is double.

Figure C.1 illustrates the effect [Chann02a]. We used a 15-W frequency narrowed diode laser sent along the axis of a 5-cm-long, 4.5-cm-diameter cylindrical Rb vapor cell contains 0.85 bar of ^{3}He and 65 torr of N_2. The temperature of the cell was 185C. The optical depth at this temperature is about 600. With only a skew angle of 3.1 degree (B_z= 8 gauss, and B_x=0.44 gauss), the transmission of the pump cut almost by half as compared to when the skew angle is a degree or less.

A second illustration of the effect is shown in figure C.3. The cell is heated to 200C where an optical depth of about 1000. Using about 17W of divergence narrowed light (overfilled), the Rb polarization measured is about 44%. We then collimate the pump light using a 400mm focal length (150mm diameter) as shown in diagram C.2. The Rb polarization increases to 81%.

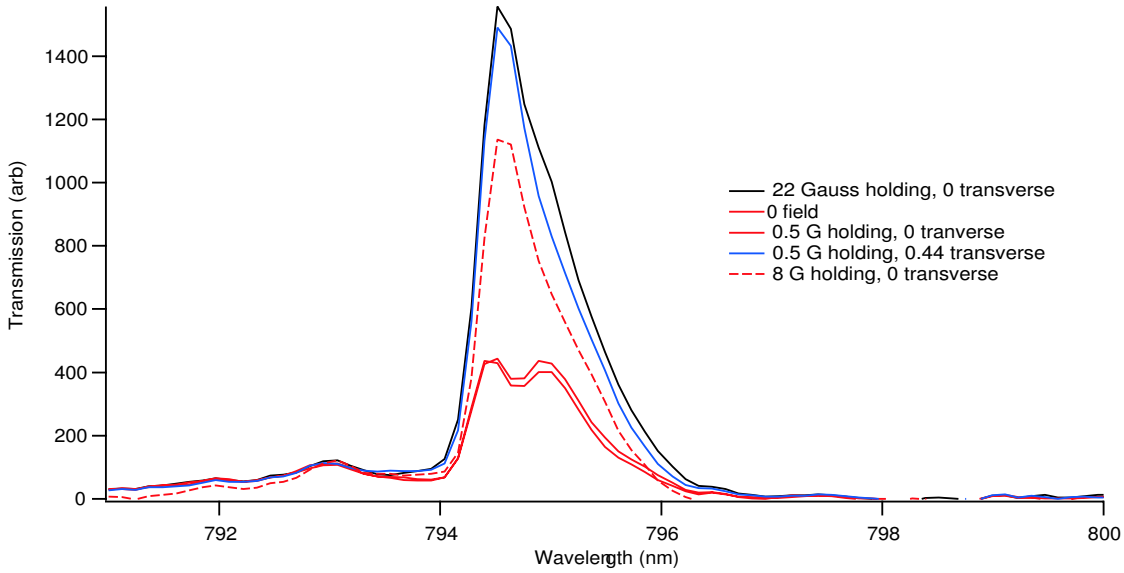

Figure C.1: Light transmission for various magnetic-field directions and magnitudes. The transverse field of 0.44 G is simply the Earths field that is cancelled for the 0.5-G data.

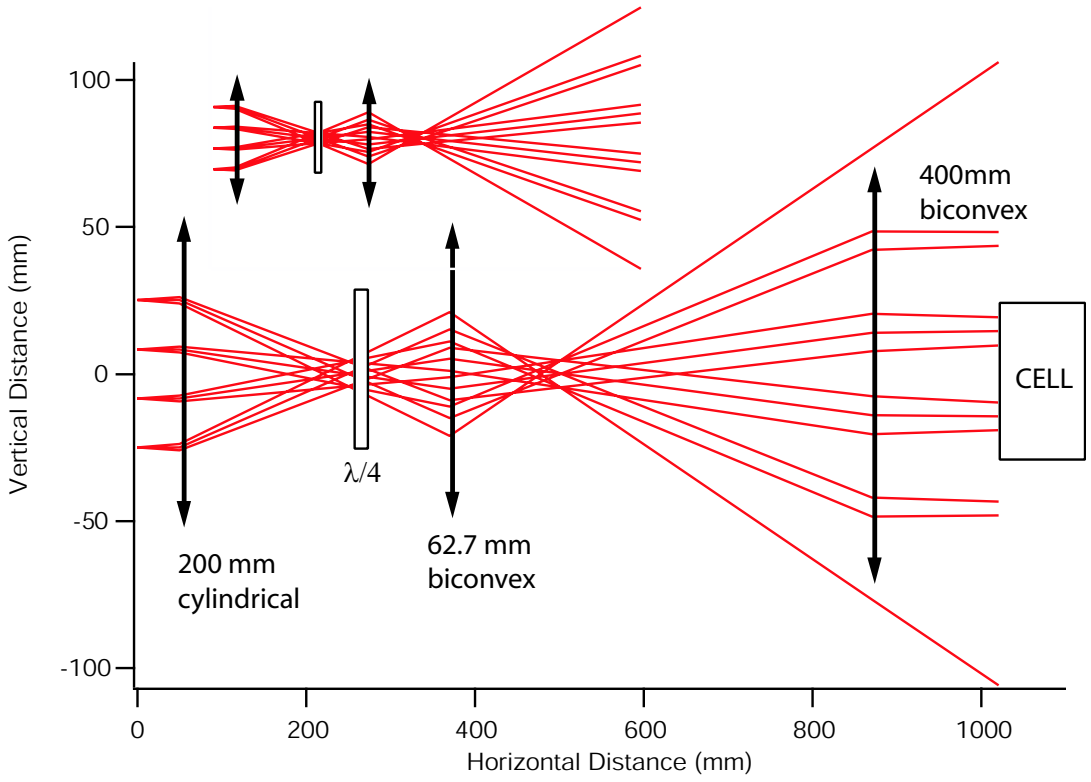

Figure C.2: Ray tracing optics (side view) used to correct for skew-light propagation. The grating, not shown, is at x=0. We used a 150mm diameter, 400 mm focal length biconvex lens to correct for the large divergence angle. The insert diagram is without the correction lens. The pump is overfilling the cell to insure uniform Rb polarization. Figure C.3 shows the results of the P_{Rb} with and without the correction optics.

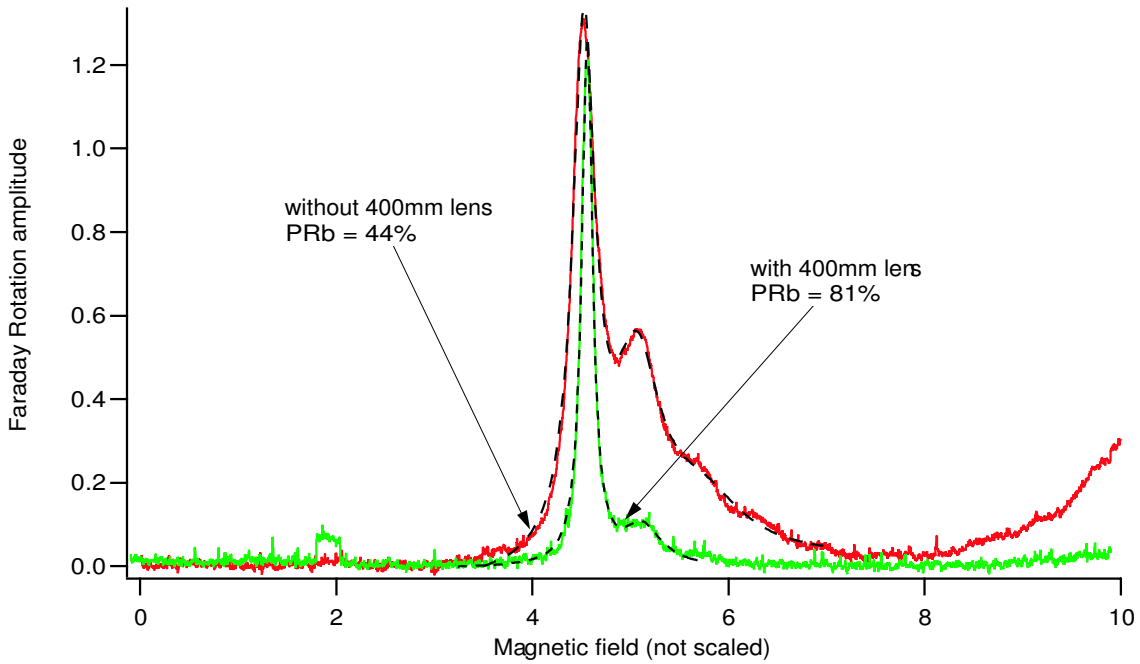

Figure C.3: EPR spectra taken with divergent and collimated light. Without collimation the $P_{Rb} = 44\%$, while collimated the $P_{Rb} = 81\%$. The main peak is the $F = 3, m = 3 \rightarrow F = 3, m = 2$ transition in ^{85}Rb, while the second peak is the unresolved $F = 3, m = 2 \rightarrow F = 3, m = 1$and $F = 2, m = 2 \rightarrow F = 2, m = 1$ pair. Notice the narrowing of the F=3, $m_F = 3 \rightarrow F = 3, m_F = 2$ peak as the polarization is getting higher [Appelt99]

Appendix D

Faraday Rotation

The following derivation of Faraday rotation is a generalization of Kadlecek's derivation [Kadlecek00] [Kadlecek01] [Vliegen01], where the fine structure mixing is taken into account due to the applied static magnetic field. This is especially important when the probe detuning is close to one of the resonances ($P_{1/2}$ and $P_{3/2}$) or the fine-structure splitting is small. We thank Prof. Nornval Fortson (University of Washington Physics department) for pointing out this effect.

For an alkali-metal atom in magnetic field B_z, the polarizability $\alpha_\pm$ can be written as

$$\alpha_\pm = \frac{e^2}{2\hbar} \sum_{Jm_J m_s} \frac{\{m_s|r_{\mp 1}|Jm_J\}\{Jm_J|r_{\pm 1}|m_s\}}{\omega - \omega_{Jm_J m_s} + i\gamma/2} P_{m_s}, \tag{D.1}$$

where the magnetic field B_z mixes states with the same m_J but different J. P_{m_s} is the probability to be in ground state $|m_s\rangle = \pm 1/2$. $r_\pm$ are the two components of the spherical basis. γ is the spontaneous decay rate from the state J. In our experiment, the probe is usually about 500-1000 GHz from resonance and, thus, we are only taking into account the fine-structure. A similar equation can be written when the hyperfine structure have to be taken into account. From first order perturbation theory, the

excited state $|Jm_J\}$ and ground state $|m_s\}$ can be written as

$$|Jm_J\} = |Jm_J\rangle - |J'm_J\rangle \frac{\langle J'm_J|H_\Omega|Jm_J\rangle}{E_{J'} - E_J} \tag{D.2}$$

$$|m_s\} = |m_s\rangle - |J'm_J\rangle \frac{\langle J'm_J|H_\Omega|m_s\rangle}{E_{J'} - E_{m_s}} = |m_s\rangle, \tag{D.3}$$

where $H_\Omega = g_J \mu_B J_z B$. The matrix element in equation D.3 is zero since the two wavefunctions have opposite parity and the operator is even parity. Substituting the last two equations into equation D.1, the resulting equation is

$$\begin{aligned} \alpha_\pm &= \frac{e^2}{2\hbar} \sum_{Jm_J m_s} \Bigg[\frac{\langle m_s|r_{\mp 1}|Jm_J\rangle\langle Jm_J|r_{\pm 1}|m_s\rangle}{\omega - \omega_{Jm_J m_s} + i\gamma/2} \\ &- C_{Jm_J} \frac{\langle m_s|r_{\mp 1}|J'm_J\rangle\langle Jm_J|r_{\pm 1}|m_s\rangle + \langle m_s|r_{\mp 1}|Jm_J\rangle\langle J'm_J|r_{\pm 1}|m_s\rangle}{\omega - \omega_{Jm_J m_s} + i\gamma/2} \Bigg], \end{aligned} \tag{D.4}$$

where $C_{Jm_J} = \frac{\langle J'm_J|H_\Omega|Jm_J\rangle}{E_{J'} - E_J}$ and the second order in C_{Jm_J} is neglected. It can be further simplified to

$$\begin{aligned} \alpha_\pm &\approx \frac{e^2}{2\hbar} \sum_{Jm_J} \frac{\langle m_s|r_{\mp 1}|Jm_J\rangle\langle Jm_J|r_{\pm 1}|m_s\rangle \Omega_{Jm_J M_s}}{\Delta_J^2} \\ &- \frac{e^2}{\hbar} \sum_{Jm_J m_s} \frac{\langle m_s|r_{\mp 1}|J'm_J\rangle\langle Jm_J|r_{\pm 1}|m_s\rangle}{\Delta_J}, \end{aligned} \tag{D.5}$$

where

$$\omega - \omega_{Jm_J m_s} = \Delta_J - \Omega_{Jm_J m_s} \tag{D.6}$$

and $\Omega = \mu_B B/\hbar$. Also γ has been neglected which is valid for large detuning from resonance. The difference between indices for the two circular polarizations is defined as

$$n_- - n_+ = \sqrt{1 + 4\pi N Re(\alpha_-)} - \sqrt{1 + 4\pi N Re(\alpha_+)} \approx 2\pi N(\alpha_- - \alpha_+), \tag{D.7}$$

where N is the alkali-metal vapor density.

The difference of α_+ and α_- for the magnetic field dependence gives

$$\alpha_+ - \alpha_- = \frac{-e^2\Omega}{2m\omega}\left[\frac{14}{9\Delta_{3/2}^2} - \frac{4}{9\Delta_{3/2}\Delta_{FS}} + \frac{8}{9\Delta_{1/2}^2} + \frac{4}{9\Delta_{1/2}\Delta_{FS}}\right], \tag{D.8}$$

where $-\Delta_{FS} = \Delta_{3/2} - \Delta_{1/2}$ is the fine-structure splitting. Hence, the Faraday rotation as a function of magnetic field gives

$$\begin{aligned}\Theta_B &= \frac{\pi N L \omega}{c}(\alpha_- - \alpha_+) \\ &= \frac{[N]Le^2\mu_B B}{18mhc}\left[\frac{7}{\Delta_{3/2}^2} + \frac{4}{\Delta_{1/2}^2} - \frac{2}{\Delta_{3/2}\Delta_{1/2}}\right],\end{aligned} \tag{D.9}$$

where the detuning are in units of Hertz.

The Faraday rotation as a function polarization P is less sensitive to the fine-structure mixing and is [Kadlecek00]

$$\Theta_P = \frac{[N]Le^2P}{6mc}\left[\frac{1}{\Delta_{3/2}} - \frac{1}{\Delta_{1/2}}\right], \tag{D.10}$$

where the detuning are in units of Hertz.

Bibliography

[Abragam61] A. Abragam, *Principles of Nuclear Magnetism*, Oxford University Press, New York, (1961).

[Abramowitz72] M. Abramowitz and I. A. Stegun (ed.), *Handbook of Mathematical Functions*, Dover Publications, Inc., New York (1972).

[Albert94] M. S. Albert, G. D. Cates, B. Driehuys, W. Happer, C. S. Springer, Jr., B. Saam, and A. Wishnia, Nature (London), Phys. Sci. **370**, 199 (1994).

[amg] 1 amagat is the density of atoms/molecules of 2.69×10^{19} cm^{-3} at STP.

[Anderson59] L. W. Anderson, F. M. Pipkin and J. C. Baird, Phys. Rev. **116**, 87 (1959).

[Appelt98] S. Appelt, A. Ben-Amar Baranga, C. J. Erickson, M. V. Romalis, A. R. Young, and W. Happer, Phys. Rev. A **58**, 1412 (1998).

[Appelt99] S. Appelt, A. Ben-Amar Baranga, A. R. Young, and W. Happer, Phys. Rev. A **59**, 2078 (1999).

[Aziz83] R. A. Aziz and A. van Dalen, J. Chem. Phys. **78**, 2402 (1983).

[Aziz89] R. A. Aziz, U. Buck, H. Jonsson, J. C. Ruiz-Suarez, B. Schmidt, G. Scoles, M. J. Slaman, and J. Xu, J. Chem. Phys. **91**, 6477 (1990).

[Aziz90] R. A. Aziz, U. Buck, H. Jonsson, J. C. Ruiz-Suarez, B. Schmidt, G. Scoles, M. J. Slaman, and J. Xu, J. Chem. Phys. **93**, 4492 (1990).

[Balint-Kurti92] G.G. Balint-Kurti, R.N. Dixon, and C.C. Marston. Internat. Rev. Phys. Chem., **11**, 317 (1992).

[Baranga98] A. Ben-Amar Baranga, S. Appelt, M. V. Romalis, C. J. Erickson, A. R. Young, G. D. Cates, and W. Happer, Phys. Rev. Lett. **80**, 2801 (1998).

[Barton94] A. S. Barton, N. R. Newbury, G. D. Cates, B. Driehuys, H. Middleton, and B. Saam, Phys. Rev. A **49**, 2766 (1994).

[Bhaskar80] N. D. Bhaskar, J. Pietras, J. Camparo, W. Happer, and J. Liran, Phys. Rev. Lett. **44**, 930 (1980).

[Bear00] D. Bear, R. E. Stoner, R. L.Walsworth, V. A. Kostelecky, and C. D. Lane, Phys. Rev. Lett. **85**, 5038 (2000).

[Borel02] P. I. Borel, C. J. Erickson, and D. K. Walter, Phys. Rev. A **66** 063410 (2002).

[Borisov01] A. G. Borisov, J. Chem. Phys. **114**, 7770 (2001).

[Bouchiat60] M.A. Bouchiat, T.R. Carver, and C.M. Varnum, Phys. Rev. Lett. **5** 373 (1960).

[Bouchiat69] C.C. Bouchiat, M.A. Bouchiat, and L. C. L. Pottier, Phys. Rev. **181** 144 (1969).

[Brinkmann62] D. Brinkmann, E. Brun, and H. H. Staub, Helv. Phys. Acta **35**, 431 (1962).

[CEO] Cutting Edge Electronics (imclaser.com), 20 Point West Boulevard, St. Charles, MO USA 63301 Model ARR26C020. Emitter size, 80 mm; 200-mm pitch.

[Chann00] B.Chann, I.Nelson, and T.G. Walker, Opt. Lett. **25**, 1352 (2000).

[Chann02a] B.Chann, E.Babcock, L.W.Anderson, and T.G.Walker, Phys. Rev. A **66**, 032703 (2002).

[Chann02b] B.Chann, E.Babcock, L.W. Anderson, and T.G. Walker, Phys. Rev. A **66**, 033406 (2002).

[Cohr] Coherent Inc, Santa Clara, CA 95054. Model B1-40C-19- 30-A.

[Coulter90] K. P. Coulter, T. E. Chupp, A. B. McDonald, C. D. Bowman, J. D. Bowman, J. J. Szymanski, V. Yuan, G. D. Cates, D. R. Benton, and E. D. Earle, Neutron polarization with a polarized 3He spin filter", Nucl. Instrum. & Methods A **288**, 463 (1990).

[Dham90] A. K. Dham, W. J. Meath, A. R. Allnatt, R. A. Aziz, and M. J. Slaman, Chem. Phys. **142**, 173 (1990).

[Dios97] A. de Dios and C. J. Jameson, J. Chem. Phys. **107**, 4253 (1997).

[Doric] Doric Lenses Inc. 1298 St-Paul Ancienne-Lorette Quebec G2E 1Z3 Canada Phone: (418) 877-5600.

[Driehuys96] B. Driehuys, G. D. Cates, E. Miron, K. Sauer, D. K. Walter, and W. Happer, Appl. Phys. Lett. 69, 1668 (1996).

[Edmund] Edmund Industrial Optics (edmundoptics.com) Sales Department W028 101 East Gloucester Pike Barrington, NJ 08007-1380

[Erickson00] C. J. Erickson, D. Levron, W. Happer, S. Kadlecek, B. Chann, L.W. Anderson, and T. G. Walker, Phys. Rev. Lett. **85** 4237 (2000).

[Fitzgerald99] R. J. Fitzgerald, M. Gatzke, David C. Fox, G. D. Cates, and W. Happer, Phys. Rev. B **59** 8795 (1999).

[Franzen59] W. Franzen, Phys. Rev. **115**, 850 (1959).

[Happer72] Happer, W., 1972, Rev. Mod. Phys. **44**, 169.

[Happer84] W. Happer, E. Miron, S. Schaefer, W. A. van Winjingaarden, and X. Zheng, Phys. Rev. A **29** 3092.

[Heil99] W. Heil, J. Dreyer, D. Hofmann, H. Humblot, E. Lelievre-Berna, and F. Tasset, Physica B **267-268**, 328 (1999).

[Hsu00] F. Hsu, G. D. Cates, I. Kominis, I. A. Aksay, and D. M. Dabbs, Appl. Phys. Lett. **77**, 2069 2000.

[Hunt63] E. R. Hunt and H.Y. Carr, Phys. Rev. **130**, 2302 (1963).

[Jackson75] J. D. Jackson, *Classical Electrodynamics*, New York: John Wiley and Sons, (1975).

[Jameson73] C. J. Jameson, A. K. Jameson, and S. M. Cohen, J. Chem. Phys. **59**, 4540 (1973).

[Jameson75] C. J. Jameson, A. K. Jameson, and S. M. Cohen, J. Chem. Phys. **62**, 4224 (1975).

[Jameson92] C. J. Jameson and A. C. de Dios, J. Chem. Phys. **97**, 417 (1992).

[Jau02] Y.-Y. Jau, N. N. Kuzma, and W. Happer, Phys. Rev. A **66**, 052710 (2002)

[Jones00] G. Jones, T. Gentile, A. Thompson, Z. Chowdhuri, M. Dewey, W. Snow, and F. Wietfeldt, Nucl. Instrum. & Methods A **440**, 772 (2000).

[Kadlecek98] S. Kadlecek, L. W. Anderson and T. G. Walker, Phys. Rev. Lett. **80**, 5512 (1998).

[Kadlecek00] S. Kadlecek, Ph.D. thesis, University of Wisconsin, Madison, (2000).

[Kadlecek01] S. Kadlecek, L.W. Anderson, C. J. Erickson, and T. G. Walker, Phys. Rev. A **64**, 052717 (2001).

[Killian26] T. Killian, Phys. Rev. **27**, 578 (1926).

[Krauss90] M. Krauss and W. J. Stevens, J. Chem. Phys. **93**, 4236 (1990).

[Larson91] B. Larson, O. Husser, P. P. J. Delheij, D. M. Whittal, and D. Thiessen, Phys. Rev. A **44**, 3108 (1991).

[Littman78] M. Littman and H. Metcalf, Appl. Opt. **17**, 2224 (1978).

[Marston89] C.C. Marston and G.G. Balint-Kurti, J. Chem. Phys., **91**, 3571 (1989).

[MacAdam92] K. MacAdam, A. Steinbach, and C. Wieman, Am. J. Phys. **60**, 1098 (1992).

[MacFall96] J. R. MacFall, Radiology **200**, 553 (1996).

[Migdalek98] J. Migdalek and Y.K. Kim. J. Phys. B: At. Mol. Opt. Phys. **31**, 1947 (1998).

[Melcor] Melcor Corp. (Melcor.com) 1040 Spruce Street Trenton, NJ 08648 Tel: 609-393-4178.

[MellesGriot] Melles Griot Corp. (Mellesgriot.com) 2051 Palomar Airport Road, 200 Carlsbad, California 92009.

[Middleton95] H. Middleton et al., Magn. Reson. Med. **33**, 271 (1995).

[Mies96] F. H. Mies, C. Williams, P. Julienne, and M. Krauss, J. Res. Natl. Inst. Stand. Technol. **101**, 521 (1996).

[Moudrakovski01] I. L. Moudrakovski, S. R. Breeze, B. Simard, C. I. Ratcliffe, J. A. Ripmeester, T. Seideman, J. S. Tse, and G. Santyr, J. Chem. Phys. **14**, 2173 (2001).

[Nagasaka01] B. Nagasaka, H. Omi, T. Eguchi, H. Nakayama, and N. Nakamura, Chem. Phys. Lett. **340**, 473 (2001).

[Nelson01] S. Kadlecek, Ph.D. thesis, University of Wisconsin, Madison, 2000.

[Newbury91] N. R. Newbury et al., Phys. Rev. Lett. 67, 3219 (1991).

[Newbury93] N.R. Newbury,A.S. Barton, G.D. Cates, W. Happer, and H. Middleton, Phys. Rev. A **48**, 4411 1993.

[NewFocus] New Focus Corp. (Newfocus.com) 2584 Junction Avenue San Jose, CA 95134 USA. (408) 919-1500

[Newport] Newport Corp. (Newport.com) 1791 Deere Avenue Irvine, CA 92606 In U.S. (800) 222-6440.

[Noble94] A. Noble and M. Kasevich, Rev. Sci. Instrum. **65**, 3042 (1994).

[Raftery91] D. Raftery, H. Long, T. Meersmann, P. J. Graninetti, L. Reven, and A. Pines, Phys. Rev. Lett. **66**, 584 (1991).

[Raftery92] D. Raftery, H. Long, L. Reven, P. Tang, and A. Pines, Chem. Phys. Lett. **191**, 385 (1992).

[Ramsey56] N. Ramsey, *Molecular Beams*, Clarendon Press (1956).

[Reif65] F. Reif, *Fundamentals of Statistical and Thermal Physics*. McGraw-Hill (1965).

[Rich02] D. R. Rich, T. R. Gentile, T. B. Smith, A. K. Thompson and G. L. Jones, Appl. Phys. Lett. **80**, 2210 (2002).

[Romalis97] M.V. Romalis,E. Miron, G.D. Cates, Physical Review A **56**, 4569 (1997).

[Romalis98] M. V. Romalis and G. D. Cates, Phys. Rev A **58** 3004 (1998).

[Romalis98b] M. V. Romalis, P. L. Bogorad, G. D. Cates, T. E. Chupp, K. P. Coulter, E. W. Hughes, J. R. Johnson, K. S. Kumar, T. B. Smith, A. K. Thompson, and R. Welsh, Nucl. Instrum. & Methods A **402**, 260 (1998).

[Romalis01] M. V. Romalis and M. P. Ledbetter, Phys. Rev. Lett. **87**, 067601 (2001).

[Schaefer89] S. R. Schaefer, G. D. Cates, T. R. Chien, D. Gonatas, W. Happer, and T. G. Walker, Phys. Rev. A **39**, 5613 (1989).

[Slichter90] C. P. Slichter, *Principles of Magnetic Resonance*, Springer-Verlag Berlin Heidelberg (1990).

[Smithells65] C. J. Smithells, *Metals Reference Book*, Butterworths, London, (1962), Vol. 2, p. 655.

[Torrey63] H. C. Torrey, Phys. Rev. **130**, 2306 (1963).

[Verhulst01] A. S. Verhulst, O. Liivak, M. H. Sherwood, H. M. Vieth, and I. L. Chuang, Appl. Phys. Lett. **79**, 2480 (2001).

[Vliegen01] E. Vliegen, S. Kadlecek, L. W. Anderson, and T. G. Walker, Nucl. Inst. Meth. Phys. Res. A, **460** 444 (2001).

[Walker89] T. G. Walker, Phys. Rev. A **40**, 4959 (1989).

[Walker97] T. G. Walker and W. Happer, Rev. Mod. Phys. **69**, 629 (1997).

[Walker02] Private communications.

[Walter98] D.K. Walter, W. Happer, and T.G. Walker, Phys. Rev. A **58** 3642 (1998).

[Walter01] D.K.Walter, W.M.Griffith, and W. Happer, Phys. Rev. Lett. **86**, 3264 (2001).

[Wieman91] C. E. Wieman and L. Hollberg, Rev. Sci. Instrum. **62**, 1 (1991).

[Wilms97] E. Wilms, M. Ebert, W. Heil, and R. Surkau, Nucl. Instrum. & Methods A 401, 491 (1997).

[Wu86] Z. Wu, M. Kitano, W. Happer, M. Hou, and J. Daniels, Applied Optics **25**, 4483 (1986).

[Wu90] Z. Wu, W. Happer, M. Kitano, and J. Daniels, Physical Review A **42**, 2774 (1990).

[Xu00] W. Xu et al., Phys. Rev. Lett. **85**, 2900 (2000).

[Young97] A. Young, S. Appelt, A. Ben-Amar-Baranga, C. Erickson, and W. Happer, Appl. Phys. Lett. **70** 3081 (1997).